UNIVERSITY OF CALIFORNIA SAN DIEGO

Excitons and Plasmons in Low-dimensional Systems

A dissertation submitted in partial satisfaction of the
requirements for the degree Doctor of Philosophy

in

Physics

by

Brian Sullivan Vermilyea

Committee in charge:

Professor Michael M. Fogler, Chair
Professor Leonid V. Butov
Professor Michael Galperin
Professor Tarun Grover
Professor Joel Yuen-Zhou

2024

The Dissertation of Brian Sullivan Vermilyea is approved, and it is acceptable in quality and form for publication on microfilm and electronically.

University of California San Diego

2024

DEDICATION

To my grandfather, David Vermilyea.

TABLE OF CONTENTS

LIST OF FIGURES

LIST OF TABLES

ACKNOWLEDGEMENTS

First and foremost, I would like to thank my PhD advisor, Prof. Michael Fogler. Misha is a great physicist and I have learned much working with him over the past few years. I always enjoy our physics discussions and appreciate his rigorous approach to research and sense of humor. I would also like to thank Prof. Congjun Wu. During my first year at UCSD, I was a member of Congjun's research group and took several courses with him. Although I did not continue working with Congjun, he was a great inspiration to me and his belief in my abilities helped motivate me through difficult times.

I would like to thank our experimental collaborators. I learned a lot working with Prof. Leonid Butov and the other members of his group, especially Erik Szwed, to help explain their experiments on excitons over the past couple years. Prof. Dmitri Basov hosted the weekly Columbia light-matter seminar where I learned more about experimental condensed matter physics. It was also great working with Prof. Mengkun Liu, Lukas Wehmeier, and Suheng Xu to understand their experiments on Landau-phonon polaritons.

Additionally, I would like to thank a number of other UCSD professors. I enjoyed taking graduate physics courses with Profs. John McGreevy, Daniel Arovas, and Tarun Grover, who clearly put a lot of effort into these courses. Prof. Yi-Zhuang You organized the CMT Journal Club where I learned more about current research in condensed matter theory. I was a teaching assistant for Prof. Ben Grinstein's graduate electromagnetism course for several years, and he gave me some good advice on teaching. Thanks also to the other members of my thesis committee, Profs. Michael Galperin and Joel Yuen-Zhou, for their time and comments on my work.

Thanks to my fellow group members, Andrey Rikhter, Shubham Parashar, and Yueqi Zhao for great company and many interesting discussions about physics and life in general. I wish them the best of success in their future careers. Finally, thanks to my parents, Mark and Kathleen, whose support and encouragement has been invaluable throughout my education, and to various other family members and friends who have

expressed their interest in and enthusiasm for my studies over the years.

Chapter 2, in full, is a reprint with permission of the material as it appears in 'B. Vermilyea and M. M. Fogler, Physical Review B **109**, 115401 (2024).' The dissertation author was the primary investigator and author of this paper.

Chapter 3, in part, is a reprint with permission of the material as it appears in 'L. Wehmeier, S. Xu, R. A. Mayer, B. Vermilyea, M. Tsuneto, M. Dapolito, R. Pu, Z. Du, X. Chen, W. Zheng, R. Jing, Z. Zhou, K. Watanabe, T. Taniguchi, A. Gozar, Q. Li, A. B. Kuzmenko, G. L. Carr, X. Du, M. M. Fogler, D. N. Basov, and M. Liu, Science Advances **10** (2024).'

Chapter 4, in part, is a reprint with permission of the material as it appears in 'E. A. Szwed, B. Vermilyea, D. J. Choksy, Z. Zhou, M. M. Fogler, L. V. Butov, D. K. Efimkin, K. W. Baldwin, and L. Pfeiffer, Nano Letters **24**, 13219 (2024).'

Chapter 5, in full, is currently being prepared for submission for publication of the material "Plasmon modes of topological-state networks in twisted bilayer graphene" by B. Vermilyea and M.M. Fogler. The dissertation author was the primary investigator and author of the material.

VITA

2018 B.S. in Physics, McGill University

2024 Ph.D. in Physics, University of California San Diego

PUBLICATIONS

B. Vermilyea and M. M. Fogler, "Feshbach resonance of heavy exciton-polaritons," Physical Review B **109**, 115401 (2024).

L. Wehmeier, S. Xu, R. A. Mayer, B. Vermilyea, M. Tsuneto, M. Dapolito, R. Pu, Z. Du, X. Chen, W. Zheng, R. Jing, Z. Zhou, K. Watanabe, T. Taniguchi, A. Gozar, Q. Li, A. B. Kuzmenko, G. L. Carr, X. Du, M. M. Fogler, D. N. Basov, and M. Liu, "Landau-phonon polaritons in Dirac heterostructures," Science Advances **10** (2024).

E. A. Szwed, B. Vermilyea, D. J. Choksy, Z. Zhou, M. M. Fogler, L. V. Butov, D. K. Efimkin, K. W. Baldwin, and L. Pfeiffer, "Excitonic Bose Polarons in Electro-Hole Bilayers," Nano Letters **24**, 13219 (2024).

ABSTRACT OF THE DISSERTATION

Excitons and Plasmons in Low-dimensional Systems

by

Brian Sullivan Vermilyea

Doctor of Philosophy in Physics

University of California San Diego, 2024

Professor Michael M. Fogler, Chair

In this dissertation, I study the many-body physics of two types of collective excitations, excitons and plasmons, in low-dimensional systems. In Chapter 1, I explain how low-dimensional systems are realized and discuss their importance in condensed matter physics. I subsequently introduce excitons and plasmons, as well as exciton-polaritons and exciton-polarons. Chapter 2 considers a novel type of polariton formed by hybridization of excitons in a two-dimensional semiconductor with surface optical phonons or plasmons. We show that these quasiparticles can bind into bipolaritons near a Feshbach-like scattering resonance and analyze the physics of a many-body condensate of polaritons and bipolaritons. In Chapter 3, we study another type of polariton that

results from the hybrdiization of magnetoexcitons in graphene with hyperbolic phonon modes in hexagonal boron nitride, and calculate the shift in the magnetoexciton energy due to many-body effects. We investigate excitonic Bose-polarons in Chapter 4, where we develop a many-body theory of these polarons formed by spatially direct excitons immersed in a degenerate Bose gas of spatially indirect excitons. In Chapter 5, we study surface plasmons in minimally-twisted gapped bilayer graphene that develops a triangular network of partial dislocations (or AB-BA domain walls) hosting one-dimensional electronic states, and formulate a theoretical model describing the plasmonic spectrum of the network in different regimes of temperature and electron-electron interaction strength. Conclusions are given in Chapter 6, where I also outline potential future research directions.

Chapter 1

Introduction

In condensed matter physics, low-dimensional systems are of great current interest due to their high degree of tunability and novel properties. Such systems arise when electrons are spatially confined in one or more dimensions and can be realized in several different ways: in nano-fabricated structures, such as semiconductor quantum wells [1]; in two-dimensional (2D) materials such as graphene or monolayer transition metal dichalcogenides [2], or one-dimensional (1D) materials such as carbon nanotubes [3]; or as topological states at the boundary between two higher-dimensional regions [4].

From an experimental perspective, low-dimensional systems often have the advantage that they can more easily be controlled and manipulated than their three-dimensional (3D) counterparts. For example, the electron density in graphene can be changed by applying an external gate voltage. Additionally, 2D materials can be stacked to form heterostructures and superlattices that exhibit unique phenomena, such as superconductivity and correlated insulating states observed in a twisted bilayer graphene superlattice [5, 6]. On the theoretical side, low-dimensional systems are intriguing because the physics of interacting particles strongly depends on dimensionality. With reduced dimensionality, electron-electron interactions have a more pronounced effect. In fact, electrons in one dimension form a Luttinger liquid where the low-energy excitations are entirely collective, rather than single-particle, in nature [7]. At the same time, quantum fluctuations become

stronger as the system's dimension decreases and limit its ability to form ordered states.

Collective excitations in low-dimensional systems are of interest for several reasons. First of all, they determine the optical properties and reveal information about the underlying electronic state of the system. Furthermore, they can serve as a tunable platform to explore many-body physics and create novel solid-state devices. Here we study two types of collective excitations: excitons, which are bound electron-hole pairs in semiconductors, and plasmons, which are longitudinal oscillations of electrons in conductors. In the following I provide a brief overview of excitons and plasmons before proceeding to the next chapter.

Excitons are created by absorption of a photon in a semiconductor, which excites an electron from the conduction to the valence band. Removing an electron from the valence band creates a positively-charged quasiparticle called a hole. Due to the attractive Coulomb interaction between them, the electron in the conduction band and hole in the valence band form a bound state known as an exciton. Another type of exciton — magnetoexcitons — appear in 2D conductors subject to a strong magnetic field (Chapter 3). They are bound states of electrons and holes residing in different Landau levels. In general, excitons are observed as peaks in the optical absorption spectrum of a material, and as composite bosons they can provide a solid-state realization of Bose-Einstein condensation and superfluidity [8, 9]. Furthermore, excitons can resonantly couple to photons to form hybrid light-matter states know as exciton-polaritons [10]. In Chapters 2 and 3, we consider a generalized notion of exciton-polaritons where the excitons are coupled to phonons or plasmons instead of photons. We also study exciton-polarons: excitons dressed by a surrounding Bose and Fermi gas to form a new quasiparticle (Chapter 4).

The physical origin of plasmons can be simply understood. If the electron density in a conductor is increased in one region, the electrons repel each other and try to return to their equilibrium position. However, they will overshoot the mark, setting up a longitudinal oscillation known as a plasmon. The plasmon dispersion at long-wavelength can be found

by solving hydrodynamic equations for the electron density and current and depends on the Drude weight, i.e., the weight of the zero-frequency peak in optical conductivity [11]. Alternatively, plasmons can be viewed as superpositions of electron-hole pair excitations where the hole refers to an empty state in the Fermi sea. In 3D, the plasmon is a gapped mode that has finite frequency even as its momentum q tends to zero, which is due to the long-range of the Coulomb interaction. In lower dimensions the plasmon dispersion is gapless: its frequency scales as $\sqrt{q}$ in 2D and linearly in q with logarithmic corrections in 1D. In Chapter 5, we study plasmon modes in a 2D network of 1D electronic states formed in twisted bilayer graphene.

Chapter 2

Feshbach resonance of heavy exciton-polaritons

2.1 Introduction

In this chapter, we consider heavy exciton-polaritons, a novel type of polariton formed by hybridization of excitons in a two-dimensional (2D) semiconductor with surface optical phonons or plasmons [12]. Exciton-polaritons, formed by coherent coupling of excitons with photons in semiconductor microcavities, have been a subject of active research [10, 13]. These hybrid light-matter quasiparticles are of interest due to their potential device applications [14] and solid-state realizations of condensation and superfluidity [15, 16]. Many phenomena unique to exciton-polaritons stem from strong interactions induced by their excitonic component. Recent pump-probe optical experiments revealed that exciton-polaritons can exhibit a Feshbach scattering resonance mediated by the biexciton state [17, 18, 19, 20, 21, 22], which in some sense allows one to control the strength and sign of polariton interactions, akin to the manipulation performed in experiments with atomic gases.

The origin of the exciton-polariton Feshbach resonance is associated with formation of bipolaritons, i.e., bound states of polaritons. One might expect that bipolaritons are realized when the Rabi splitting (Sec. 2.2.1) exceeds the biexciton binding energy. However, due to the strong dispersion of the photon, exciton-polaritons have a very

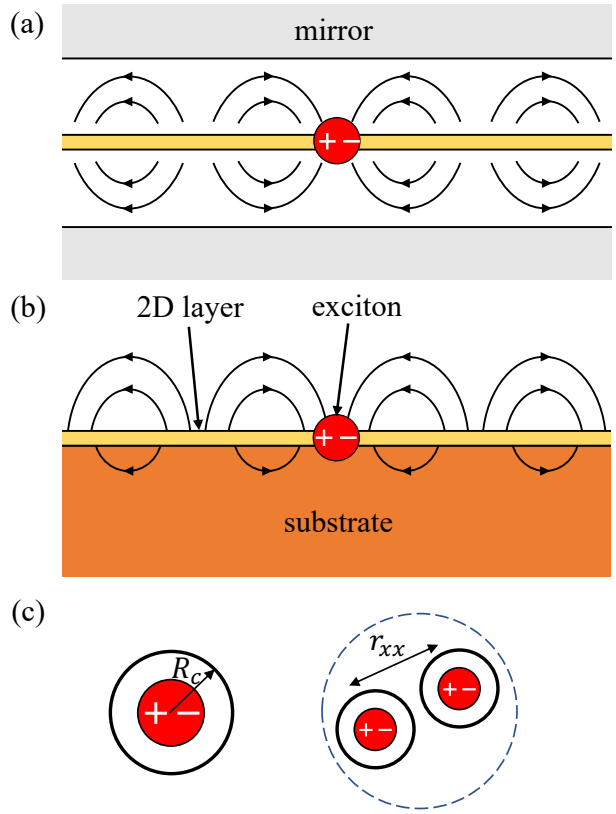

Figure 2.1. Schematic diagrams of (a) the photon cavity and (b) phonon/plasmon cavity. The lines indicate the electric field direction. (c) Schematic of the heavy-exciton polariton (left) and bipolariton (right) The ring surrounding the exciton indicates the characteristic polariton radius $R_c = (1/m_x\Omega)^{1/2}$, with m_x the exciton mass and Ω the polariton Rabi frequency. Bipolaritons are well defined when the biexciton binding energy E_{xx} is much smaller than Ω, or equivalently R_c is much smaller than the length scale $r_{xx} = (1/m_x E_{xx})^{1/2}$, which is of order the bipolariton radius.

small effective mass and the bipolariton binding energy is exponentially suppressed in 2D. Thus, bipolariton states are not observed [23], although radiative corrections can significantly modify the biexciton dispersion [24, 25, 26, 27]. Note that while such radiatively renormalized biexciton states are often called bipolaritons in the literature, in this chapter we use the term bipolariton to mean a true bound state of two polaritons with energy below the two-particle continuum.

Polaritons in 2D materials, such as phonon polaritons in hexagonal boron nitride and exciton-polaritons in tranitional metal dichalcogenide (TMD) monolayers, are a

growing research field which provides a controllable platform to study polaritons and their interactions [28, 29]. Motivated by this, we consider a novel type of exciton-polariton formed by strong coupling of excitons in a 2D semiconductor with surface optical phonons or surface plasmons, see Fig. 2.1(a),(b). In contrast to previous investigations of resonant exciton-phonon coupling [30, 31, 32], we consider the regime where the phonon frequency is resonant with transitions across the band gap, not between internal states of the exciton. This is similar to the case of plexcitons, which are hybrid quasiparticles resulting from resonant coupling between excitons and plasmons in metallic nanostructures [33, 34, 35]. By analogy to heavy fermions, we use a common term heavy exciton-polaritons for these quasiparticles to emphasize that they have a large effective mass inherited from a nearly flat dispersion of phonons or plasmons. This is why heavy exciton-polaritons can be confined in nanocavities of size much smaller than the diffraction limit of light. Note that such highly confined heavy polaritons have a very small photonic component. In this regard, we wish to clarify that we use the term 'polariton' in a broad sense, meaning a hybrid excitation of a polarizable medium.

In this chapter, we analyze the Feshbach scattering resonance between heavy polaritons and show that they can form bipolariton states near the resonance. In contrast to previously studied exciton-polaritons in photonic cavities, where paired states are essentially biexcitons, heavy polaritons retain their hybrid nature in the bound state [Fig. 2.1(c)] assuming that Rabi frequency exceeds the biexciton binding energy. We subsequently consider a system with finite densities of polaritons and bipolaritons that can exhibit Bose condensation and superfluidity. We study possible phases of such a condensate, the polariton superfluid (PSF) and bipolariton superfluid (BSF) [36, 37, 38, 39], and the associated excitation spectra within a mean-field approximation.

The rest of this chapter is organized as follows. In Sec. 2.2 we first discuss single-particle states and compare heavy exciton-polaritons to photon exciton-polaritons. We then include exciton-exciton interactions and show how bipolariton states emerge near

the Feshbach resonance. In the last part of Sec. 2.2, we study the consequences of heavy bipolariton formation in many-body condensates. In Sec. 2.3, we compute the absorption and luminescence spectra of the polariton systems and show that they are dominated by collective excitations of the condensate. We discuss additional experimentally testable predictions of our theory in Sec. 5.7. Details of our calculations are provided in the Appendix.

2.2 Model

2.2.1 Single-particle states

We consider a simple model of the heavy polariton that captures the essential physics. The Hamiltonian is

$$H_0 = \sum_{\mathbf{k}} \left[\omega_{x,\mathbf{k}} b_{\mathbf{k}}^\dagger b_{\mathbf{k}} + \omega_{c,\mathbf{k}} a_{\mathbf{k}}^\dagger a_{\mathbf{k}} + \frac{\Omega_{\mathbf{k}}}{2} \left(b_{\mathbf{k}}^\dagger a_{\mathbf{k}} + \text{h.c.} \right) \right], \tag{2.1}$$

which is analogous to what is commonly used to model exciton-polaritons in photonic cavities [13]. In that context the operators $a_{\mathbf{k}}^\dagger$ and $b_{\mathbf{k}}^\dagger$ respectively create cavity mode and exciton states with momentum $\mathbf{k}$. The exciton kinetic energy is $\omega_{x,\mathbf{k}} = k^2/2m_x$, where m_x is the exciton mass. In our case $a_{\mathbf{k}}^\dagger$ creates a phonon or a plasmon (Fig. 2.1) with energy $\omega_{c,\mathbf{k}} = \delta$ independent of $\mathbf{k}$ since the dispersion of a surface optical phonon (plasmon) is nearly flat compared to that of the exciton. We refer to parameter δ as the cavity detuning. The strength of the coupling is characterized by the Rabi frequency $\Omega_{\mathbf{k}}$, i.e., the rate of energy transfer between the two modes, which we take to be momentum independent for simplicity: $\Omega_{\mathbf{k}} = \Omega$. We also ignore the polarization degree of freedom of the exciton. We use units such that $\hbar = 1$ throughout. The spectrum consists of upper and lower polariton

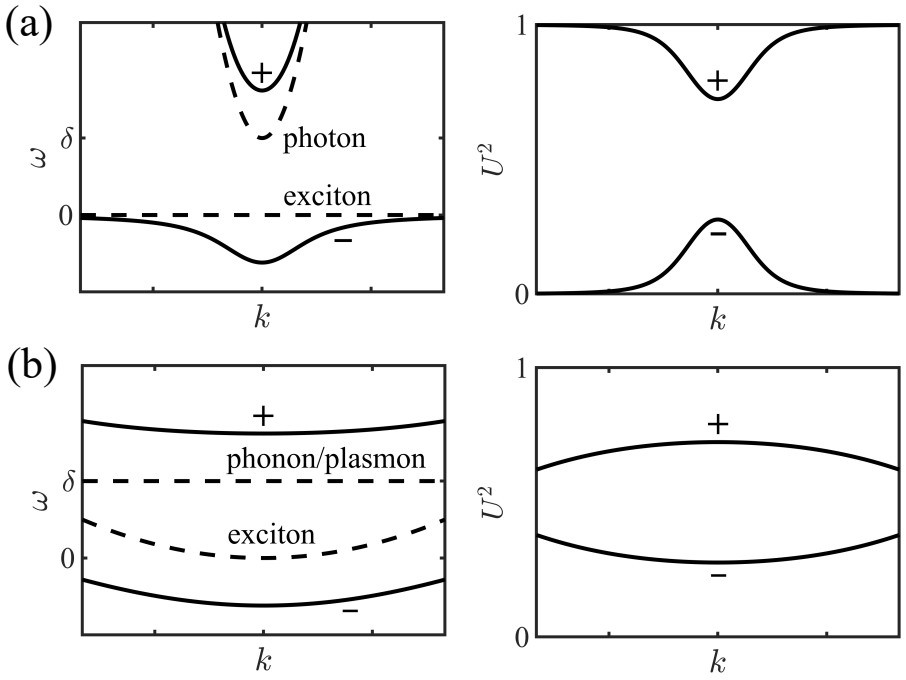

Figure 2.2. Plots of the polariton energy (left) and the exciton fraction (right) versus momentum for (a) photon exciton-polaritons and (b) heavy exciton-polaritons.

branches with energies

$$\omega_{\pm,\mathbf{k}} = \frac{1}{2}\left[\omega_{c,\mathbf{k}} + \omega_{x,\mathbf{k}} \pm \sqrt{(\omega_{x,\mathbf{k}} - \omega_{c,\mathbf{k}})^2 + \Omega_{\mathbf{k}}^2}\right], \tag{2.2}$$

and the exciton fraction in each branch is given by the squares of the Hopfield coefficients

$$U_{\pm,\mathbf{k}}^2 = \frac{1}{2}\left[1 \pm (\omega_{x,\mathbf{k}} - \omega_{c,\mathbf{k}})\Big/\sqrt{(\omega_{x,\mathbf{k}} - \omega_{c,\mathbf{k}})^2 + \Omega_{\mathbf{k}}^2}\right]. \tag{2.3}$$

$$\omega_{c,\mathbf{k}} = \frac{k^2}{2m_c} + \delta \tag{2.4}$$

$$\omega_{x,\mathbf{k}} = \frac{k^2}{2m_x} \tag{2.5}$$

In Fig. 2.2, we compare the momentum dependence of the polariton energy and Hopfield coefficients for conventional photon exciton-polaritons and heavy exciton-polaritons.

Cavity photons have a very steep energy-momentum dispersion which takes the form $\omega_{p,\mathbf{k}} \simeq \delta + k^2/2m_p$, with an effective mass $m_p \sim 10^{-4} m_x$. Therefore, for a photonic cavity, the polaritons have a strong dispersion at small k, but with increasing k outside the light-cone the lower polariton rapidly becomes mostly exciton and the upper polariton becomes mostly photon. This is contrasted with the heavy polaritons which have an effective mass of order the exciton mass m_x and retain their hybrid character at much larger k.

2.2.2 Two-particle states

The interaction between two excitons, viewed as rigid structureless bosons, takes the form

$$H_{\text{int}} = \frac{1}{2A} \sum_{\mathbf{k}\mathbf{k}'\mathbf{q}} W_{\mathbf{q}}\, b^\dagger_{\mathbf{k}+\mathbf{q}} b^\dagger_{\mathbf{k}'-\mathbf{q}} b_{\mathbf{k}'} b_{\mathbf{k}}, \tag{2.6}$$

where A is the area of the system and $W_{\mathbf{q}}$ is an attractive interaction that supports the biexciton bound state. The structureless boson approximation for excitons is justified if their binding energy is much greater than all other relevant energy scales in the problems, including the Rabi frequency, the biexciton binding energy, etc. If this is not true, a more sophisticated formalism is required [40]. The total Hamiltonian is $H = H_0 + H_{\text{int}}$, with H_0 defined in Eq. (2.1). We may estimate the bipolariton binding energy E from the well-known formula for weak attractive interactions in 2D [41]:

$$E \simeq E_\Lambda \exp\left(-\frac{2\pi}{|V_p| m_r}\right), \tag{2.7}$$

with $V_p < 0$ the polariton interaction strength at zero momentum, m_r the reduced mass of the two polaritons forming the bound state, and E_Λ a high-energy cutoff determined by the range of the interaction. For photon exciton-polaritons, $m_r \sim m_p \sim 10^{-4} m_x$, so the binding energy is exponentially small, as mentioned earlier in Sec. 2.1 (see also Appendix A.1). In contrast, for heavy polaritons m_r and V_p are of the same order as those

of the exciton. Therefore, strongly bound bipolaritons are expected near the biexciton resonance. We find the bipolariton energies from the poles of the exciton two-particle scattering matrix. To simplify the calculation we choose $W_{\mathbf{q}}$ to be momentum independent, i.e., a contact interaction, and subsequently eliminate it in favor of the biexciton binding energy E_{xx} to obtain the renormalized scattering matrix $\mathcal{T}(\mathbf{K}, \omega)$, which depends on the total incoming momentum $\mathbf{K}$ and energy ω of the particles. We give an explicit formula for the scattering matrix, along with details of the calculation, in Appendix A.1.

Here and in the following calculations we choose $\Omega = 3E_{xx}$ for the Rabi frequency. In Fig. 2.3(a) we plot the bipolariton energies versus cavity detuning δ. There are two Feshbach resonances. The first one occurs when the energy of a biexciton (the horizontal dotted line) conincides with the energy of two lower polaritons (the lower boundary of the continuum), $2\omega_- = -E_{xx}$, all at momenta $\mathbf{k} = 0$. The second resonance is found where the biexciton energy is equal to the sum of the energies of a lower and upper polariton, $\omega_+ + \omega_- = -E_{xx}$. In both cases there are bipolariton states lying below the continuum of unbound two-particle states, e.g., $\omega = \omega_-(\mathbf{k}) + \omega_-(-\mathbf{k})$. In principle, two upper polaritons can also form a quasi-bound state but it lies in the continuum and is damped. Figure 2.3(b) shows the binding energies and radii of the states outside the continuum versus δ. The bipolariton states become more loosely bound with decreasing δ as the exciton fraction u_-^2 decreases, e.g., for two lower polaritons $m_r \propto u_-^{-2}$ and $V_p \propto u_-^4$, hence their binding energy decreases towards zero in accordance with Eq. (2.7) while their radius diverges.

2.2.3 Phase diagram and excitations

Many-body physics of a system with a finite concentration of polaritons may be described by a two-channel effective Hamiltonian [39] that explicitly includes polariton

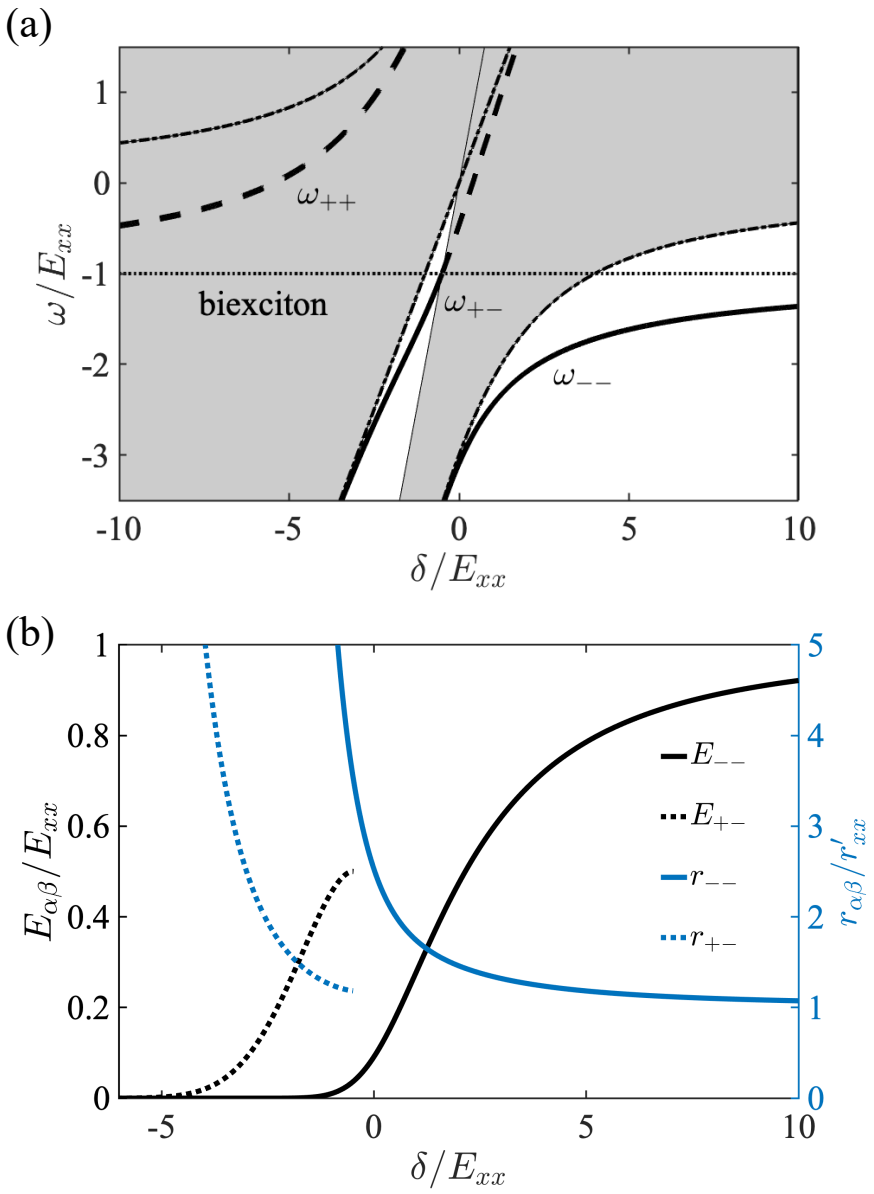

Figure 2.3. (a) Energies of the bipolariton states versus detuning δ for $\Omega = 3E_{xx}$. The solid and dashed black lines are the energies of lower-lower, upper-lower, and upper-upper bipolaritons, denoted respectively by ω_{--}, ω_{+-}, and ω_{++}. The horizontal dotted line is the biexciton energy, the negative of the biexciton binding energy E_{xx}. The dashed-dotted lines are the sum of the energies of two polaritons at zero momentum, with the two-polariton continuum shown by the shaded regions above. (b) The binding energies $E_{--} = 2\omega_- - \omega_{--}$ and $E_{+-} = \omega_+ + \omega_- - \omega_{+-}$ and corresponding radii of the bipolariton states versus detuning δ. The radii $r_{ss'}$ are defined by $r_{ss'}^2 = \int d^2r\, r^2 |\psi_{ss'}(\mathbf{r})|^2$, with $\psi_{ss'}(\mathbf{r})$ the bipolariton wavefunction, and $r'_{xx} = (2/3m_x E_{xx})^{1/2}$ is the biexciton radius for the contact potential model.

(ξ_1) and bipolariton (ξ_2) fields:

$$\begin{aligned} H_{\text{eff}} = &\sum_{i=1,2}\sum_{\mathbf{k}}(\omega_{i,\mathbf{k}}-\mu_i)\xi^\dagger_{i,\mathbf{k}}\xi_{i,\mathbf{k}} \\ &+\frac{1}{2A}\sum_{ij}\sum_{\mathbf{kk'q}} g^{ij}_{\mathbf{kk'q}}\,\xi^\dagger_{i,\mathbf{k+q}}\xi^\dagger_{j,\mathbf{k'-q}}\xi_{j,\mathbf{k'}}\xi_{i,\mathbf{k}} \\ &+\frac{1}{\sqrt{2A}}\sum_{\mathbf{kq}}\left(\alpha_{\mathbf{kq}}\xi^\dagger_{1,\mathbf{q}/2+\mathbf{k}}\xi^\dagger_{1,\mathbf{q}/2-\mathbf{k}}\xi_{2,\mathbf{q}}+\text{h.c.}\right). \end{aligned} \tag{2.8}$$

We assume that only the "−" polaritons, which are the lower energy states, are present. Parameter μ is the chemical potential; $\mu_1=\mu$, $\mu_2=2\mu$; $\omega_{1,\mathbf{k}}=\omega_{-,\mathbf{k}}$ and $\omega_{2,\mathbf{k}}$ [defined by Eq. (2.10) below] are the energies of the polariton and bipolariton, respectively, and α is the polariton-bipolariton coupling. Parameters g^{ij} are repulsive background interactions which depend on the Hopfield coefficents according to

$$g^{ij}_{\mathbf{kk'q}} = U_{-,\mathbf{k}}U_{-,\mathbf{k'}}U_{-,\mathbf{k+q}}U_{-,\mathbf{k'-q}}\tilde{g}^{ij}/m_x, \tag{2.9}$$

and $\tilde{g}^{ij}$ are dimensionless interaction strengths, which we assume to be constant. The parameters α and $\omega_{2,\mathbf{k}}$ are determined by an expansion of the polariton-polariton scattering matrix near the bipolariton pole (see Appendix A.1):

$$T_{--}(\mathbf{k},\mathbf{k'},\mathbf{K},\omega) = U_{-,\mathbf{K/2+k}}U_{-,\mathbf{K/2-k}}U_{-,\mathbf{K/2+k'}}U_{-,\mathbf{K/2-k'}}T(\mathbf{K},\omega)\simeq\frac{\alpha_{\mathbf{kK}}\alpha_{\mathbf{k'K}}}{\omega-\omega_{2,\mathbf{K}}}. \tag{2.10}$$

The system exhibits a transition from a polariton to bipolariton superfluid with changing density and detuning. In the polariton superfluid phase (PSF) both polaritons and bipolaritons condense; in the bipolariton superfluid phase (BSF) only bipolaritons condense. we calculate the mean-field phase diagram at zero temperature using the two-channel model of Eq. (2.8). We caution the reader that these phase diagrams are not

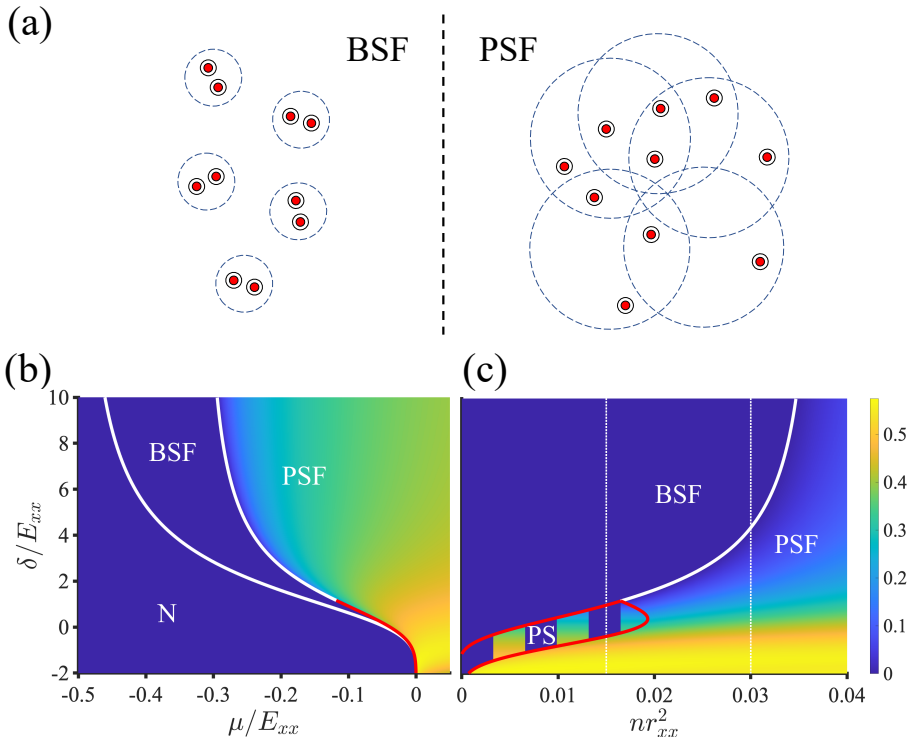

Figure 2.4. (a) Schematic of polariton distribution in the BSF and PSF phases. (b),(c) Ratio of single polariton condensate density to the total density at zero temperature as a function of cavity detuning δ and chemical potential μ (b) or density n (c). The background scattering parameters are $\tilde{g}^{11} = 6$, $\tilde{g}^{12} = 9$, and $\tilde{g}^{22} = 20$. The normal phase is labeled by N, the polariton superfluid by PSF, the bipolariton superfluid by BSF, and phase separated regions by PS.

suitable for immediate comparison with experiment because quantum fluctuations beyond mean-field theory can significantly shift the phase boundaries [39]. Additionally, there is a significant uncertainty in the values of phenomenological parameters $\tilde{g}_{ij}$ (see more below).

We plot the ratio of the single polariton condensate density to the total density in Fig. 5.2(b),(c) [note that $r_{xx} = (1/m_x E_{xx})^{1/2}$], showing the BSF to PSF phase transition with decreasing δ, which can be either first-order or continuous. In the case of a first-order transition, there is a region of phase separation between the PSF phase and the BSF or normal phase. The mean-field phase boundary of the continuous transition is described by

the equation

$$E_{--} = (g_{22}/2 - g_{12})n + \alpha\sqrt{2n}, \tag{2.11}$$

with E_{--} the bipolariton binding energy. This equation relates the total density n to the cavity detuning δ. Note that the parameters $\tilde{g}^{ij}$ are difficult to determine even for simplified microscopic models; furthermore, they depend crucially on details such as the exciton spin structure not included in our simple model. We crudely estimate these parameters by requiring that the BSF-PSF transition occur at a critical density n_M in accordance with the Mott criterion $n_M r_{--}^2 \sim 0.03$ [9, 42]. Here r_{--} is the bipolariton radius which is plotted versus detuning in Fig. 2.3(b). Associated with this criterion is the picture of particle distribution in real space, Fig. 5.2(a). In the BSF phase, polaritons form a dilute gas of bound pairs. As the system approaches the phase transition, the binding energy of these pairs decreases while their radius becomes larger so they begin to overlap in space. As a result, a significant fraction of these pairs dissociate leading to the formation of a single-polariton condensate in addition to the bipolariton condensate in the PSF phase.

As discussed below in Sec. 2.3, the optical response of the PSF and BSF phases is dominated by their collective excitations. The excitation spectrum has one gapless acoustic mode and one gapped mode in each phase [37]. In the BSF phase, the gapless mode is due to phase oscillations of the bipolariton condensate and the gapped mode is due to pair-breaking of bipolaritons into two polaritons. The energy of the gapped mode is

$$E_1^{\mathrm{BSF}} = \left\{ \left[\tfrac{1}{2}(E_{--} - g_{22}n_2 + 2g_{12}n_2) \right]^2 - \alpha^2 n_2 \right\}^{1/2}, \tag{2.12}$$

where n_1 is the single polariton density and n_2 is the bipolariton density. In the PSF phase, the gapless and gapped modes are due to in-phase and out-of-phase fluctuations of

polariton and bipolariton fields, respectively. The energy of the gapped mode is

$$E_1^{\mathrm{PSF}} = \Big\{ \left[E_{--} - g_{12}n_1 - g_{22}n_2 + 2g_{11}n_1 + 2g_{12}n_2 - \alpha\sqrt{n_2}\right]^2 + \alpha n_1 \left[\alpha - 2g_{12}\sqrt{n_1} + (4g_{11} + g_{22})\sqrt{n_2}\right] \Big\}^{1/2}. \tag{2.13}$$

Both E_1^{BSF} and E_1^{PSF} vanish along the phase boundary given by Eq. (2.11). Far from the phase transition, and neglecting the Feshbach coupling α, the energies of the gapped modes have a simple interpretation. We may write $E_1^{\mathrm{PSF}} = \tilde{\omega}_2 - 2\tilde{\omega}_1$, where $\tilde{\omega}_1 = g_{11}n_1 + g_{12}n_2$ and $\tilde{\omega}_2 = -E_{--} + g_{12}n_1 + g_{22}n_2$ are respectively the polariton and bipolariton energies renormalized by interaction. This corresponds to the energy to create a bipolariton. Similarly, $E_1^{\mathrm{BSF}} = \frac{1}{2}(2\tilde{\omega}_1 - \tilde{\omega}_2)$ corresponds to the energy to break a bipolariton into its constituent polaritons.

2.3 Experimental signatures

One way to distinguish PSF and BSF phases is by measuring the optical absorption or luminescence spectrum. The spectrum in both normal and condensed states is determined from the collective excitations of the system, which we calculate from the effective Hamiltonian of Eq. (2.8). Details of the calculation are given in Appendix A.2. There are two contributions: direct coupling of polaritons to photons, which gives rise to sharp emission lines, and coupling of a bipolariton to a photon and polariton, which yields a broad continuum. In Fig. 2.5, we show plots of the absorption and luminescence spectra for a polariton condensate at zero temperature.

The energy of a photon measured in an optical experiment is the sum (difference) of the chemical potential μ and excitation energy corresponding to absorption (emission) of a photon along with emission of a collective excitation. Therefore, the gapless modes follow the lines $\omega = \mu$ (the solid lines in Fig. 2.5), and the gapped modes are positioned above or below these lines. Within the mean-field theory, the chemical potential is given

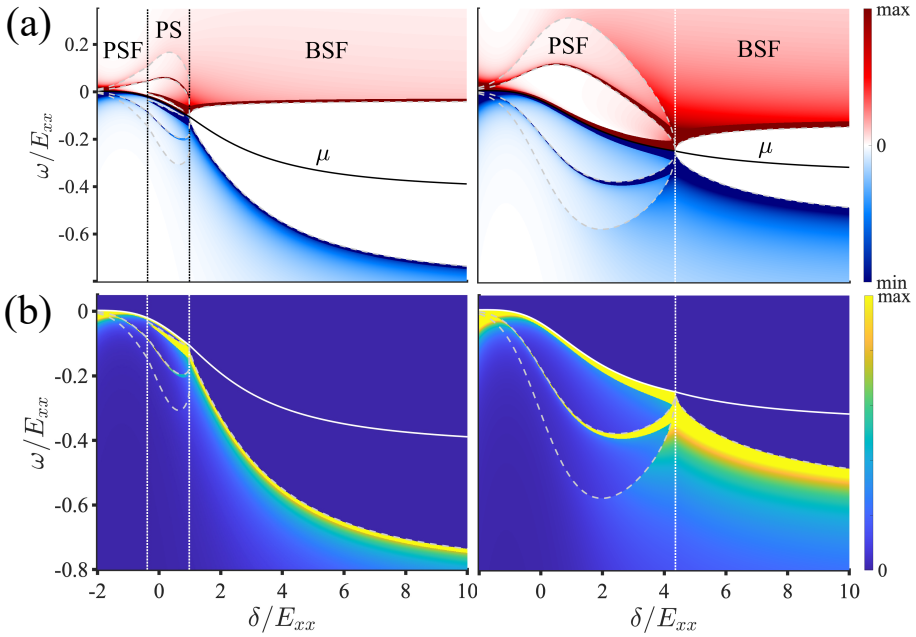

Figure 2.5. (a) Absorption and (b) luminescence spectra at zero temperature for density $nr_{xx}^2 = 0.015$ (left) and $nr_{xx}^2 = 0.03$ (right). The chemical potential μ is denoted by the solid lines, and dashed grey lines indicate thresholds associated with the emission of collective excitations. The absorption spectrum is negative for frequencies below μ, corresponding to optical gain, and positive for frequencies above μ. Since only emission (and not absorption) of collective excitations is possible at zero temperature, luminescence only occurs at frequencies below μ.

by

$$\mu = \begin{cases} g_{11}n_1 + g_{12}n_2 - \alpha\sqrt{n_1 n_2} & \text{(PSF)} \\ \frac{1}{2}(-E_{--} + g_{22}n_2) & \text{(BSF).} \end{cases} \tag{2.14}$$

The energy $\omega = \mu + E_1^{\mathrm{PSF}}$ of the collective mode above μ in the PSF phase and the energy $\omega = \mu - E_1^{\mathrm{BSF}}$ below μ in the BSF phase, can be viewed as the renormalized energy of the bipolariton spectral line. Far from the transition, this energy is given by the formula

$$\omega = \tilde{\omega}_2 - \tilde{\omega}_1 = -E_{--} + (g_{12} - g_{11})n_1 + (g_{22} - g_{12})n_2\,. \tag{2.15}$$

At large positive δ, the system is in the BSF phase, where bipolaritons are energetically favored. The gap between μ and the absorption or emission threshold is the energy of the gapped excitation mode, given by Eq. (2.12). The gapless mode, which is due to phase oscillations of the bipolariton condensate, is not observed in this phase because bipolaritons do not couple directly to light. With decreasing detuning, the gap decreases and closes at the phase transition, where single polariton condensation becomes favorable. In the PSF phase, both gapless and gapped modes are observed. The energy of the gapped mode is given by Eq. (2.13).

We now discuss the relation of our results to previous experiments on the polaritonic Feshbach resonance [19, 20, 21]. Photon exciton-polaritons studied in those experiments have a polarization or pseudo-spin degree of freedom since there are two countercircular polarization states of the photon that couple to excitons with the same polarization. Since the interaction between two excitons is attractive (repulsive) when they have anti-parallel (parallel) spin, only polaritons with anti-parallel spin can form biexcitons. In the experiments, the system is pumped with circularly polarized light to create a condensate of spin-up polaritons. A probe beam with the opposite circular polarization then excites a few spin-down polaritons which interact with the spin-up condensate to form biexcitons.

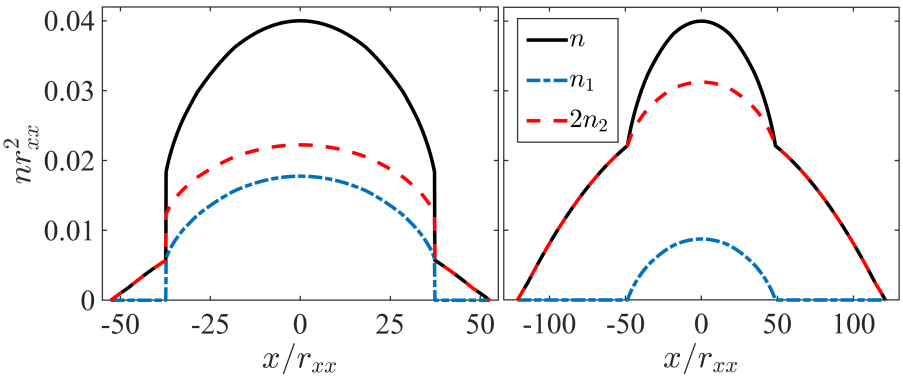

Figure 2.6. Density profiles for polariton condensate in a harmonic trap for first-order transition (left) and continuous transition (right). The plots correspond respectively to $\delta/E_{xx} = 0$ and $\delta/E_{xx} = 2$ in the phase diagram of Fig. 5.2(b). The trap potential is $V(x) = \frac{1}{2}E_{xx}(x/r_{\rm trap})^2$ with $r_{\rm trap} = 300r_{xx}$. Here n_1 is the single polariton density, n_2 is the bipolariton density, and $n = n_1 + 2n_2$ is the total density.

This results in a shift in the spin-down polariton energy observed in the probe transmission spectrum. The shift changes from positive to negative with decreasing cavity detuning as the system is tuned across the Feshbach resonance, which is often colloquially described as the interaction changing from repulsive to attractive. The corresponding effect in our model is the change in the collective mode energy from $-E_1^{\rm BSF}$ to $E_1^{\rm PSF}$ in Fig. 2.5(a) and crossing between the photon energy ω in Eq. (2.15) and chemical potential μ. In other words, the renormalized bipolariton binding energy effectively changes from positive in the BSF phase to negative in the PSF phase. However, the aforementioned experiments have studied a transient state rather than the true ground state of the polariton system, since in principle biexcitons should also condense.

In addition to photoluminescence spectroscopy of a uniform density system, the PSF to BSF transition can be detected by imaging the polariton condensate confined in a trap. In Fig. 2.6, we show the density profile in a harmonic trap calculated in the Thomas-Fermi approximation by solving $\mu[n(r)] + V(r) = \mu_0$ for $n(r)$, where $\mu[n]$ is the local chemical potential as a function of density, $V(r) = \frac{1}{2}E_{xx}(r/r_{\rm trap})^2$ is the trap potential with $r_{\rm trap} = 300r_{xx}$, and μ_0 is the chemical potential at the center of the trap. Since

the local chemical potential $\mu(r)$ decreases with increasing radial coordinate r, there is a transition from the PSF to BSF phase which results in a discontinuity in the density $n(r)$ or its derivative $\frac{dn}{dr}$ for a first-order or continuous transition, respectively. Since μ is continuous across the phase boundary of the continuous transition, $\Delta\mu = 0$, we may relate the discontinuity in $\frac{\partial\mu}{\partial n}$ to that of $\frac{\partial\mu}{\partial\delta}$ by $\Delta\frac{\partial\mu}{\partial\delta} = -\frac{dn}{d\delta}\Delta\frac{\partial\mu}{\partial n}$, with $\frac{dn}{d\delta}$ determined from the phase boundary in Fig. 5.2(c). From Fig. 2.5, $\frac{\partial\mu}{\partial\delta}\big|_{c-} = -0.022$ and $\frac{\partial\mu}{\partial\delta}\big|_{c+} = -0.026$, where $c-$ ($c+$) indicates that the derivative is evaluated just below (above) the transition point. This gives $\Delta\frac{\partial\mu}{\partial\delta} \approx -0.004$, and since $\frac{dn}{d\delta} \approx 0.002/(E_{xx}r_{xx}^2)$, we have $\Delta\frac{\partial\mu}{\partial n} \approx 2E_{xx}r_{xx}^2$. Therefore, $\Delta\big(\frac{dn}{dr}\big)^{-1} = \frac{r_{\rm trap}^2}{E_{xx}r}\Delta\frac{\partial\mu}{\partial n} \approx 10 r_{\rm trap} r_{xx}^2$, which is consistent with the slopes in Fig. 2.6: $\frac{dn}{dr}\big|_{c-} \approx -0.5/(r_{\rm trap}r_{xx}^2)$ and $\frac{dn}{dr}\big|_{c+} \approx -0.05/(r_{\rm trap}r_{xx}^2)$. This explains the large kink seen in the density profile of Fig. 2.6(right) despite the small discontinuity of $\frac{\partial\mu}{\partial\delta}$ in Fig. 2.5.

2.4 Discussion and outlook

We have investigated a novel type of quasiparticle, heavy polaritons, formed by strong coupling of excitons in a 2D semiconductor with surface optical phonons or plasmons. Similar to systems of cold atoms, where this phenomenon was first studied, heavy polaritons exhibit a Feshbach resonance when the biexciton energy becomes resonant with that of two polaritons. Such resonances have been recently probed in experiments with exciton-polaritons in photonic cavities. However, in those experiments the polaritons did not form true bound states. In contrast, we predict that heavy polaritons bind into bipolaritons near the Feshbach resonance. For a system with a finite density of polaritons and bipolaritons we have analyzed the possible phases, polariton (PSF) and bipolariton (BSF) superfluids, and their collective excitations within a mean field approximation. We have computed the absorption and luminescence spectra in these phases.

Another observable signature of polariton condensation is formation of quantized vortices. Such vortices can be induced in the system by external perturbations or non-

equilibrium flow and subsequently detected by optical imaging [43, 44, 45]. of polaritons and bipolaritons induces a splitting of a 2π polariton vortex into two π vortices connected by a domain wall. Observation of this vortex splitting would confirm the existence of the PSF phase.

In conclusion, we briefly mention possible materials realizations of our results. Since phonons have frequencies in the terahertz region, resonantly coupling them to excitons requires a narrow band gap semiconductor. One candidate is gapped bilayer graphene, where tunable excitons have been observed with energies around 100 meV [46, 47]. These excitons can be tuned into resonance with the low-loss hyperbolic phonon modes in hBN [48, 49]. Regarding plasmons, several experiments have demonstrated strong coupling of excitons in TMD monolayers with plasmons in metallic nanostructures [35, 50]. TMDs host strongly bound biexcitons with $E_{xx} \approx 50$ meV [51]. Also, a highly controllable realization of plasmonic strong local coupling with excitons can be achieved using a nano-optical antenna [52, 53]. Note that previously the term heavy polariton has been used to describe hybridization of excitons with 'heavy photons', i.e. flat photonic bands, in an optical lattice [54]. Even though the range of momenta where this band dispersion remains flat is relatively narrow, this could potentially be another path to realization of the physics described in this chapter.

Possible extensions of our work include studying a Josephson-like effect where the optical spectrum in the PSF phase depends on the relative phase of polariton and bipolariton condensates and analyzing the collective modes of the polariton condensate in a trap. A potential application of the heavy polariton Feshbach resonance is the generation of entangled pairs of polaritons [55], which is another interesting subject for future study. In addition, experiments with atomic Bose gases near a Feshbach resonance have observed novel phenomena including Efimov states [56], universal dynamical behavior [57], and formation of solitons [58] or quantum droplets [59]. The system of heavy polaritons studied in this chapter provides another potential avenue to realize these phenomena.

This chapter, in full, is a reprint with permission of the material as it appears in 'B. Vermilyea and M. M. Fogler, Physical Review B **109**, 115401 (2024).' The dissertation author was the primary investigator and author of this paper.

Chapter 3

Landau-phonon polaritons

3.1 Introduction

Another type of phonon exciton-polariton occurs via resonant coupling of optical phonons with magnetoexcitons in a 2D material under a strong transverse magnetic field. These so-called Landau-phonon polaritons (LPPs) are observed experimentally from hybridization of a hyperbolic phonon mode in hBN with magnetoexcitons in graphene [60]. The experiment employs magneto scanning near-field optical microscopy (m-SNOM) to image real-space interference patterns created by LPPs, obtaining a high precision mapping of the LPP dispersion. This in turn allows precise measurements of the many-body corrections to the inter Landau Level (LL) transition energy in graphene for both optically allowed and forbidden transitions. We theoretically calculate these corrections and find excellent agreement with the experimental data. Therefore, the formation of LPPs allows for measurements of the magnetoexciton energy, which is the main subject of this chapter. We use the term LPP both to make a connection with prior literature [61] and to account for the fact that the magnetoexcitons are hybridized with hBN hyperbolic phonons. Additionally, we consider LPPs in a graphene/hBN heterostructure (HS) with N layers of graphene and show a $\sqrt{N}$ enhancement of the polaritonic gap.

The remainder of this chapter is organized as follows. In Sec. 3.2, we review optics of graphene Landau levels (LLs) and explain the details of the experiment. We discuss

our calculation of many-body corrections and compare these results to the experimental data in Sec. 3.3. In Sec. 3.4, we formulate a quantum theory of LPPs in a graphene/hBN HS and derive an analytical expression for the polaritonic gap. A discussion of our results and outlook is given in Sec. 3.5.

3.2 Observation of Landau-phonon polaritons

In a transverse magnetic field, the energy spectrum of graphene splits into Landau levels (LLs) with energy $E_n = \mathrm{sgn}(n)\sqrt{2n}(\hbar v_F/l_B)$, where $n = 0, \pm1, \pm2, \ldots$ is the LL index, v_F is the Fermi velocity, e is the elementary charge, $l_B = \sqrt{\hbar/e|B|}$ is the magnetic length, and B is the magnetic field. This characteristic square-root n- and B-dependence is a consequence of the linear energy-momentum dispersion of electrons in graphene. In a charge-neutral graphene the optical transitions can occur between LLs with indices of opposite sign, $-n \to n'$, at frequencies $\omega \propto \sqrt{|n|} + \sqrt{|n'|}$. The oscillator strength of each inter-LL transition (ILT) is a function of the in-plane momentum k. Conventional far-field infrared experiments excite graphene at very small momentum k, with a non-negligible oscillator strength only at $|n| - |n'| = \pm1$ [62, 63]. However, at finite momenta transitions between any pair of LLs become possible [64].

Each ILT gives rise to a collective excitation, the magnetoexciton [65]. If the magnetoexcitons are tuned in resonance with the hyperbolic phonon-polaritons in hBN by changing the applied magnetic field, the hybrid modes, which are the aforementioned LPPs, can form. The dispersion of the collective modes may be deduced from the frequency and momentum-dependent p-polarized reflection coefficient of the sample, $r_\mathrm{p} = r_\mathrm{p}(k, \omega)$. Figs. 3.1(a)-(c) show the imaginary part of r_p calculated for three representative values of the magnetic field. The multiple branches of phonon-polaritons in the upper Reststrahlen band of hBN (1360-1610 cm^{-1}) are evident in all three cases [66, 48].

At 3.35 T [Fig. 3.1(b)], the frequency of the $-1 \to 2$ ILT is inside the hBN upper

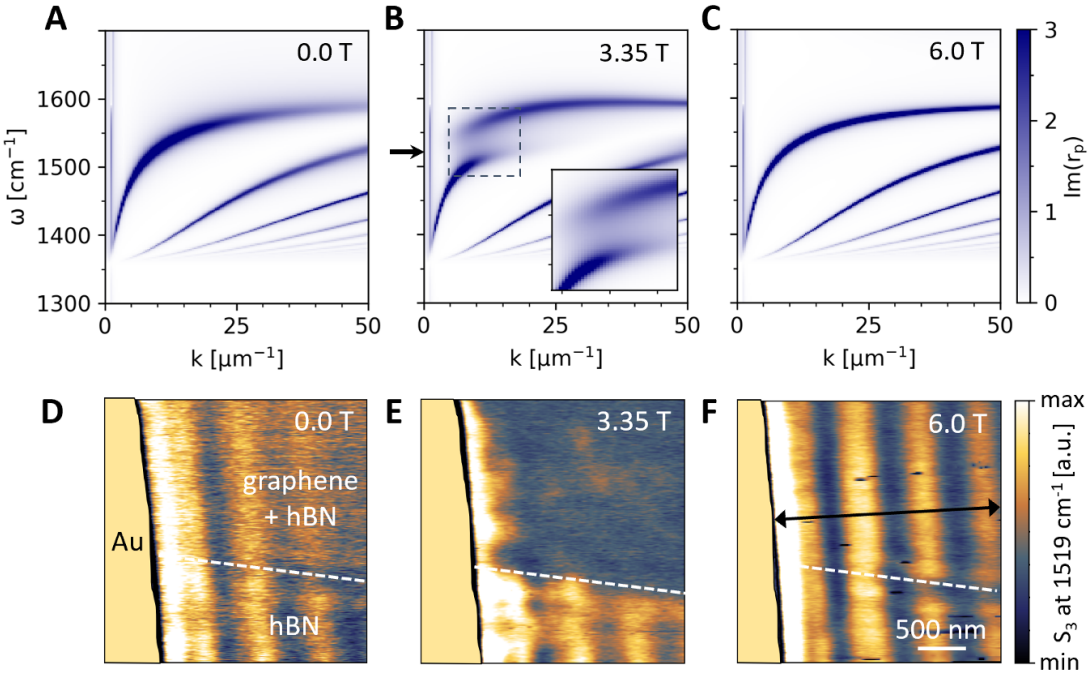

Figure 3.1. Hybridization of hBN phonon polaritons with graphene Landau polaritons, resulting in LPPs. (A to C) Calculated LPP dispersion at magnetic fields of 0.0, 3.35, and 6.0 T, respectively. The false color represents Im $r_p(k, \omega)$, the analytically calculated imaginary part of the reflection coefficient for p-polarized light. Graphene is assumed to be charge neutral with a constant LL broadening (33) $\gamma = 24.3$ cm^{-1} and Fermi velocity $v_F = 1.19 \times 10^6$ m/s, the latter being the value extracted from Fig. 4C. Inset in (B): An enlarged view of the region exhibiting strong coupling and an avoided crossing between the Landau and the hBN phonon polaritons; the arrow marks $\omega = 1519$ cm^{-1} corresponding to the data in (D) to (F). (D to F) Nano-imaging data collected from the region marked by the red rectangle in Fig. 1A at $T = 154$ K and $B = 0.0, 3.35$, and 6.0 T, respectively. The near-field signal S_3 (demodulated at the third harmonic of the tip frequency; refer to Materials and Methods) shows relative differences between regions with and without graphene that strongly depend on the magnetic field. The enhanced signal-to-noise ratio in (E) and (F), compared to (D), is due to a slightly longer integration time. We also note that the mechanical stability of our system is slightly better at higher magnetic fields. The double-headed arrow in (F) marks the location of the line scan analyzed further in Fig. 3. a.u., arbitrary unit.

Reststrahlen band, which generates avoided crossings in the polariton dispersion. These features manifest as a coupling and hybridization of the $1 \rightarrow 2$ inter-LL Landau polariton with the hBN phonon polaritons, i.e., the formation of the LPPs. At 0 T [3.1(a)] and 6.0 T [Fig. 3.1(c)], there are no ILTs inside the Reststrahlen band, so the phonon-polariton dispersion is again largely unaffected by graphene. Figs. 3.1(d)-(f) show m-SNOM images for magnetic fields of B =0.0, 3.35, and 6.0 T, matching Figs. 3.1(a)-(c), respectively, for a fixed incident photon energy. At 3.35 T [Fig. 3.1(e)], the polariton propagation in hBN-graphene ceases such that all but the first fringe is suppressed. This gives clear evidence for the existence of the hybridization gap in the LPP dispersion, i.e., the strong mode coupling, predicted by our theoretical calculations [Fig. 3.1(b)].

To study the magnetic-field dependence of the LPP dispersion in detail, we obtained a field-tip-position map of the m-SNOM signal By sweeping B from -6.0 T to +6.0 T. At our selected photon energy of 188 meV ($\omega = 1519\ \mathrm{cm}^{-1}$) within the hBN Reststrahlen band, we observe the suppression of the fringes for certain distinct field values corresponding to distinct ILTs, e.g., for the discussed case of $B = 3.35$ T for the $-1 \rightarrow 2$ transition. When approaching such fields from a higher (lower) absolute magnetic field side, the polariton wavelength decreases (increases) along with an overall reduction in near-field signal and a decrease of the propagation length.

Fig. 3.2 (a) and (b) show respectively the polariton wavelength and polariton quality factor $Q = \mathrm{Re}\, k/\mathrm{Im}\, k$ extracted from the near-field signal. We find that the features corresponding to the $-1 \rightarrow 2$ transitions are the strongest in our frequency window, testifying to a strong mode coupling regime. In addition, we observe clear signatures of several other transitions. They include allowed transitions $-2 \rightarrow 3$ and $-3 \rightarrow 4$, as well as transitions $-1 \rightarrow 1$, $-2 \rightarrow 2$, and $-3 \rightarrow 3$ forbidden by the standard selection rules. Any of these ILTs also induces a clear modification of the polariton wavelength as well as a reduction of the quality factor, which further supports our assignment and will be used for a quantitative analysis later. In total, we can resolve six different ILTs in our

data. Notably, the forbidden transitions show up much stronger compared to what was previously seen in far-field infrared spectroscopy. As hypothesized above, this massive breakdown of the selection rules originates from the greater role of high-momentum field components $k \sim l_B^{-1}$ in our m-SNOM measurements.

3.3 Many-body effects

Many-body effects manifested in deviations of the ILT frequencies from the $\sqrt{B}$-law valid for free Dirac fermions. An alternative description of these deviations is the renormalization of the effective Fermi velocity v_F^{eff} defined by Eq. (1) below. From the minima in the Q-factor we can read off the magnetic fields B associated with each ILT and obtain the corresponding field-dependent v_F^{eff}. We find that v_F^{eff} decreases with B for all transition types following a non-logarithmic B-dependence (squares in Fig. 3.2(c)). These values agree surprisingly well with previous far-field infrared (31) and Raman (32) spectroscopy results. Importantly, we extract v_F^{eff} associated with both allowed and forbidden ILTs with the same measurement. In this regard, the m-SNOM provides a unified approach for LL spectroscopy that lifts many previous limitations.

Our theoretical calculations (Appendix B) of the effective Fermi velocity (diamonds in Fig. 3.2(c)) show a good agreement with the data utilizing one adjustable parameter, the value of v_F^{eff} at one specific ILT (here, $-2 \to 3$ gives the best agreement). These calculations also corroborate our experimental observation that the effective Fermi velocity of the $-n \to n$ ILTs is consistently below the trend followed by the $-n \to n \pm 1$ ones.

Our explanation for the above observation of v_F^{eff} is as follows: Despite its common usage, the term "effective" Fermi velocity is somewhat misleading in the present context. A more accurate statement is that the interaction corrections to the observed ILT energy $\hbar\omega$, resulting in v_F^{eff}, include contributions from both the Fermi velocity renormalization (a polaronic effect) and excitonic effects. Namely, $\hbar\omega$ is given by the LL energy difference,

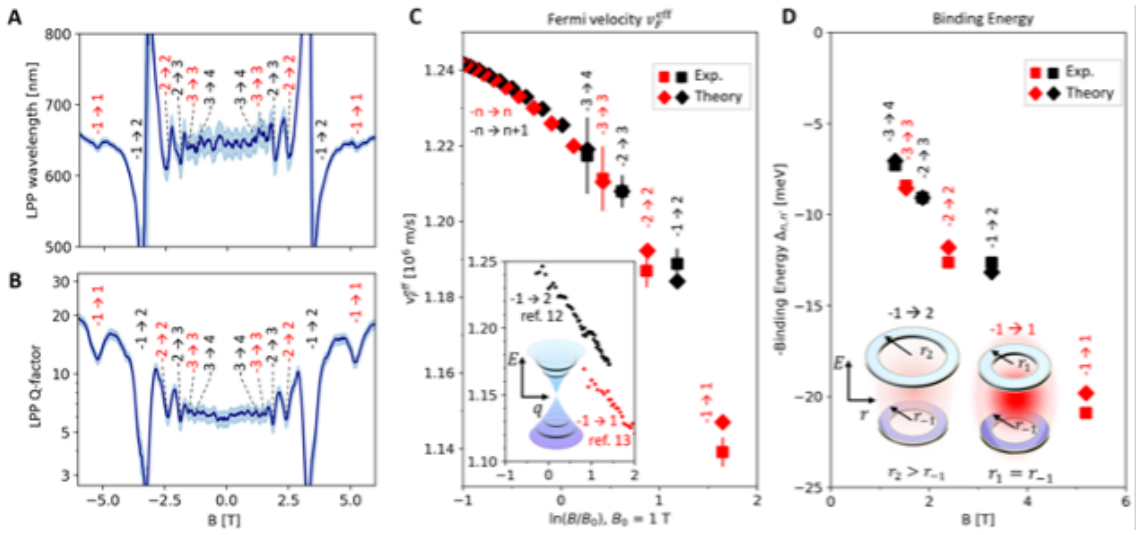

Figure 3.2. Magnetic-field dependence of LPP properties and Fermi velocity renormalization. (A) Polariton wavelength λ_p and (B) polariton quality factor $Q = \mathrm{Re}k/\mathrm{Im}k$ as a function of the magnetic field B. Solid lines show experimental values extracted from Fig. 2; shaded regions show the SD of the measurement. (C) Effective Fermi velocity v_F^{eff} as a function of the logarithmic magnetic field $\ln(B)$ derived for different ILTs (see section Many-body effects): Squares show experimental values derived from (B). Diamonds represent calculated values of v_F^{eff}. [67]. We observe a nonlogarithmic trend. Inset: The red (black) points show v_F^{eff} for the $-1 \to 1$ ($-1 \to 2$) ILT measured via Raman spectroscopy [63] [far-field infrared spectroscopy [62]]. The tapering shape of the Dirac cone illustrates the Fermi velocity renormalization [62, 63, 68], resulting in a logarithmic B dependence of the far-field data [62, 63]. (D) Squares and diamonds show the exciton binding energy $\Delta_{nn'}$ of the Landau polaritons derived from the experiment and theory, respectively. The exciton binding energy is larger for the ILT s with $n' = -n$ compared to those with $n' = -(n \pm 1)$ and generally increases with magnetic field. Inset: The dependence of the exciton binding energy on the magnetic field and type of the ILT can be explained within a semiclassical model where quantized electronic orbitals of the LLs are shaped as narrow rings of radius $r_j = l_B\sqrt{2|j|}$, $j = n$, or n'. The magnetoexciton binding energy $\Delta_{nn'}$ (see text) is given by the Coulomb attraction energy of these rings. For a fixed n, this binding energy is the largest when the ring radii are equal, at $n' = -n$.

$|E_n| + |E'_n|$, minus the magnetoexciton binding energy $\Delta_{nn'}$:

$$\hbar\omega \equiv \frac{\hbar v_F^{\text{eff}}}{l_B}(\sqrt{2|n|} + \sqrt{2|n'|}) = |E_n| + |E'_n| - \Delta_{nn'}. \tag{3.1}$$

The LLs E_n in this expression obey the quantization rule $|E_n| = E(q_n)$ where $E = \hbar v_F^{\text{ren}} q$ is the renormalized quasiparticle dispersion and $q_n = l_B^{-1}\sqrt{2|n|}$ is the quantized momentum of a Dirac fermion residing at the nth LL (inset Fig. 3.2(c)). The effective Fermi velocity v_F^{eff} is (approximately) equal to the renormalized v_F^{ren} only if the magnetoexciton binding energy $\Delta_{nn'}$ is neglected. In that case a logarithmic dependence of v_F^{eff} on E (at fixed n and n') follows from the perturbation theory formula $v_F(E) \approx v_F(\Lambda)[1 + \frac{1}{4}\alpha \ln|\Lambda/E| + \dots]$ where $\alpha = e^2/(\kappa\hbar v_F) \gg 1$ is the Coulomb coupling constant, λ is the high-energy cutoff, and κ is the effective dielectric constant of the graphene environment (34). This formula has been derived for graphene in zero magnetic field; however, it remains approximately correct at nonzero B (Appendix B), meaning that the renormalized Fermi velocity is first and foremost a function of energy, $v_F^{\text{ren}} = v_F^{\text{ren}}(E)$. Since E_n and E'_n are B-dependent (31, 32), v_F^{ren} usually acquires a logarithmic B-dependence for a given ILT, as found in previous far-field spectroscopy studies (inset in Fig. 3.2(d)). On the other hand, here we have studied ILTs at a fixed laser frequency so that the transition energy $\hbar\omega \approx |E_n| + |E'_n|$ remained the same, being split roughly equally between $|E_n|$ and $|E_{n'}|$. Therefore, in our experiments, the renormalized Fermi velocity $v_F^{\text{ren}} \approx v_F^{\text{ren}}(\hbar\omega/2)$ should have little B-field dependence and the observed variation of v_F^{eff} (Fig. 3.2(c)) should mostly come from the change of magnetoexciton binding energy $\Delta_{nn'}$, which follows non-logarithmic trend with changing magnetic field.

Indeed, our theoretical calculation of the two competing terms, $|E_n|+|E'_n|$ and $\Delta_{nn'}$, in Eq. (3.1) confirms that at fixed $\hbar\omega$, the former gives a nearly constant contribution to v_F^{eff} for all measured ILTs, so that v_F^{eff} variation comes from the latter, with characteristic dips occurring at $n' = -n$ points (Appendix B). This allows us to extract the binding energy

$\Delta_{nn'}$ (Fig. 3.2(d)) from v_F^{eff}. The absolute value of $\Delta_{nn'}$ generally increases with magnetic field and is larger for the ILTs with $n' = -n$ compared to those with $n' = -(n \pm 1)$. A simple way to think about the magnetoexciton binding energy $\Delta_{nn'}$ is to imagine that it is equal to the Coulomb attraction energy of two LL orbitals shaped as concentric rings, one with charge $+e$, the other with charge -e (inset Fig. 3.2(d)). The ring radii are given by the formula $r_j = |E_j/ev_F^{\text{ren}}B|$, where $j = n$ or n', which is the semiclassical cyclotron radius of a Dirac particle with energy E_j. (Note additional relations $r_j = l_B\sqrt{2|j|} = l_B^2 q_j$.) For a fixed n, this attraction energy is the largest when the ring radii are equal, i.e., at $n' = -n$, yielding the lowest v_F^{eff} at such ILTs.

3.4 Polaritonic gap in graphene/hBN heterostructure

In addition to allowing precise measurements of the magnetoexciton energy, LPPs are intrinsically interesting as a realization of strong mode coupling. The strength of the coupling can potentially be increased by adding more layers of graphene. In this section, we consider a graphene-hBN heterostructure consisting of N layers of graphene separated by hBN spacers, and show a $\sqrt{N}$ enhancement of the gap. In Appendix C, we derive a quantum theory of LPPs in this HS. We define creation operators $a_{l,\mathbf{q}}^\dagger$ for the hBN hyperbolic phonon mode l with in-plane momentum $\mathbf{q}$, and $b_{i,nm,\mathbf{q}}^\dagger$ for the $m \to n$ graphene magnetoexciton in the ith graphene layer. The Hamiltonian of these coupled modes is

$$H = \sum_{\mathbf{q}} \left[\omega_{l,\mathbf{q}} a_{l,\mathbf{q}}^\dagger a_{l,\mathbf{q}} + \omega_{nm,\mathbf{q}}^x \sum_{i=1}^{N} b_{i,nm,\mathbf{q}}^\dagger b_{i,nm,\mathbf{q}} + \sum_{i=1}^{N} \tfrac{1}{2}\Phi_{l,\mathbf{q}}(z_i)\rho_{nm,-\mathbf{q}}(a_{l,\mathbf{q}} b_{i,nm,\mathbf{q}}^\dagger + \text{H.c.}) \right], \tag{3.2}$$

where $\omega_{l,\mathbf{q}}$ and $\omega_{nm,\mathbf{q}}^x$ are respectively the energies of the hBN phonon mode and graphene magnetoexciton, $\Phi_{l,\mathbf{q}}(z_i)$ is the normalized electrostatic potential profile of the phonon mode at the position of the ith graphene layer z_i, and $\rho_{nm,-\mathbf{q}}$ is the charge density matrix

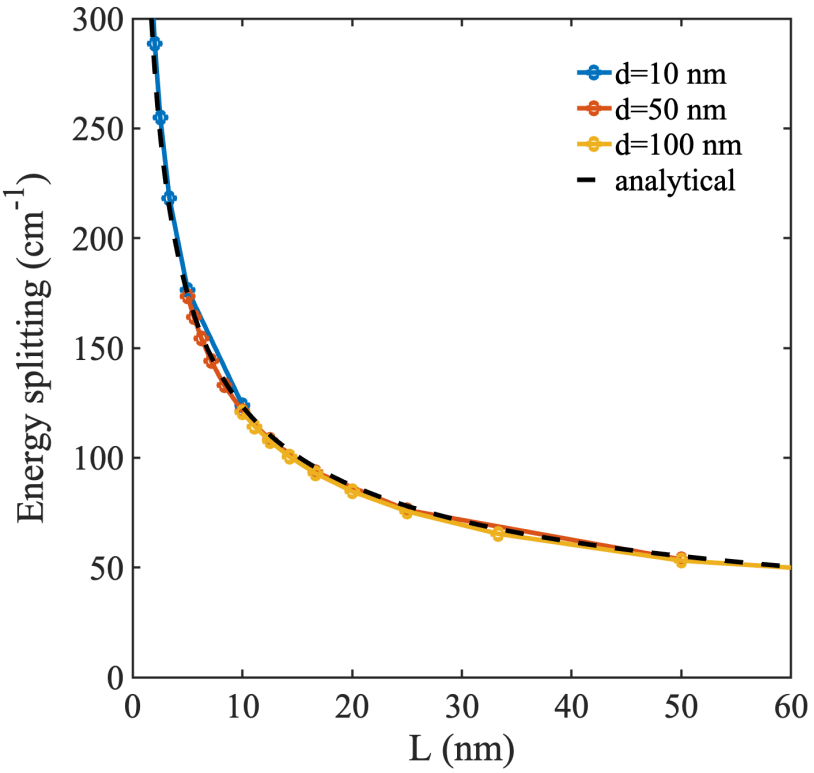

Figure 3.3. Polaritonic energy splitting versus graphene layer spacing L in graphene-hBN HS. The dashed line is the analytical formula of Eq. (3.3), and the other lines show numerical results for fixed hBN thicknesses $d = 10, 50$, and 100 nm with different number of graphene layers.

element associated with the ILT. Diagonalizing this Hamiltonian, we find upper and lower LPP branches and obtain the following approximate expression for the polaritonic gap Δ:

$$\begin{aligned} &\Delta = \sqrt{\frac{\mathcal{N}\bar{\mathcal{E}}\mu}{L}}, \quad \mu = 16\pi e^2 F_{nm}/\hbar, \quad \bar{\mathcal{E}} = \tfrac{1}{2}\left\{1 - (2k_e^z d)^{-1}[\sin(2\phi_a) + \sin(2\phi_s)]\right\}, \\ &\mathcal{N} = qd\left(\frac{1}{[-\varepsilon_\perp]}\left\{\left[1 + (\varepsilon_a/\varepsilon_\perp\psi)^2\right]^{-1} + \left[1 + (\varepsilon_s/\varepsilon_\perp\psi)^2\right]^{-1}\right\} + qd\right)^{-1}\left(\frac{d\varepsilon_\perp}{d\omega}\right)^{-1}. \end{aligned} \tag{3.3}$$

Here d is the thickness of the hBN slab, $L = d/N$ is the graphene layer spacing, $\epsilon_\perp$ and $\epsilon_\parallel$ are the hBN dielectric functions perpendicular and parallel to the optical axis, respectively, ϵ_s is the substrate dielectric constant, and ϵ_a is the dielectric constant of the medium above hBN. We also define $\psi = \frac{\sqrt{\varepsilon_\parallel}}{i\sqrt{\varepsilon_\perp}}$, $k_e^z = q/\psi$, and $\phi_j = \arctan\left(\frac{\varepsilon_j}{\varepsilon_\perp\psi}\right)$ for $j = s, a$ [66]. Matrix

element F_{nm} of the ILT is defined in Eq. (B.7). The dielectric functions are evaluated at the magnetoexciton frequency ω^x_{nm}, and q is the momentum of the hBN phonon mode at this frequency.

The gap scales as $\sqrt{N}$, as expected. Additionally, it scales as $1/\sqrt{d}$ since the coupling strength increases with increasing confinement of the hBN mode. In Fig. 3.3, we plot our formula for the gap Δ versus the graphene layer spacing L for the $l = 0$ phonon mode (for hBN on an SiO_2 substrate) coupled to the $-1 \to 2$ ILT. We compare to numerical results for different hBN thicknesses and number of graphene layers and find good agreement.

3.5 Discussion

Our study has shown that the physics of LPPs is very rich, and it involves simultaneously three types of effects: polaritonic, excitonic, and polaronic. These effects have distinct characteristics: 1) The polaritonic effects change collective mode properties in the heterostructure. Forbidden optical transitions are now accessible in the momentum space offered by m-SNOM. The mode coupling between Landau polaritons (magnetoexcitons) in graphene and phonon polaritons in hBN generates a tunable avoided crossing, which, as we have shown, can potentially be further tailored by using other ILTs (e.g., $0 \to 1$ ILT) or multilayer engineering (e.g., adding additional layers of graphene). 2) The excitonic effects are manifestations of the electron-electron interactions. They lead to a finite binding energy, which also modifies the LPP dispersion. This binding energy can be further tuned via dielectric screening engineering. 3) The polaron effect is another term for the renormalization of the quasiparticle dispersion. Although above we emphasized the role of electron-electron interactions as the reason for the renormalization of the Fermi velocity v_F^{ren}, this interaction is screened by hBN. Hence, the interaction of electrons in graphene with phonons in hBN is included implicitly. In our case, v_F^{ren} does not change much with

magnetic field since we keep the incident photon energy the same throughout.

The LPPs are specific examples of magneto phonon resonance (MPR) effects. Other known MPR effects include magneto-polarons [69, 70], dc magneto-transport oscillations [71, 72, 73], and mode splitting in magneto-Raman spectroscopy [74]. Most of them have been studied in bulk crystals or a single material system. It would be interesting to investigate whether these phenomena are affected by finite-momenta LPPs in a 2D heterostructure. Last, it would be desirable to explore a variety of other nano-magneto-optics phenomena using m-SNOM, including chiral edge magnetoplasmons [75, 76, 77], cavity magneto optics [78], magnon polaritons and magnon-phonon polaritons [61, 79], the polaritonic Hofstadter butterfly [80], magnetoexcitons of fractional quantum Hall states [81], and collective modes of stripe phases in partially filled LLs [82].

This chapter, in part, is a reprint with permission of the material as it appears in 'L. Wehmeier, S. Xu, R. A. Mayer, B. Vermilyea, M. Tsuneto, M. Dapolito, R. Pu, Z. Du, X. Chen, W. Zheng, R. Jing, Z. Zhou, K. Watanabe, T. Taniguchi, A. Gozar, Q. Li, A. B. Kuzmenko, G. L. Carr, X. Du, M. M. Fogler, D. N. Basov, and M. Liu, Science Advances **10** (2024).'

Chapter 4

Excitonic Bose-polarons

4.1 Introduction

In this chapter we consider excitonic Bose-polarons: excitons dressed by a surrounding Bose gas. They are observed experimentally with spatially direct excitons immersed in a degenerate Bose gas of spatially indirect excitons in an electron-hole (e-h) bilayer formed in a GaAs semiconductor heterostructure (HS) [83]. We develop a many-body theory of the energies of the attractive and repulsive polaron branches in this system. We determine the parameters of our theory via numerical calculations of exciton and biexciton binding energies, as well as Hartree-Fock estimates of the exciton-exciton scattering amplitude, and find good agreement with the experimental data.

The remainder of this chapter is organized as follows. In Sec. 4.2, we provide an overview of the experimental results. Our calculation of binding energies of various e-h complexes is presented in Sec. 4.3. We discuss our calculations of exciton-exciton interactions in Sec. 4.4. In Sec. 4.5, we discuss the T-matrix theory of Bose polarons. Finally, we develop a phenomenological T-matrix model and compare with the experiment in 4.6.

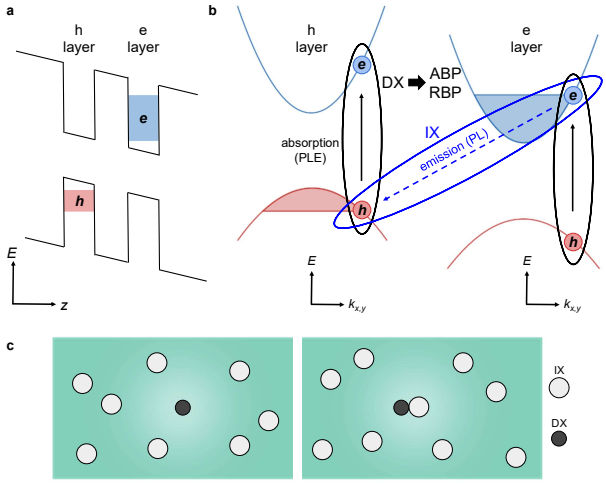

Figure 4.1. Diagram of an electron-hole bilayer. (a) Electrons (e) and holes (h) are confined in separated layers. (b) Absorption (PLE) and emission (PL) in bilayer heterostructure. Spatially indirect excitons (IXs) and direct excitons (DXs) are shown by the ovals. (c) Free DXs (left) and DX-IX bound states (right) interact with surrounding IXs and form attractive and repulsive Bose polarons (ABP and RBP).

4.2 Observation of excitonic Bose-polarons

In this work, we present experiments with electron-hole bilayers in GaAs HS hosting two types of excitons: spatially indirect, or interlayer, excitons (IXs), and spatially direct, or intralayer, excitons (DXs), see Fig. 4.1a,b. The photo-excited DXs behave as polaronic impurities in a degenerate Bose gas of IXs, Fig. 4.1c. We observe spectroscopic signatures of two kinds of such polarons: attractive and repulsive Bose polarons (ABPs and RBPs, respectively). The ABPs are the stable low-energy polaron quasiparticles whereas RPBs are the long-lived excited states in the many-body continuum.

Semiconductor HS's containing e-h bilayers are suited for studying ultracold neutral e-h matter (Fig. 4.1a). The layer separation drastically increases e-h recombination lifetimes, which allows such systems to reach low-temperature quasi-equilibrium states even under optical excitation [84]. As summarized in Ref. [9], e-h bilayers can exhibit a variety of quantum phases, depending on the two key parameters: dimensionless density

$na_{\rm X}^2$ and dimensionless layer separation $d/a_{\rm X}$. Here $a_{\rm X} = \hbar^2\kappa/(\mu_{\rm e-h}e^2)$ is the exciton Bohr radius, κ is the dielectric constant of the semiconductor, $\mu_{\rm e-h} = (m_{\rm e}^{-1} + m_{\rm h}^{-1})^{-1}$ is the reduced e-h mass, and $m_{\rm e}$ ($m_{\rm h}$) is the electron (hole) effective mass. In our GaAs system $d = 19\,$nm (center-to-center separation, Fig. 4.1a) is not much larger than $a_{\rm X} \approx 13\,$nm, so the most experimentally relevant phases are as follows. At low densities, $na_{\rm X}^2 \ll 1$, electrons and holes form a Bose-Einstein condensate (BEC) of tightly bound, hydrogen-like IXs [85, 43]. At moderate densities, $na_{\rm X}^2 \sim 1$, IXs become weakly bound and Cooper-pair-like, so that the BEC crosses over to a Bardeen-Cooper-Schrieffer (BCS) state [86, 87, 88]. At high density, $na_{\rm X}^2 \gg 1$, the IX binding energy is exponentially small (or perhaps, zero), so that the state of the system is best described as a correlated Fermi liquid of electrons and holes. These three regimes can be expressed as the condition on the energy scale

$$E_n = (\pi\hbar^2/\mu_{\rm e-h})n\,, \tag{4.1}$$

which has the meaning of the Fermi edge, i.e., the sum of the Fermi energies of noninteracting electrons and holes. This quantity is much smaller, of the order of, and larger than the IX binding energy $E_{\rm IX} \sim \hbar^2/\mu_{\rm e-h}a_{\rm X}^2$ in the BEC, BCS, and Fermi-liquid regimes, respectively.

The experiments were done with GaAs HS containing two 15 nm-thick quantum wells (QWs) separated by a 4 nm-wide AlGaAs barrier. Electrons and holes were optically generated and their density was controlled by the laser excitation power $P_{\rm ex}$. Electrons and holes were driven into different QWs by an applied voltage (Fig. 4.1a). This significantly increased e-h recombination time, to $\tau \sim 1\mu$s, allowing the system to cool down and form the aforementioned quantum phases.

Previous photoluminescence (PL) studies of this system [88] are consistent with the BEC-BCS crossover occurring with increasing $P_{\rm ex}$. Here we study photoluminescence excitation (PLE) spectra. The PLE signal is a measure of optical absorption in the

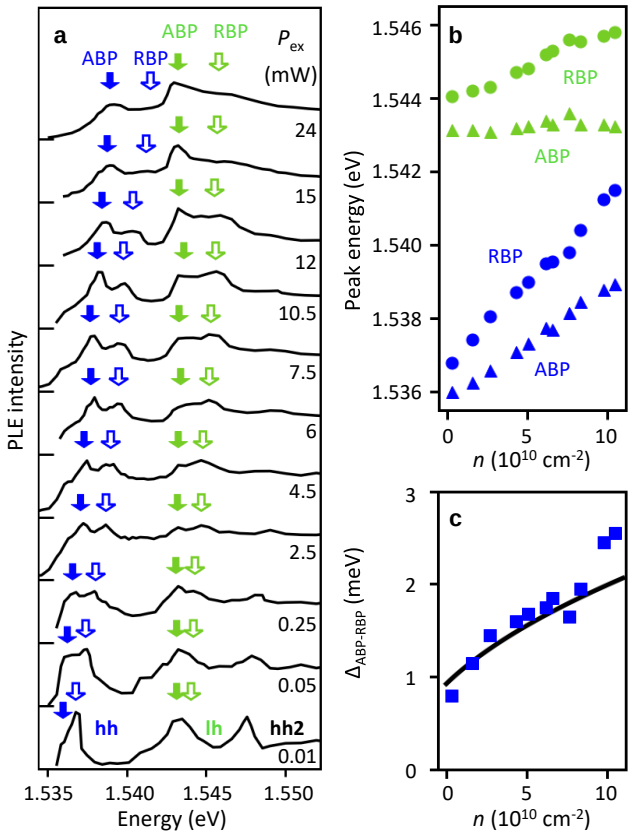

Figure 4.2. Measured PLE spectra. (a) PLE spectra *vs.* the laser excitation power $P_{\rm ex}$ at bath temperature $T = 2\,\mathrm{K}$. The first two peaks in the order of increasing energy correspond to ABP and RBP for DXs containing heavy holes (hh). The next two peaks correspond to ABP and RBP for DXs containing light holes (lh). The higher-energy peaks originate from higher QW subbands. (b) Polaron energies *vs.* IX density (symbols). (c) Measured (squares) and calculated (line) ABP-RBP energy splitting for the hh DXs. The calculations [Eq. (4.42)] use the estimated $E_{\rm XX} = (0.88 + 0.96)/2 = 0.92\,\mathrm{meV}$ and $g_3 = 0.084 \times 10^{-10}\,\mathrm{meV\,cm^2}$.

system. The absorption is dominated by spatially direct (intralayer) optical transitions, e.g., photoexcitation of DXs. Absorption via spatially indirect (interlayer) transitions is much weaker and is not observed. However, the DX density is always much smaller than the IX density due to a fast interlayer e-h relaxation and long IX lifetime [89]. The IX densities in the PLE experiments were estimated to be in the range $n = 0.3{-}11 \times 10^{10}\,\mathrm{cm}^{-2}$. These estimates are based on the measured blue shift δE of the IX PL energy and the "capacitor" formula [90] $\delta E = (4\pi e^2 d/\kappa)\, n$, which becomes increasingly more accurate as n gets larger [89, 91].

Our principal finding is a set of peaks in the PLE spectra, which display a pronounced n-dependence. As labeled in Fig. 4.2a, we attribute the two lowest-energy peaks to ABP and RBP formed from DXs containing heavy holes (hh) and the next pair of peaks those containing light holes (lh). The photo-excited DXs behave as many-body objects dressed by excitations of the surrounding IX Bose gas. As the IX density increases, an approximately linear increase of the ABP and RBP energies (Fig. 4.2b) as well as their splitting $\Delta_{\mathrm{ABP-RBP}}$ (Fig. 4.2c) is observed. This behavior is reproduced within a theoretical model (solid line in Fig. 4.2c) to be discussed in Sec. 4.6. This model treats the DX-IX interaction and phase-space filling [92] (PSF) effects in a unified fashion. According to this model, at low n the RBP evolves into a free DX and the ABP into a DX-IX biexciton, so that the energy splitting $\Delta_{\mathrm{ABP-RBP}}$ should approach the DX-IX biexciton binding energy E_{XX}. There are two possible biexciton types in our CQW, (h-e-h)(e) and (e-h-e)(h), where the parentheses group together particles residing in the same QW. The calculated $E_{\mathrm{XX}} = 0.88$ and $0.96\,\mathrm{meV}$ for, respectively, (h-e-h)(e) and (e-h-e)(h) are close to the measured $\Delta_{\mathrm{ABP-RBP}} = 0.8\,\mathrm{meV}$, see Fig. 4.1c and Sec. 4.3.

Table 4.1. Calculated binding energies of various e-h complexes, in units of meV, for zero gate voltage $V_g = 0$; 'hh' and 'lh' stand for the heavy hole and light hole, respectively.

Complex	QW 1	QW 2	h = hh	h = lh
IX	e	hh	2.99	
DX	e-h		8.24	9.44
DX-IX	e-h-e	hh	0.96	1.26
DX-IX	e	h-e-hh	0.88	0.73

4.3 Exciton binding energies

Few-body e-h bound states that can form in the CQW are listed in Table 4.1, together with their calculated binding energies. They include indirect excitons (IXs), direct excitons (DXs), and DX-IX biexcitons. The details of the calculations are presented below.

The first step of the calculation is to solve for the single-particle states of the QWs. The electron states were determined from the Hamiltonian

$$H_e = \frac{1}{2m_e}\mathbf{P}^2 + U_e(z)\,, \tag{4.2}$$

where z is the coordinate perpendicular to the QW plane, $\mathbf{P} = (\mathbf{p}, -i\hbar\partial_z)$ is the momentum operator, $\mathbf{p} = \hbar\mathbf{k}_\perp$ is the in-plane momentum, and $m_e = 0.0665m_0$ is the effective electron mass in GaAs. The hole states were determined from the Hamiltonian [93, 94]

$$\begin{aligned} H_h &= -\frac{1}{2m_0}\sum_{ij} P_i D_{ij} P_j + U_h(z), \\ \hat{D}_{ij} &= \left(\frac{1}{2}\gamma_1 + \frac{5}{4}\gamma_2\right)\delta_{ij} - \gamma_2 J_i J_j, \end{aligned} \tag{4.3}$$

where γ_1 and γ_2 are the Luttinger parameters, m_0 is the free electron mass, and $\mathbf{J} = (J_x, J_y, J_z)$ is the spin-3/2 angular momentum operator. The confining potentials $U_e(z)$

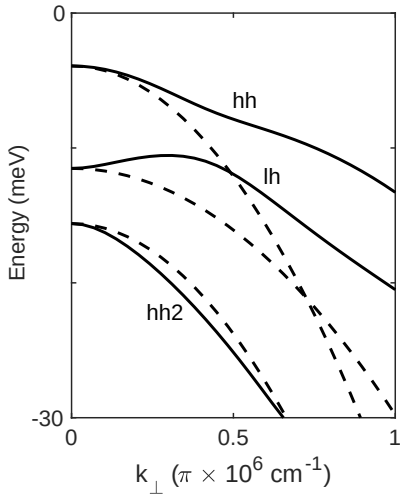

Figure 4.3. In-plane dispersion $\varepsilon_{\rm h}(\mathbf{k}_\perp)$ for the first three hole subbands in units of meV. The dashed lines are the dispersions obtained by neglecting the coupling between heavy and light holes (the off-diagonal terms of H_h).

and $U_{\rm h}(z)$ were chosen in the form

$$U_{\rm e,h}(z) = \begin{cases} 0 & \text{inside QW,} \\ \mathcal{U}_{\rm e,h} & \text{outside QW.} \end{cases} \tag{4.4}$$

For all the parameter values in our calculations we used those given in Ref. 95. We numerically diagonalized the Hamiltonians in Eqs. (4.2) and (4.3) and obtained the energy levels and wavefunctions $\varphi_i(z)$ where $i = {\rm e(h)}n$ for e(h) states of QW $n = 1, 2$. The energy-momentum dispersions of the first three hole subbands are plotted in Fig. 5.6. To facilitate comparison with published results [93, 94] (that appears to be good) the momentum on the horizontal axis is expressed in units of $\pi \times 10^6\,{\rm cm}^{-1}$.

Next, to define the effective mass $m_{\rm h}$ of the heavy hole (hh), we fitted its dispersion to a parabola over a range of momenta $0 < k_\perp < a_{\rm X}^{-1}$, where $a_{\rm X} = (\kappa\hbar^2/e^2)(m_{\rm e}^{-1} + m_{\rm h}^{-1})$ is again the exciton Bohr radius. We found $m_{\rm h} = 0.217m_0 = 3.26m_{\rm e}$, so that $a_{\rm X} = 12.7\,{\rm nm}$.

Note that $a_{\rm X}^{-1}$ is about 0.25 in the momentum units used in Fig. 5.6. The light hole (lh) dispersion is non-monotonic. For simplicity, we decided to neglect this dispersion altogether, i.e., to treat the lh mass as infinite.

To compute the binding energies of interest we approximated the momentum-space Coulomb interaction potential between particles of charge e_i and e_j by

$$\widetilde{V}_{ij}(\mathbf{k}_\perp) = \frac{2\pi e_i e_j}{\kappa k_\perp} \int dz dz' |\varphi_i(z)|^2 \, |\varphi_j(z')|^2 \, e^{-k_\perp |z-z'|} \,, \tag{4.5}$$

which we further simplified as follows. For particles in the same layer, we used [94]

$$\widetilde{V}_{ij}(\mathbf{k}_\perp) = \frac{2\pi e_i e_j}{\kappa k_\perp} \, \frac{1}{1 + k_\perp \rho_{ij}} \,, \tag{4.6a}$$

$$V_{ij}(\mathbf{r}) = \frac{\pi}{2\rho_{ij}} \, \frac{e_i e_j}{\kappa} \, \left[\mathbf{H}_0 \left(\frac{r}{\rho_{ij}} \right) - Y_0 \left(\frac{r}{\rho_{ij}} \right) \right] , \tag{4.6b}$$

where the effective well widths $\rho_{en,en} = 4.5\,\text{nm}$, $\rho_{\text{hn,hn}} = 3.81\,\text{nm}$, and $\rho_{en,\text{hn}} = 4.17\,\text{nm}$ (all for hh), were determined by numerically evaluating the integrals in Eq. (4.5) and fitting the result to Eq. (4.6a) at $0 < k_\perp < a_{\rm X}^{-1}$. Equation (4.6b) is known as the Rytova-Keldysh potential. This function approaches the Coulomb potential $e_i e_j / \kappa r$ at $r \gg \rho_{ij}$ and diverges logarithmically $(e_i e_j / \kappa \rho_{ij}) \ln(\rho_{ij}/r)$ at $r \ll \rho_{ij}$; $\mathbf{H}_0(z)$ and $Y_0(z)$ are the Struve and Neumann functions, respectively.

For particles in opposite layers, we used $\rho_{ij} = 0$, i.e., the Coulomb law:

$$\widetilde{V}_{ij}(\mathbf{k}_\perp) = 2\pi \frac{e_i e_j}{\kappa k_\perp} \, e^{-k_\perp d}, \tag{4.7a}$$

$$V_{ij}(\mathbf{r}) = \frac{e_i e_j}{\kappa} \, \frac{1}{\sqrt{r^2 + d^2}} \,, \tag{4.7b}$$

where $d = 19\,\text{nm}$ is the center-to-center layer distance. These interlayer and intralayer potentials are plotted in Fig. 4.4. We neglected intersubband mixing because the energy separation between the subbands is relatively large, 5–7 meV, see Fig. 5.6.

We computed the DX and IX binding energies $E_{\rm X}$ and ground-state wavefunctions $\phi_{\rm X}(\mathbf{k}_\perp)$ by numerically solving the Wannier equation,

$$[\varepsilon_{\rm e}(\mathbf{k}_\perp)+\varepsilon_{\rm h}(\mathbf{k}_\perp)]\phi_{\rm X}(\mathbf{k}_\perp)+\Omega^{-1}\sum_{\mathbf{k}'_\perp}\widetilde{V}_{ek,{\rm h}n}(\mathbf{k}_\perp-\mathbf{k}'_\perp)\phi_{\rm X}(\mathbf{k}'_\perp)$$
$$=-E_{\rm X}\phi_{\rm X}(\mathbf{k}_\perp) \tag{4.8}$$

following Ref. 96. Here $\mathrm{X}\in\{\mathrm{DX},\mathrm{IX}\}$ is the exciton type, $\varepsilon_{\rm e,h}(\mathbf{k}_\perp)=\hbar^2\mathbf{k}_\perp^2/2m_{\rm e,h}$ are the e(h) dispersions, and Ω is the area of the system.

Finally, we calculated the biexciton binding energies using the stochastic variational method (SVM), a highly accurate numerical technique for solving few-body quantum mechanics problems [97]. To this end we adopted the SVM code previously developed [98] for zero-thickness 2D layers ($\rho_{ij}\equiv 0$) and modified it to work with the interaction potential of Eq. (4.6). We also used the SVM solver to verify the exciton binding energies $E_{\rm X}$ computed by the diagonalization method and found them to be in excellent agreement. Table 4.1 summarizes the results for all the binding energies we calculated.

4.4 Exciton-exciton interaction

4.4.1 IX-IX interaction

Theoretical investigations of Bose polarons have been stimulated primarily by experiments with cold atoms. Transferring these methods to excitons must be done with caution because of important differences between two classes of systems. Atoms reach quantum degeneracy at very low temperatures in the nK or μK-range. Since IXs have much smaller mass, their degeneracy temperature $T_{\rm deg}=2\pi T_0$ with $T_0\equiv\hbar^2 n/m$ [9] is many orders of magnitude higher, e.g., $T_{\rm deg}=20\,\mathrm{K}$ for $m=m_{\rm e}+m_{\rm h}=0.285m_0$ and $n=10^{11}\,\mathrm{cm}^{-2}$.

Atoms typically form dilute, weakly nonideal BECs (Bose-Einstein condensates) for

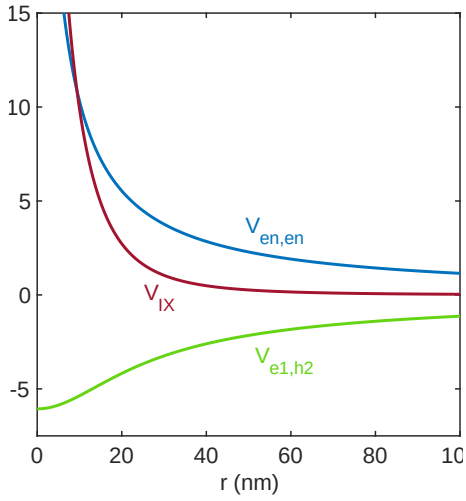

Figure 4.4. Model interaction potentials: intralayer potential $V_{en,en} = V_{hn,hn}$ [Eq. (4.6b)], interlayer potential $V_{e1,h2}$ [Eq. (4.7b)], and the IX-IX potential V_{IX} [Eq. (4.12)].

which the details of the interatomic interaction potential are unimportant. Instead, the interactions are parametrized by the s-wave scattering amplitude, which is proportional to the on-shell two-body T-matrix. In 2D, this T-matrix has a universal low-energy form

$$T(E) \simeq \frac{4\pi\hbar^2}{m}\left[\ln\left(-\frac{\hbar^2}{ma^2}\frac{1}{E}\right)\right]^{-1}, \quad E \to 0, \tag{4.9}$$

where a is referred to as the scattering length. The T-matrix enters in equations for many key quantities of the system. For example, the chemical potential ζ of the BEC is given by

$$\zeta = Tn \tag{4.10}$$

to the leading order in $na^2 \ll 1$. In this equation, T needs to be evaluated at energy $E \sim -\zeta$ [99, 100], so that Eq. (4.10) is a self-consistent equation for ζ as a function of n.

The solution can be presented in the form

$$\tilde{g} \equiv \frac{\zeta}{T_0} = \frac{m}{\hbar^2}\frac{\zeta}{n} \simeq \frac{4\pi}{\ln\left(1/na^2\right)}\,. \tag{4.11}$$

The dimensionless parameter $\tilde{g}$ is a measure of BEC nonideality. For example, it determines the interaction-induced condensate depletion via $\tilde{g}/(2\pi)$ [100]. These formulas apply if $\tilde{g} \lesssim 1$ [101, 102], which translates to the condition on the boson density $na^2 \lesssim 10^{-6}$. Despite the small numerical factor on the right-hand side of this inequality, it is not uncommon to have it fulfilled for cold atoms. In contrast, such densities are unrealistically low for IXs in GaAs heterostructures. As a result, scattering length a is not useful for describing these excitonic systems. Their properties crucially depend on details of the IX-IX interaction and they are typically strongly coupled, $\tilde{g} \gg 1$.

One common model for the interaction potential of two IXs is

$$V_{\mathrm{IX}}(r) = V_{\mathrm{ee}}(r) + V_{\mathrm{hh}}(r) + 2V_{\mathrm{eh}}(r)\,, \tag{4.12}$$

where r is the distance between the centers of mass of the IXs. As one can see from Fig. 4.4, potential $V_{\mathrm{IX}}(r)$ has a strong repulsive core and rapidly decreasing tails. Equation (4.12) is essentially classical, e.g., it neglects fermionic and bosonic exchange of IXs [103] at distances $r \lesssim a_{\mathrm{X}}$. However, due to the strong IX-IX repulsion [104, 98], excitons tend to avoid each other and these exchange effects should be small at densities $n \ll a_{\mathrm{X}}^{-2} \sim 6\times10^{11}\,\mathrm{cm}^{-2}$ studied in our experiments.

At $r \gg d$, the IX-IX potential approaches $V_{\mathrm{IX}}(r) \simeq e^2d^2/\kappa r^3$. The corresponding s-wave scattering length a is given by [102] $a = e^{2\gamma_E}d^2/A_X$, where $\gamma_E = 0.577$ is the Euler constant and $A_{\mathrm{X}} = \hbar^2\kappa/me^2 = 2.3\,\mathrm{nm}$. For $d = 19\,\mathrm{nm}$, we find $a = 500\,\mathrm{nm}$, so that in our

experiments $na^2 \gg 1$. In this regime Eq. (4.11) fails and is replaced by

$$\tilde{g} \equiv \frac{m}{\hbar^2}\frac{\zeta}{n} = \begin{cases} C_g\sqrt{na^2}\,, & n \ll 1/d^2, \quad (4.13a) \\ 4\pi e^{-2\gamma_E}\dfrac{a}{d}\,, & n \gg 1/d^2, \quad (4.13b) \end{cases}$$

which is specific to the interaction law (4.12). The numerical constant $C_g \sim 5$ in Eq. (4.13a) can be estimated from Ref. [91] and work cited therein. Note that Eq. (4.13b) is the same as the 'capacitor formula' introduced in the main text. From these equations, we find $\zeta \sim 30$–$300\,\mathrm{K}$, $T_0 \sim 0.3$–$3\,\mathrm{K}$, and $\tilde{g} \sim 40$–80 in our experiments, indicating that IXs form a strongly correlated Bose gas rather than a weakly nonideal BEC. The large value of $\tilde{g}$ is not a cause for concern; it simply shows that the s-wave scattering length a is not a meaningful control parameter for such dense many-body systems.

4.4.2 DX-IX interaction

The interaction between impurities and host bosons in cold atom gases and in excitonic systems also has some qualitative differences. In the context of cold atoms it is common to describe this interaction using another parameter of dimension of length — the size of the impurity-host dimer. If this length is much larger than the scattering length a of the host bosons, the impurity can attract many host particles. As a result, the ABP becomes a multi-particle cluster with energy much lower than the dimer energy [105]. A related effect is formation of multimers (trimers, quadrimers, *etc.*) in a few-body bosonic systems [106]. In our case, the size of the DX-IX bound state, defined by the relation

$$a_{\mathrm{XX}} = \frac{\hbar}{(2\mu E_{\mathrm{XX}})^{1/2}} \approx 15\,\mathrm{nm}, \quad (4.14)$$

is much smaller than the IX-IX scattering length $a \approx 500\,\mathrm{nm}$. [Here $\mu = (m_{\mathrm{DX}}^{-1} + m^{-1})^{-1}$ is the reduced mass of DX and IX, m is the IX mass, and m_{DX} is the DX mass. We used $E_{\mathrm{XX}} = 1.11\,\mathrm{meV}$, which is the average of the hh and lh values in Table 4.1.] This

means that the IX-IX repulsion is strong compared to the DX-IX attraction. Therefore no multimers or multi-exciton clusters can appear and the excitonic ABP is essentially a dimer.

As mentioned in the main text, the DX-IX bound states, e.g., (e-h-e)(h) biexcitons, which Eq. (4.14) refers to, are stable only when the spins on the two e's form a singlet. The spin dependence of the interaction of the excitons comes from the symmetries of their orbital wavefunctions. It indicates that exchange plays an important role in the DX-IX interaction unlike the case of the IX-IX interaction discussed in Sec. 4.4.1 above.

The exchange effects can be analyzed as follows. Taking the (e-h-e)(h) complex as an example, we note that in GaAs each of the four particles involved can exist in two spin states, $s_z = \pm 1/2$ for the e's and $J_z = \pm 3/2$ for the h's, yielding $2^4 = 16$ combinations total. In this Hilbert space we can select a basis of spin wavefunctions that are either even or odd with respect to interchange of e's or h's. The corresponding orbital wavefunctions must have the opposite parity and therefore different scattering amplitudes. Following Ref. [104], we can describe the DX-IX interaction using four different T-matrices T_v^u, where u and v refer to e and h, respectively, $u, v \in \{\mathrm{s}, \mathrm{a}\}$ and s(a) indicates symmetric (antisymmetric) orbital wavefunction. The $u = v = \mathrm{s}$ channel is a singlet. The spin degeneracy triples if u or v is switched from s to a, so that the original 16-fold degeneracy is split into four channels of spin degeneracy 1, 3, 3, and 9. In the present case, the problem is actually simpler because we can neglect exchange between particles residing in different QWs, e.g., the h-exchange in the (e-h-e)(h) DX-IX complex. Thus, we can disregard the spin of the two h's. We need to consider only the four e-spin states that split into an antisymmetric triplet, described by a T-matrix $T_{\mathrm{a}}^{\mathrm{a}} = T_{\mathrm{s}}^{\mathrm{a}} \equiv T^{\mathrm{a}}$ and a symmetric singlet, characterized by another T-matrix $T_{\mathrm{a}}^{\mathrm{s}} = T_{\mathrm{s}}^{\mathrm{s}} \equiv T^{\mathrm{s}}$.

Some properties of these T-matrices are known from general principles. The triplet channel is non-binding, the singlet channel supports bound state(s). Therefore, $T^{\mathrm{a}}(E)$ is analytic at all negative energies $E < 0$ whereas $T^{\mathrm{s}}(E)$ has a pole at $E = -E_{\mathrm{XX}}$. In the

asymptotic low-energy limit $E \to 0$, both $T^{\rm a}$ and $T^{\rm s}$ have the universal form [cf. Eq. (4.9)]

$$T^u(E) = \frac{\widetilde{V}^u}{1 - L(E)\widetilde{V}^u}, \tag{4.15}$$

$$L(E) = \frac{1}{\Omega} \sum_{|\mathbf{k}|<\Lambda} \frac{1}{E - \varepsilon_{\mathbf{k}} - \varepsilon_{\mathrm{DX},\mathbf{k}}} \simeq -\frac{\mu}{2\pi\hbar^2} \ln\left(-\frac{\hbar^2\Lambda^2}{2\mu E}\right). \tag{4.16}$$

This expression represents the sum of all ladder diagrams for two particles — an IX with dispersion $\varepsilon_{\mathbf{k}} = \hbar^2\mathbf{k}^2/2m$ and a DX with dispersion $\varepsilon_{\mathrm{DX},\mathbf{k}} = \hbar^2\mathbf{k}^2/2m_{\rm DX}$ — interacting via a short-range effective potential $V^u(r)$ such that $\widetilde{V}^{\rm a} > 0$ and $\widetilde{V}^{\rm s} < 0$. Parameter $\Lambda \sim a_{\rm X}^{-1}$ is the high-momentum cutoff. If the binding energy $E_{\rm XX}$ belongs to the range of validity of Eq. (4.15), then $\widetilde{V}^{\rm s}$ can be deduced from the condition that $T^{\rm s}(E)$ has a pole at $E = -E_{\rm XX}$:

$$\widetilde{V}^{\rm s} = -\frac{\hbar^2}{\mu} \frac{\pi}{\ln(\Lambda a_{\rm XX})}, \tag{4.17}$$

which entails

$$\begin{aligned} T^{\rm s}(E) &= \frac{2\pi\hbar^2}{\mu} \left[\ln\left(-\frac{E_{\rm XX}}{E}\right)\right]^{-1} \\ &\simeq \frac{2\pi\hbar^2}{\mu} \frac{E_{\rm XX}}{E + E_{\rm XX}}, \quad E \to -E_{\rm XX}. \end{aligned} \tag{4.18}$$

Accurate calculation of $T^{\rm a}$ and $T^{\rm s}$ at arbitrary energies and momenta requires solving the four-body scattering problem numerically, which goes beyond the scope of the present work. (Currently, our numerical codes can only solve for the bound states, see Sec. 4.3.) However, we can estimate $T^{\rm a}$ and $T^{\rm s}$ by combining Eqs. (4.15), (4.16) with the Hartree-Fock approximation for $\widetilde{V}^{\rm a(s)} = \widetilde{V}_d \pm \widetilde{V}_x$ [103, 92, 104]. Due to the exciton charge neutrality, the Hartree (or direct) term $\widetilde{V}_d$ is negligible compared to the Fock (or e-exchange) term $\widetilde{V}_x$, so that

$$T^{\rm a(s)}(E) \approx \pm \frac{\widetilde{V}_x}{1 \mp L(E)\widetilde{V}_x}. \tag{4.19}$$

The equation for the Fock term is

$$\begin{aligned}
\widetilde{V}_x &= -\int \frac{d^2k}{(2\pi)^2} \int \frac{d^2k'}{(2\pi)^2} W(\mathbf{k},\mathbf{k}')\,, \\
W(\mathbf{k},\mathbf{k}') &= \widetilde{V}_{\mathrm{e1,e1}}(\mathbf{k}-\mathbf{k}')\Phi(\mathbf{k},\mathbf{k}';\mathbf{k},\mathbf{k}') \\
&\quad + \widetilde{V}_{\mathrm{e1,h2}}(\mathbf{k}-\mathbf{k}')\Phi(\mathbf{k},\mathbf{k};\mathbf{k},\mathbf{k}') \\
&\quad + \widetilde{V}_{\mathrm{h1,e1}}(\mathbf{k}-\mathbf{k}')\Phi(\mathbf{k},\mathbf{k};\mathbf{k}',\mathbf{k}) \\
&\quad + \widetilde{V}_{\mathrm{h1,h2}}(\mathbf{k}-\mathbf{k}')\Phi(\mathbf{k},\mathbf{k}';\mathbf{k}',\mathbf{k})\,,
\end{aligned} \tag{4.20}$$

where

$$\Phi(\mathbf{k},\mathbf{q};\mathbf{k}',\mathbf{q}') \equiv \phi^*_{\mathrm{DX}}(\mathbf{k})\phi^*_{\mathrm{IX}}(\mathbf{q})\phi_{\mathrm{DX}}(\mathbf{k}')\phi_{\mathrm{IX}}(\mathbf{q}')\,. \tag{4.21}$$

For comparison with previous work, we can write

$$\widetilde{V}_x = C_x \frac{\hbar^2}{2\mu_{\mathrm{e-h}}}\,, \quad \frac{1}{\mu_{\mathrm{e-h}}} \equiv \frac{1}{m_{\mathrm{e}}} + \frac{1}{m_{\mathrm{h}}}. \tag{4.22}$$

Using $\phi_{\mathrm{DX}}(\mathbf{k})$, $\phi_{\mathrm{IX}}(\mathbf{k})$ found as described in Sec. 4.3, we obtained the numerical coefficients $C_x = 3.81$ for hh and 3.24 for lh. Interestingly, they are only slightly larger than the analytical result $C_x = 4\pi - (315\pi^3/1024) = 3.03$ for the DX-DX interaction in a zero-thickness QW [92]. In physical units, we find

$$\widetilde{V}_x = 0.28 \times 10^{-10}\,\mathrm{meV\,cm^2} \tag{4.23}$$

for (e-h-e)(h) with h = hh.

At this point we can compare the Hartree-Fock estimate $\widetilde{V}^{\mathrm{s}} \approx -\widetilde{V}_x$ with Eq. (4.17). In fact, we can get them to agree perfectly by fixing the numerical factor in the momentum cutoff parameter, making the 'large logarithm' in Eq. (4.17) equal to $\ln(\Lambda a_{\mathrm{XX}}) = 0.59$, which corresponds to $\Lambda = 1.5/a_{\mathrm{X}}$. With this adjustment, Eq. (4.18) for $\widetilde{T}^{\mathrm{s}}$ reproduces the accurate value of the binding energy $E_{\mathrm{XX}} = 0.96\,\mathrm{meV}$ in Table 4.1. It may now be

tempting to use Eq. (4.19) for $\widetilde{T}^{\mathrm{a}}$ with the same Λ. However, doing so would generate a spurious pole in $\widetilde{T}^{\mathrm{a}}(E)$ at a relatively small (by absolute value) energy

$$E = -\left(\frac{\hbar^2\Lambda^2}{2\mu}\right)^2 \frac{1}{E_{\mathrm{XX}}} \approx -10\,\mathrm{meV}\,. \tag{4.24}$$

We believe it is a sign of going beyond the range of validity of the approximation. Therefore, it may be better to revert to the lowest-order perturbation theory formula

$$T^{\mathrm{a}}(E) = \widetilde{V}_x = \mathrm{const}\,. \tag{4.25}$$

We take Eqs. (4.18), (4.23), and (4.25) for two-body DX-IX scattering as the basis for the further analysis of the many-body Bose polaron problem in Sec. 4.6.

4.5 Bose polarons in weakly interacting 2D systems

There have been numerous theoretical studies of Bose polarons in all physical dimensions: 3D, 2D, and 1D. Some examples of methods developed to tackle the 2D case with short-range interactions include the Fröhlich polaron model, which was treated by the Feynman variational method [107] and by perturbation theory [108], a truncated-basis variational approach [109, 110, 111], diffusion quantum Monte-Carlo calculations [112, 105], functional renormalization group theory [113], a T-matrix approximation [114], and variational mean-field (coherent-state) methods, both static and dynamic [115, 116, 117].

The problem of a Bose polaron in a dense excitonic system with realistic interaction laws [such as Eq. (4.12)] has received much less attention. Some nonperturbative calculations within the hypernetted chain method have been reported [91]. Unfortunately, those results are not directly relevant for the present study because of a different geometry of the problem (an e-h quadrilayer instead of the bilayer).

In general, the goal is to find the dispersion $E = E(P)$ of the Bose polarons, which

is determined by the peaks of the spectral function

$$A_{\mathrm{DX}}(P,E) = -2\,\mathrm{Im}\,G_{\mathrm{DX}}(P,E)\,, \tag{4.26}$$

where

$$\begin{aligned} G_{\mathrm{DX}}(P,E) &= -i\int\limits_0^\infty dt e^{iEt/\hbar}\left\langle\left[a_{\mathbf{P}}(t), a_{\mathbf{P}}^\dagger(0)\right]\right\rangle \\ &\equiv \left[E - \frac{\hbar^2 P^2}{2m_{\mathrm{DX}}} - \Sigma(P,E) + i0^+\right]^{-1} \end{aligned} \tag{4.27}$$

is the retarded Green's function of the impurity (in our case, a DX) and $a_{\mathbf{k}}(a_{\mathbf{k}}^\dagger)$ is the impurity creation (annihilation) operators. To analyze the polaron resonances probed in optical experiments it is sufficient to consider $P = 0$ only, and so we suppress the momentum argument P in the formulas below.

Within the T-matrix method the self-energy of the Bose polaron is given by

$$\Sigma(E) = nT(E)\,, \tag{4.28}$$

which is similar to Eq. (4.10). A formula for the T-matrix of a weakly-coupled BEC of spinless bosons has been proposed by Raith and Schmidt (RS) [118]. In our notations, it looks as follows:

$$T(E) = \frac{\widetilde{V}}{1 - L_{\mathrm{RS}}(E)\widetilde{V}}\,, \tag{4.29}$$

$$L_{\mathrm{RS}}(E) = \frac{1}{\Omega}\sum_{|\mathbf{k}|<\Lambda} \frac{u_{\mathbf{k}}^2}{E - \omega_{\mathbf{k}} - \varepsilon_{\mathrm{DX},\mathbf{k}}}\,, \tag{4.30}$$

where

$$\omega_{\mathbf{k}} = \sqrt{\varepsilon_{\mathbf{k}}^2 + 2\zeta\varepsilon_{\mathbf{k}}}\,, \tag{4.31}$$

$$u_{\mathbf{k}} = \frac{1}{2}\left(\sqrt{\frac{\omega_{\mathbf{k}}}{\varepsilon_{\mathbf{k}}}} + \sqrt{\frac{\varepsilon_{\mathbf{k}}}{\omega_{\mathbf{k}}}}\,\right) \tag{4.32}$$

are the Bogoliubov excitation energies and coherence factors. RS derived Eq. (4.29) by summing a subset of ladder diagrams. Identical expressions have been also obtained within the truncated-basis approach [111]. Focusing on the equal-mass case $m_{\mathrm{DX}} = m$, it is easy to show analytically that $L_{\mathrm{RS}}(E) = L(E)$ [cf. Eq. (4.16)]. Hence, these theories predict, surprisingly, that $T(E)$ is no different from the vacuum two-body T-matrix given by Eq. (4.15). Therefore, to adapt this approach to the spinful case, we can use our results from Sec. 4.4.2 and try

$$T(E) = \frac{3}{4}\,T^{\mathrm{a}}(E) + \frac{1}{4}\,T^{\mathrm{s}}(E)\,, \tag{4.33}$$

assuming equal concentrations of all IX spin states.

In our model the triplet term $T^{\mathrm{a}}(E) = \widetilde{V}_x$ is energy-independent, and so it shifts the self-energy by a fixed amount

$$\Delta\Sigma = \frac{3}{4}\,\widetilde{V}_x n\,, \tag{4.34}$$

which is equivalent to a shift of the DX chemical potential. This suggests an improved approximation

$$\begin{aligned}\Sigma(E) &= \Delta\Sigma + \frac{1}{4}\,nT^{\mathrm{s}}(E - \Delta\Sigma) \\ &= \Delta\Sigma + \frac{\pi\hbar^2}{m} n \left[\ln\left(-\frac{E_{\mathrm{XX}}}{E - \Delta\Sigma}\right)\right]^{-1}.\end{aligned} \tag{4.35}$$

(We used $2\mu = m$ in the denominator assuming $m_{\mathrm{DX}} = m$.) The resultant spectral function $A_{\mathrm{DX}}(E)$ has peaks at energies that solve the equation $E = \mathrm{Re}\,\Sigma(E)$. The higher-energy

solution is the RBP:

$$E_{\mathrm{RBP}} \simeq \Delta\Sigma(n) + \frac{\pi\hbar^2}{m}\frac{n}{\ln\left(1/na_{\mathrm{XX}}^2\right)}\,, \quad n \ll a_{\mathrm{XX}}^{-2}\,. \tag{4.36}$$

This equation is different from those previously derived for spinless bosons [108, 105] in two aspects. One is the addition of $\Delta\Sigma(n)$, the other is the extra factor of $1/4$ in the second term. Both differences originate from the electron spin. The 'repulsive' nature of the RBP is manifested in its energy increase with n, which is due to the positive sign of $\mathrm{Re}\,T(E)$. Note that $\mathrm{Re}\,T^{\mathrm{s}}(E) > 0$ at $-E_{\mathrm{XX}} < E < E_{\mathrm{XX}}$, which can be thought of as a 'level repulsion' at energies above the bound-state resonance. At the face value, Eq. (4.36) predicts a diverging E_{RBP} at $n \to 1/a_{\mathrm{XX}}^2$. This is referred to as the strong coupling regime for the Bose polaron. In fact, at large n, this solution of the equation $E = \mathrm{Re}\,\Sigma(E)$ has the asymptotic behavior $E_{\mathrm{RBP}} \simeq \Delta\Sigma(n) + E_{\mathrm{XX}}$.

The lower-energy solution corresponds to the ABP. It depends on n as

$$E_{\mathrm{ABP}} \simeq \Delta\Sigma(n) - \begin{cases} \dfrac{\pi\hbar^2}{m}n + E_{\mathrm{XX}}\,, & n \ll a_{\mathrm{XX}}^{-2}\,, \quad (4.37a) \\ \dfrac{\pi\hbar^2}{m}\dfrac{n}{\ln\left(na_{\mathrm{XX}}^2\right)}\,, & n \gg a_{\mathrm{XX}}^{-2}\,. \quad (4.37b) \end{cases}$$

Note that Eq. (4.37b) is the same as Eq. (4.36). However, the 'reduced energy' $E_{\mathrm{ABP}} - \Delta\Sigma(n)$ now decreases with n, which is a signature of DX-IX attraction.

The DX spectral function computed numerically from Eqs. (4.26), (4.27), (4.34), and (4.35) is plotted in Fig. 4.5(a). To regularize the δ-function-like ABP peak we added a damping constant $-i\Gamma$ to $\Delta\Sigma$. Both the ABP and RBP energies increase with IX density n, in a qualitative agreement with the experiment. The rate of increase is however somewhat smaller. The distance $\Delta_{\mathrm{ABP-RBP}}$ between the two peaks as a function of n is shown in Fig. 4.5(b). The starting point, $\Delta_{\mathrm{ABP-RBP}} = E_{\mathrm{XX}}$ is in a good agreement with the measured value, the subsequent rate of increase is about twice slower. In the

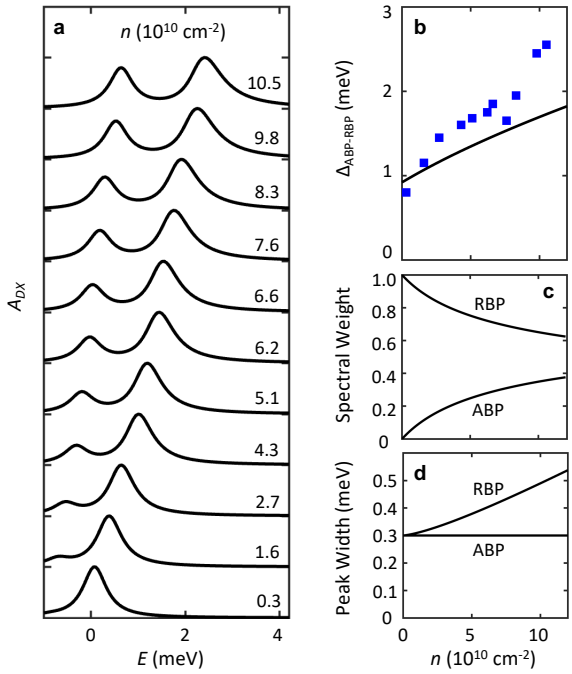

Figure 4.5. (a) Calculated DX spectral function for different n using $E_{\rm XX} = (0.96 + 0.88)/2 = 0.92\,$meV and damping $\Gamma = 0.3\,$meV. The lower-energy and higher-energy peaks correspond to the ABP and RBP, respectively. (b) The ABP-RBP energy splitting deduced from panel (a) (line). The squares are experimental data from Fig. 2 of the main text. (c) ABP and RBP spectral weight vs. n. (d) ABP and RBP peak width vs. n.

context of the polaron problem, the integrated weight (or so-called quasiparticle residue) of the spectral peaks is often discussed. As shown in Fig. 4.5(c), the spectral weight is steadily transferred from the RBP to to ABP as n increases, which is also apparent from Fig. 4.5(a). Finally, in Fig. 4.5(d) we present the evolution of the peak widths. The ABP peak maintains the constant width equal to Γ (which we added by hand). The RBP peak widens with n. This widening originates from the imaginary part of the T-matrix and represents collisional broadening of an unbound DX being scattered by IXs.

The described T-matrix theory is certainly an approximation. It does not capture several additional effects as follows. In Sec. 4.4.2 we suggested that the ABP is essentially a dimer. In fact, the ABP can still be dressed with Bogoliubov-like excitations of the medium, i.e., density oscilations localized near the dimer. Such excitations would produce

spectral weight above the lowest-energy ABP state. This spectral weight can be substantial. In the strong-coupling polaronic regime, it may even exceed that of the ground ABP state. Conversely, for the RBP, which is a metastable state, these local modes typically have negative energies, producing spectral lines below the main RBP peak [119]. Therefore, a non-negligible absorption can be present everywhere in between ABP and RBP energies.

4.6 A phenomenological T-matrix model

The T-matrix theory of Sec. 4.5 gives a qualitative but not quantitative agreement with the experiment. It is also not fully satisfactory for several conceptual reasons. First, Eq. (4.30) disagrees with the perturbation theory formula [120, 108]

$$\Sigma = n\widetilde{V} + \frac{n\widetilde{V}^2}{\Omega} \sum_{|\mathbf{k}|<\Lambda} \frac{\varepsilon_{\mathbf{k}}}{\omega_{\mathbf{k}}} \frac{1}{E - \omega_{\mathbf{k}} - \varepsilon_{\mathrm{DX},\mathbf{k}}} \tag{4.38}$$

already in the order $O(\widetilde{V}^2)$ unlike other theoretical calculations [119, 115], which do agree with Eq. (4.38). The perturbation theory indicates that the response of the BEC to the impurity is suppressed at energy scales below ζ where it behaves as a fairly 'rigid' medium with excitation energies much larger than the bare particle energies, $\omega_{\mathbf{k}} \gg \varepsilon_{\mathbf{k}}$. In contrast, the RS theory [118] and the truncated-basis method [111] (at the single-Bogoliubov-excitation level) predict that the interaction among host bosons practically do not affect the response of the BEC. (If $m_{\mathrm{DX}} = m$, there is no difference at all, see Sec. 4.5.)

Second, as explained in Sec. 4.4.1, the IX system is strongly correlated, so diagrammatic approaches, perturbative or otherwise, are uncontrolled. In the same vein, formulas like Eqs. (4.30) or (4.38) assume unrealistic (extremely short-range) IX-IX interaction law.

It may therefore be prudent to retain only the basic properties of the theory outlined in the previous section and make phenomenological assumptions about all quantities that are difficult to compute reliably. Returning to Eq. (4.35), we can argue that it represents

splitting of the self-energy into a non-singular part with a slow E-dependence and a singular part that has a pole at some energy

$$E^{(0)}_{\mathrm{ABP}} = -E_{\mathrm{XX}} + ng_2\,. \tag{4.39}$$

This leads us to the model:

$$T(E) = g_1 + g_3 \frac{E_{\mathrm{XX}}}{E - E^{(0)}_{\mathrm{ABP}}}, \tag{4.40}$$

which predicts the polaron energies

$$E_{\mathrm{ABP,RBP}} = \frac{1}{2}\left(2ng_1 - E_{\mathrm{XX}} \pm \Delta_{\mathrm{ABP-RBP}}\right), \tag{4.41}$$

$$\Delta_{\mathrm{ABP-RBP}} = \left(E^2_{\mathrm{XX}} + 4ng_3E_{\mathrm{XX}}\right)^{1/2}, \tag{4.42}$$

which agree fairly well with the measured peak energies. Here we already set $g_1 = g_2$ because it is physically reasonable if the DX-IX biexciton is weakly bound and because it helps to reduce the number of phenomenological parameters. This model also predicts the polaron spectral weights (quasiparticle residues)

$$Z_{\mathrm{ABP,RBP}} = \frac{1}{1 - (d\Sigma/dE)} = \frac{1}{2} \pm \frac{1}{2}\frac{E_{\mathrm{XX}}}{\Delta_{\mathrm{ABP-RBP}}}\,, \tag{4.43}$$

which depend on n similar to what is shown in Fig. 4.5(c).

We can use the formulas of Secs. 4.4.2 and 4.5 to crudely estimate g_1 and g_3. For the case of g_1, we take $ng_1 = \Delta\Sigma(n)$, i.e., $g_1 = (3/4)\widetilde{V}_x$, see Eq. (4.34). For g_3, we use Eqs. (4.18) and (4.33) to obtain $g_3 = \pi\hbar^2/2\mu$. These give the estimates $g_1 = 0.21 \times 10^{-10}\,\mathrm{meV\,cm^2}$ and $g_3 = 0.084 \times 10^{-10}\,\mathrm{meV\,cm^2}$ for hh. It is also possible to extract g_1 from the measured peak positions by fitting them to Eqs. (4.41) and (4.42). Doing so for the hh points in Fig. 2b, we obtained $g_1 = 0.34 \times 10^{-10}\,\mathrm{meV\,cm^2}$. A better physical understanding of these

parameter values and other spectral characteristics of the excitonic Bose polarons warrants future experimental and theoretical work.

In summary, we presented spectroscopic evidence for excitonic Bose polarons in electron-hole bilayers. These polarons are many-body objects formed around spatially direct excitons in a degenerate Bose gas of spatially indirect excitons. The energy splitting between attractive and repulsive branches of the Bose polarons grows with the indirect exciton density. We interpreted this behavior within a theoretical model employing the estimated biexciton binding energy and exciton interaction parameters.

The Mott transition (or crossover) from the excitonic to the correlated e-h Fermi liquid regime is expected to occur in our system at high n. The corresponding transition from Bose to Fermi polarons may result [110], which can be an interesting topic for future work.

This chapter, in part, is a reprint with permission of the material as it appears in 'E. A. Szwed, B. Vermilyea, D. J. Choksy, Z. Zhou, M. M. Fogler, L. V. Butov, D. K. Efimkin, K. W. Baldwin, and L. Pfeiffer, Nano Letters **24**, 13219 (2024).'

Chapter 5

Plasmon modes of topological-state networks in twisted bilayer graphene

5.1 Introduction

In this chapter, we study surface plasmons in minimally-twisted gapped bilayer graphene that develops a triangular network of partial dislocations (or AB-BA domain walls) hosting one-dimensional electronic states. The structural and electronic properties of twisted bilayer graphene (TBG) sensitively depend on the twist angle θ. While the emergence of superconducting and insulating phases near the "magic" angle of $\theta \approx 1.1^\circ$ has been extensively studied [5, 6], TBG also exhibits interesting physics at smaller θ. For twist angles below about 1°, i.e. for a minimally twisted TBG (henceforth, mTBG), this material undergoes a structural transformation to form a triangular lattice of energetically-preferred AB and BA stacking domains separated by partial dislocations (also referred to as the domain walls or structural solitons) [121, 122, 123], shown schematically in Fig. 5.1. In the experiment, mTBG is typically subject to an out-of-plane electric field due to external gates or charged impurities. In the presence of such a field, the AB and BA regions develop a bandgap Δ_{TBG} while AB-BA domain walls remain gapless [124]. Each domain wall hosts at least two bound states (per valley, per spin) whose energy dispersions cross the bandgap. These one-dimensional (1D) states are topologically protected and their propagation directions are opposite for the K and K$'$ valleys [125, 126, 127, 128, 129, 130].

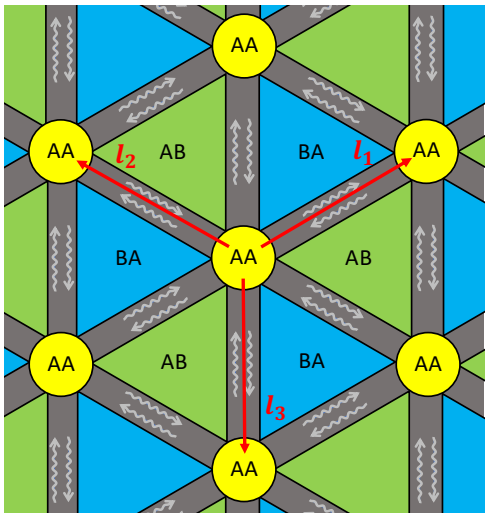

Figure 5.1. A schematic of the mTBG structure at small twist angles. The AB and BA stacking domains are separated by narrow domain walls (links), which intersect at AA regions (nodes). When an interlayer bias is applied, the AB and BA regions are gapped while the domain walls host 1D electronic states. The gray arrows represent 1D plasmons that propagate along the links and scatter at the nodes. The red arrows label the moiré primitive lattice vectors.

The states therefore form a triangular network of 1D conducting channels [123, 131, 132, 133, 134, 135, 136, 137]. The domain walls are the links and their intersections are the nodes (or junctions) of the network, see Fig. 5.1.

Near-field infrared imaging of a doped mTBG [138, 139, 140] revealed that two-dimensional (2D) plasmons in mTBG experience scattering at the domain walls. This observation was attributed to the enhanced local optical conductivity at the domain walls due to the topological 1D states. Direct imaging of these 1D states was not possible in those experiments since the chemical potential was outside the bandgap.

On the theory side, the low-energy electronic band structure of the domain-wall network has been elegantly described by scattering models [141, 142, 143] predicting quasiparticle dispersions $\varepsilon(\mathbf{k})$ that are repeated in energy with the period $\Delta\varepsilon = 2\pi\hbar v/L$. Here $L = |\mathbf{l}_j| = a/[2\sin(\theta/2)]$ is the moiré lattice constant (Fig. 5.1), $a = 0.246\,\mathrm{nm}$ is the in-plane lattice constant of mTBG, and v is the quasiparticle velocity on the

links. Representative band structures for one such model [141] are shown in Fig. 5.3(a). Although realistic electronic structure calculations [133, 136] show more complicated band dispersions, such discrepancies can presumably be accounted for by the energy dependence of the network model parameters. On the other hand, a conceptually important omission of these models is electron-electron interaction. It is known that the low-energy dynamics of interacting 1D electrons is collective [7]. Depending on L and the Fermi energy ε_F, the corresponding range of frequencies in mTBG may extend up to $\sim \Delta_{\mathrm{TBG}}$, i.e., into the terahertz domain. Theoretical understanding of the collective modes, such as 1D plasmons, is necessary to correctly describe the response of the system at such frequencies. Electron-electron interaction effects in TBG networks have been investigated with renormalization group methods [144, 145, 146], but plasmons have not been explicitly addressed.

In this chapter, we develop a theoretical model of plasmons in the mTBG network. We consider two limiting cases depending on the single-particle phase coherence length L_φ [147]. When $L_\varphi \gg L$, the electrons maintain phase coherence upon traversing the links. In this regime, we employ the random phase approximation (RPA) to calculate the network dielectric function and plasmon modes. In the other regime, $L_\varphi \ll L$, the electron phase is randomized due to inelastic scattering. The plasmon modes are determined by a plasmonic network model (PNM) analogous to that for single electrons.

We assume that the dephasing processes are momentum conserving, so that they do not cause plasmonic damping on the links. Therefore, in our PNM, plasmons propagate ballistically along the AB-BA links and scatter only at AA nodes of the network. The interaction mixes plasmons of all propagation directions, so the scattering is governed by a full 6×6 matrix. In particular, the possibility of plasmon backscattering at the nodes is included. This is a key distinction of our model from a related recent work [148] where the plasmons were restricted to propagate only in one particular direction along each link (as in the Chalker-Coddington model for the quantum Hall effect [149]).

Finding the scattering matrix in the PNM is in general a complex problem which

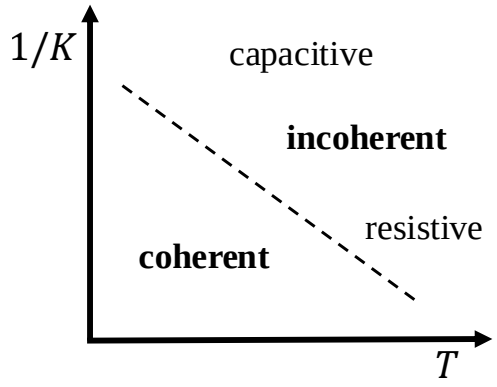

Figure 5.2. Schematic diagram showing different regimes for the network versus temperature T and interaction strength $1/K$, where K is the Luttinger parameter.

depends on the details of inter-link coupling at the nodes and the electron-electron interaction strength. We do not attempt to solve this problem here, but just consider the limiting cases of weak and strong repulsive interactions where the scattering matrix is determined by admittance boundary conditions at the nodes. Interaction strength in 1D may be parametrized by the Luttinger parameter K, where $K = 1$ for non-interacting electrons and $K < 1$ for repulsive interactions [7]. In the weakly interacting limit, $K \to 1$, the junction admittance is purely resistive and determined by the scattering probabilities of single electrons in accordance with the Landauer formula [150]. Therefore, the system behaves as a network of resistors. In the strongly interacting limit, $K \to 0$, this admittance is purely capacitive [151, 152], and the system behaves as a network of capacitors.

Fig. 5.2 shows a schematic "phase diagram" for this system that illustrates the different regimes versus temperature and interaction strength. In each of these regimes, we compute the plasmon spectrum of the network. We find that this spectrum is composed of multiple bands quasi-periodic in frequency, similar to the single-particle problem [141, 142, 143]. Finally, to facilitate their experimental discovery by near-field imaging, we model a near-field response of the network plasmons for a few representative cases. Our theory may also be useful for studying plasmons in artificial networks made from nanotubes or nanowires [153, 154].

The rest of this chapter is organized as follows. We first consider long-wavelength plasmons in Sec. 5.2. In Sec. 5.3, we analyze a model of a 1D periodic chain of scatterers and elucidate the main features of the plasmonic spectrum in different regimes. We formulate a theory of scattering of 1D plasmons at a six-wire junction in Sec. 5.4 and apply it to calculate the plasmon scattering matrix. In Sec. 5.5, we present our calculations of the plasmonic spectrum of the mTBG network in different regimes. We model signatures of the plasmons in near-field images in Sec. 5.6. The concluding discussion is given in Sec. 5.7. Additional details are included in the Appendix.

5.2 Long-wavelength plasmons

We begin by considering plasmons in the long-wavelength limit, where the plasmon wavelength λ_p is much larger than the lattice constant L and the network behaves as a continuous medium with a certain Drude weight D. For a long-range Coulomb interaction, the plasmon dispersion as a function of momentum q, is given by

$$\omega(q) = \sqrt{(2D/\kappa)q}\,, \tag{5.1}$$

with κ being the effective dielectric constant of the mTBG environment, the plasmons have the $\sqrt{q}$ dispersion expected in 2D. We compute D is from the RPA formula:

$$N_c N_d \sum_n \int \frac{d^2k}{(2\pi)^2}\, \delta\left[\varepsilon_n(\mathbf{k}) - \varepsilon_F\right] v_{n,\alpha}(\mathbf{k}) v_{n,\beta}(\mathbf{k}) = \frac{D}{\pi e^2}\, \delta_{\alpha\beta}\,. \tag{5.2}$$

Here $e = -|e|$ is the electron charge, $\varepsilon_n(\mathbf{k})$ is the single-particle energy of momentum $\mathbf{k}$ in the nth band, $\mathbf{v}_n(\mathbf{k}) = \hbar^{-1}\nabla_{\mathbf{k}}\varepsilon_n$ is the corresponding velocity, the integration is taken over the moiré Brillouin zone, $N_d = 4$ is the spin-valley degeneracy, and $N_c = 2$ is the number of channels in addition to this degeneracy. (For simplicity, we assume that all the channels have the same velocity.) We also consider a model where the interaction is

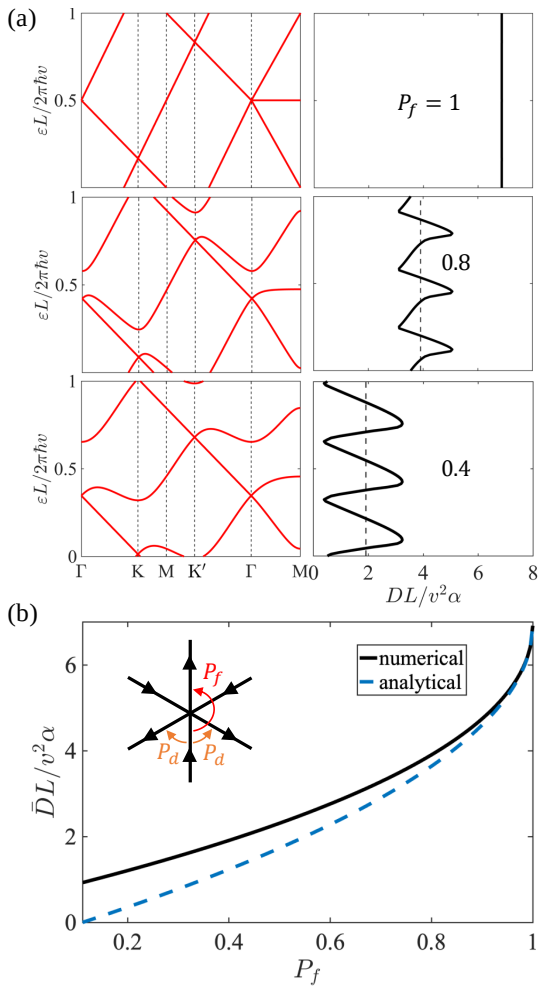

Figure 5.3. (a) Band structure (left) and Drude weight (right) according to the network model of Ref. 141 for forward scattering probability $P_f = 1$ (top), $P_f = 0.8$ (middle), and $P_f = 0.4$ (bottom). The vertical dashed lines indicate the average Drude weight $\bar{D}$. (b) Average Drude weight $\bar{D}$ as a function of the forward scattering probability P_f in this model. The solid line is the numerical result, and the dashed line is the formula of Eq. (5.6). Inset: diagram showing allowed scattering directions.

short-range, which is appropriate if the mTBG resides near a metal gate that screens the long-range Coulomb interaction. The long-wavelength plasmon dispersion is linear in q and has three branches:

$$\omega(\mathbf{q}) = v_i(\hat{\mathbf{q}})q, \quad i = 1, 2, 3, \tag{5.3}$$

where $\hat{\mathbf{q}}$ is the unit vector in the direction of $\mathbf{q}$ and the $v_i(\hat{\mathbf{q}})$ are the solutions of $\det[\epsilon(\hat{\mathbf{q}}, v)] = 0$ for v, where $\epsilon(\hat{\mathbf{q}}, v)$ is a 3×3 matrix with elements

$$\begin{aligned}
\epsilon_{ij}(\hat{\mathbf{q}}, v) &= \delta_{ij} - U_0 P_{ij}(\hat{\mathbf{q}}, v), \\
P_{ij}(\hat{\mathbf{q}}, v) &= \tfrac{\sqrt{3}}{2} N_c N_d \sum_n \int \frac{d^2k}{(2\pi)^2} \frac{M_{ij,n}(\mathbf{k})[\mathbf{v}_n(\mathbf{k}) \cdot \hat{\mathbf{q}}]^2}{v^2 - [\mathbf{v}_n(\mathbf{k}) \cdot \hat{\mathbf{q}}]^2}, \\
M_{ij,n}(\mathbf{k}) &= \delta\left[\varepsilon_n(\mathbf{k}) - \varepsilon_F\right] |\psi_{i,n,\mathbf{k}}|^2 |\psi_{j,n,\mathbf{k}}|^2,
\end{aligned} \tag{5.4}$$

with $\psi_{i,n,\mathbf{k}}$ the wavefunction amplitude on the ith link.

We employ the Efimkin-MacDonald model [141] to find $\varepsilon_n(\mathbf{k})$, as described in Appendix D. Although this model has been generalized to include inter-channel scattering [142], we neglect that here for simplicity. In this approximation, the model has a single parameter: the forward scattering probability P_f. Since the domain wall states are chiral within each valley, and there is assumed to be no intervalley scattering then the Drude weight and the plasmon dispersion should also vary periodically with ε_F. For example, if $v = 10^8\,\mathrm{cm/s}$ and $L = 500\,\mathrm{nm}$, the oscillations with Fermi energy should have a period of $\Delta\varepsilon_F = 8\,\mathrm{meV}$. In Fig. 5.3(a), we plot the band structure and Drude weight for different values of P_f. The Drude weight takes its maximum value

$$D_{\max} = 4\sqrt{3}v^2\alpha/L \tag{5.5}$$

at $P_f = 1$ and decreases with decreasing P_f. Here $\alpha = e^2/\hbar v$ is the Coulomb coupling constant. In terms of the total electron density, the oscillation period is $\Delta n = N_c N_d / A_0$

where $A_0 = \sqrt{3}L^2/2$ is the area of the unit cell of the network. For $L = 500\,\mathrm{nm}$, this period is very small, $\Delta n = 3.7 \times 10^9\,\mathrm{cm}^{-2}$. Hence, detecting such oscillations in experiments would require low disorder, low temperature, and a precise control over the electron density. A more useful quantity is the Drude weight averaged over Fermi energy, $\bar{D}$, which we plot versus P_f in Fig. 5.3(b). For P_f close to 1, we find to leading order the formula

$$\bar{D} = D_{\max}\left(1 - \tfrac{3}{2}\sqrt{P_d}\right), \tag{5.6}$$

with $P_d = \frac{1}{2}(1 - P_f)$ the probability to deflect 120° to neighboring links. The allowed scattering directions are shown in the inset diagram of Fig. 5.3(b).

5.3 1D model

In this section, we analyze a simple 1D model: a periodic chain of identical barriers separated by a distance a. The electrons scatter forward or backward at the barriers and propagate ballistically between them. We discuss the single-particle spectrum for this system, and its plasmonic spectrum calculated via both the RPA and PNM. In terms of the phase coherence length L_φ, the RPA applies when $L_\varphi \gg a$, whereas the PNM applies when $L_\varphi \ll a$.

5.3.1 Single-particle spectrum

Each barrier is characterized by a single-particle scattering matrix which takes the form

$$\mathbf{S}_0 = \begin{pmatrix} r & t \\ t & r \end{pmatrix}. \tag{5.7}$$

Current conservation requires that $\mathbf{S}_0$ is unitary, and therefore the reflection and transmission amplitudes may be parametrized by a single real parameter (the transmission probability $\mathcal{T}$) as $r = -i\sqrt{1-\mathcal{T}}$ and $t = \sqrt{\mathcal{T}}$. Between the scatterers, the electrons

propagate ballistically with velocity v. For a state with energy ε, the wavefunction at position x ($0 < x < a$) in a unit cell may be written as $\left(\psi_R e^{i\varepsilon x/\hbar v}, \psi_L e^{i\varepsilon(a-x)/\hbar v}\right)$, where the two components correspond to right and left moving electrons. At a given momentum k, wavefunction amplitudes on adjacent links differ by a Bloch phase $e^{\pm ika}$, so the incoming and outgoing amplitudes at a node are respectively given by

$$\begin{aligned} \psi_{\text{in}}(k) &= e^{i\varepsilon_k a/\hbar v}\left(\psi_R, e^{ika}\psi_L\right), \\ \psi_{\text{out}}(k) &= \left(\psi_L, e^{ika}\psi_R\right). \end{aligned} \tag{5.8}$$

These are related by the scattering matrix, $\psi_{\text{out}}(k) = \mathbf{S_0}\psi_{\text{in}}(k)$. Therefore, the energies $\varepsilon(k)$ are determined by solving the following eigenvalue problem

$$\begin{pmatrix} te^{-ika} & r \\ r & te^{ika} \end{pmatrix} \begin{pmatrix} \psi_R \\ \psi_L \end{pmatrix} = e^{-i\varepsilon_k a/\hbar v} \begin{pmatrix} \psi_R \\ \psi_L \end{pmatrix}. \tag{5.9}$$

The spectrum consists of two bands that repeat periodically in energy with period $2\pi\hbar v/a$:

$$\varepsilon_{\pm,n,k} = \frac{v}{a}\left[\pm \arccos\left(\sqrt{\mathcal{T}}\cos ka\right) + 2\pi n\right], \tag{5.10}$$

with n an integer. In Fig. 5.4(a), we plot the band structure for $\mathcal{T} = 0.5$.

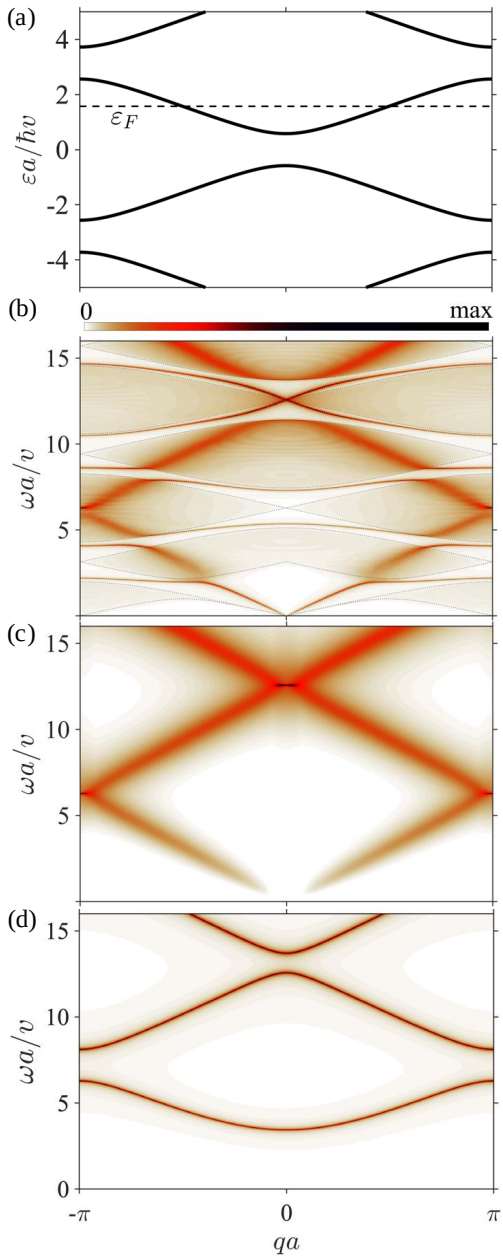

Figure 5.4. (a) The single-particle band structure for transmission probability $\mathcal{T} = 0.7$. The dashed line denotes the Fermi energy used for the RPA calculation below. (b) RPA spectrum. The dotted lines indicate boundaries of the electron-hole continua. The Luttinger parameter is $K = 0.5$. (c) Resistive PNM spectrum for the same parameters. (d) Capacitive PNM spectrum with $\bar{C} = 0.125$.

5.3.2 Random phase approximation

The RPA polarizability is given by

$$\begin{aligned} P_{ll'}(q,\omega) =& \frac{1}{\hbar}\sum_{n,m}\int_{-\pi/a}^{\pi/a}\frac{dk}{2\pi}\rho^{n,m}_{k,q,l}\left(\rho^{n,m}_{k,q,l'}\right)^* \\ & \times\frac{n_F(\varepsilon_{n,k}-\varepsilon_F)-n_F(\varepsilon_{m,k+q}-\varepsilon_F)}{\omega-(\varepsilon_{m,k+q}-\varepsilon_{n,k})/\hbar+i\gamma}, \\ \rho^{n,m}_{k,q,l} =& \int_0^a dx\, e^{-i(q+2\pi l/a)x}\Psi^\dagger_{n,k}(x)\Psi_{m,k+q}(x), \\ \Psi_{n,k}(x) =& \frac{1}{\sqrt{a}}\begin{pmatrix}\psi_{R,n,k}e^{i\varepsilon_{n,k}x/\hbar v}\\ \psi_{L,n,k}e^{i\varepsilon_{n,k}(a-x)/\hbar v}\end{pmatrix}, \end{aligned} \tag{5.11}$$

where l and l' are integers that specify the 1D reciprocal lattice vectors, n and m are band indices, ε_F is the Fermi energy, and $n_F(\varepsilon)=\Theta(-\varepsilon)$ is the Fermi-Dirac function at zero temperature. The wavefunction amplitudes are normalized such that $|\psi_{R,n,k}|^2+|\psi_{L,n,k}|^2=1$. Parameter γ is the line width, and to present our results we take $\gamma=0.01v/a$ in the following calculations. The dielectric function is

$$\epsilon_{\mathrm{RPA},ll'}(q,\omega)=\delta_{ll'}-\tilde{U}(q+2\pi l/a)P_{ll'}(q,\omega), \tag{5.12}$$

with $\tilde{U}(q)$ the 1D Fourier transform of the interaction kernel. The plasmon modes are found from the poles of the inverse matrix $\epsilon^{-1}_{ll'}$. We define the spectral function $S_{\mathrm{RPA}}(q,\omega)=-\mathrm{Im}\sum_l\epsilon^{-1}_{\mathrm{RPA},ll}(q,\omega)$. In our calculation we use a short-range interaction with $\tilde{U}(q)=U_0$ constant, and the interaction strength is defined as $K=(1+(N/\pi)U_0)^{-1/2}$, with N the number of modes [cf. Eq. (5.29)].

In Fig. 5.4(b) we show an example RPA spectral function. The dotted lines indicate the boundaries of the electron-hole continua. Outside these regions, the plasmon modes are sharp spectral lines. As expected, there is a linearly dispersing gapless mode at low frequency with slope v_F/K, where v_F is the Fermi velocity. At higher frequencies there

are interband plasmon modes, which can be explained by the inverse square-root van Hove singularities in the dielectric function at the edges of the continua. If we neglect the off-diagonal elements of $\epsilon_{ll'}$, the interband plasmons would be repelled by the singularities and remain undamped. In the full calculation, they can enter the continua, as seen in Fig. 5.4(b). Additionally, there are undamped modes at the high-symmetry points $q = 0$ and $q = \pi/a$, which are explained by pole-type singularities in $P_{ll'}(q, \omega)$ due to nesting of the single-particle bands. The presence of a sharp mode at such momenta is also obtained within the PNM (see below).

5.3.3 Plasmonic network model

To formulate the PNM, we first need the plasmon scattering matrix, which is derived in Sec. 5.4. It may be expressed in terms of the barrier admittance Y, which relates current through the barrier to voltage across it. In Sec. 5.4 below it will be shown that [Eq. (5.33)] the plasmon reflection and transmission coefficients are, respectively

$$r_p = \frac{K}{K + \bar{Y}}, \quad t_p = \frac{\bar{Y}}{K + \bar{Y}}, \tag{5.13}$$

where $\bar{Y} = \frac{h}{Ne^2} Y$ is the dimensionless admittance. To determine the plasmon modes and their frequencies at momentum q we solve the eigenvalue problem

$$\begin{pmatrix} t_p e^{-iqa} & r_p \\ r_p & t_p e^{iqa} \end{pmatrix} \begin{pmatrix} \phi_R \\ \phi_L \end{pmatrix} = e^{-i\omega_q a/\hbar v_p} \begin{pmatrix} \phi_R \\ \phi_L \end{pmatrix}, \tag{5.14}$$

where ω_q is the mode frequency. This is analogous to Eq. (5.9) but with r and t replaced by r_p and t_p, and the velocity v replaced by the plasmon velocity $v_p = v/K$.

For weak interactions, $\bar{Y} = \frac{\mathcal{T}}{\mathcal{R}}$ according to the Landauer formula [150], with $\mathcal{R} = 1 - \mathcal{T}$ the reflection probability, so the barrier behaves as a resistor. Note that in the

noninteracting case $K = 1$ this implies $r_p = \mathcal{R}$ and $t_p = \mathcal{T}$. The plasmonic bands are

$$\omega_{\pm,n,q} = \frac{v_p}{a}\left[i \ln\left(t_p \cos qa \pm \sqrt{r_p^2 - t_p^2 \sin^2 qa}\right) + 2\pi n\right]. \tag{5.15}$$

Since the scattering matrix is not unitary, $\omega_{\pm,n,q}$ has an imaginary part, which implies dissipation of the plasmon modes. For strong interactions, we have $\bar{Y} = -i(\omega a/v)\bar{C}$, where $\bar{C}$ is the dimensionless capacitance of the barrier. Then the plasmonic spectrum is dissipationless and has a gap ω_0 determined by the solution of

$$\omega_0 = \frac{K}{2\bar{C}} \cot\left(\frac{a}{2v_p}\omega_0\right), \tag{5.16}$$

which lies between 0 and $\pi v_p/a$.

In terms of the plasmon modes, the inverse dielectric function is given by

$$\begin{aligned} \epsilon^{-1}_{\mathrm{PNM},ll'}(q,\omega) &= \sum_n \epsilon^{-1}_{\mathrm{1D}}(\omega_{n,q}/v_p, \omega + i\gamma)\tilde{\Phi}_{n,q,l}\tilde{\Phi}^*_{n,q,l'}, \\ \tilde{\Phi}_{n,q,l} &= \int_0^a dx\, e^{-i(q+2\pi l/a)x}\Phi_{n,q}(x), \\ \Phi_{n,q}(x) &= \phi_{R,n,q}e^{i\omega_{n,q}x/v_p} + \phi_{L,n,q}e^{i\omega_{n,q}(a-x)/v_p}. \end{aligned} \tag{5.17}$$

Here $\Phi_{n,q}(x)$ is normalized so that $\int_0^a dx|\Phi_{n,q}(x)|^2 = 1$.

We show the spectral function $S_{\mathrm{PNM}}(q,\omega) = -\mathrm{Im}\sum_l \epsilon^{-1}_{\mathrm{PNM},ll}(q,\omega)$ in Fig. 5.4(c,d) for resistive and capacitive barriers, respectively. In both cases, the spectrum is quasi-periodic in frequency with period $2\pi v_p/a$, although we only plot one full period. In the resistive case, $\omega_{\pm,n,q}$ is purely imaginary for $|qa| < \arcsin(r_p/t_p)$. In particular, we obtain the low frequency dispersion by expanding $\omega_{+,0,q}$ in $qa \ll 1$:

$$\omega_{+,0,q} = -i\frac{av}{2K^2}\frac{\mathcal{T}}{\mathcal{R}}q^2. \tag{5.18}$$

This corresponds to diffusive motion of electrons with diffusion constant $\mathcal{D} = \frac{1}{2}av\mathcal{T}/\mathcal{R}$. At $qa \sim K\mathcal{R}/\mathcal{T}$, there is a crossover from diffusive motion to damped ballistic motion with velocity v. There is a broadened linearly-dispersing mode with a velocity of approximately v/K, which becomes a sharp mode at high-symmetry points $q = 0$ and $q = \pi/a$. This is because current conservation enforces $r_p + t_p = 1$, so there is no dissipation in the symmetric scattering channel. In the capacitive case, the plasmons are dissipationless at all frequencies, since the admittance is purely imaginary. Furthermore, the spectrum is gapped since the admittance vanishes as $\omega \to 0$.

Comparing Fig. 5.4(b,c), it is apparent that the broad features of the RPA and resistive PNM spectra are similar: both exhibit a broadened specral line with a slope of approximately v/K. However, features seen in the RPA spectrum, such as the electron-hole continua and the sharp interband plasmons outside these continua, as well as the linearly-dispersing gapless mode at low energy, are absent in the PNM spectrum. This is due to loss of phase coherence of the electrons.

We now comment briefly on the validity of our approaches. In the RPA, we compute the irreducible polarizability neglecting electron-electron interactions, as in Eq. (5.11), which ignores both vertex and self-energy corrections to the polarization bubble. At low energy, the RPA predicts that there is a gapless plasmon mode above the intraband continuum [Fig. 5.4(b)]. While it correctly predicts that the velocity of the mode is v/K (see Sec. 5.4), in 1D the continuum below this mode is present only if there are multiple species of electrons (such as due to spin degeneracy). Regarding the intraband excitations, the RPA does not include exciton lines that should exist below the electron-hole continua. In general, the RPA becomes more accurate with increasing dimension d and number of modes N. Applied to the mTBG network, where $d = 2$ and $N = 4$, we believe it should be an adequate approximation in the coherent regime. On the other hand, the PNM should be a good approximation in the incoherent regime. Computing the plasmonic response of the system in a general, partially coherent regime $L_\varphi \sim L$ goes beyond the scope of the

present work but we think the result should be somewhere in between these two limiting cases.

5.4 Plasmon scattering

Assuming $L \gg \lambda_p$, we treat the links of the network as 1D wires. Each link contains $N = 4$ modes, due to the two chiral states per link and the two spin states of the electron. By a "mode" we mean a pair of 1D channels: one from the K valley and its partner from the K′ valley obtained by time-reversal of the orbital motion. To describe the low-frequency long-wavelength dynamics of the system we use the standard bosonization theory [7], as outlined in Appendix E. With a harmonic time dependence $e^{-i\omega t}$ of the fields, the equations of motion for the total density n and current j may be written as

$$-i\omega n(x) + \partial_x j(x) = 0, \tag{5.19}$$

$$-i\omega j(x) = -\frac{Ne^2 v}{\pi\hbar}\partial_x \Phi(x)\,, \tag{5.20}$$

$$\Phi(x) = \frac{\pi\hbar v}{Ne}\, n(x) + \frac{1}{e}\int dx' U(x-x') n(x') + \Phi_{\rm ext}(x)\,. \tag{5.21}$$

Function $\Phi(x)$ has the meaning of the electrochemical potential (or voltage, for short). The first term on the right-hand side of Eq. (5.21) is the local change in the chemical potential, the second term is the electrostatic contribution, and the last term is an external potential, added for completeness.

Function $U(x)$ is the effective 1D interaction kernel. In our calculations later in this section we adopt the approximation

$$U(x) = \frac{e^2}{\kappa}\,\frac{1}{|x| + \ell}. \tag{5.22}$$

Parameter ℓ, which has the meaning of a characteristic width of the wire, cuts off the divergence of the Coulomb law, $U(x) \simeq e^2/\kappa|x|$ at short distances. Note that $\tilde{U}(q) =$

$(e^2/\kappa)\tilde{u}(q)$ with $\tilde{u}(q) \simeq 2\ln(A/q\ell)$ and $A = 0.561$. Here and below the tilde denotes the 1D Fourier transform. For the case that $U(x)$ is short-range due to screening by a metal gate, we have $\tilde{u}(q) = 2\ln(Ad_g/\ell) = \text{const}$ where d_g is the gate-sample distance and $A \sim 1$.

From Eqs. (5.19)–(5.21), it is easy to see that the 1D dielectric function of the system is

$$\epsilon_{1\mathrm{D}}(q,\omega) \equiv \frac{\tilde{\Phi}_{\mathrm{ext}}(q)}{\langle\tilde{\Phi}(q)\rangle} = 1 - \frac{N}{\pi}\,\frac{\tilde{U}(q)}{\hbar v}\,\frac{v^2q^2}{\omega^2 - v^2q^2}\,, \tag{5.23}$$

which is identical to the RPA result for a 1D electron gas with a linearized dispersion. The roots of the dielectric function determine the plasmon spectrum

$$\omega_p(q) = [1 + (N\alpha/\pi)\tilde{u}(q)]^{1/2}\, vq, \tag{5.24}$$

where $\alpha = e^2/(\hbar v\kappa)$ is the dimensionless Coulomb interaction constant. The plasmon dispersion is linear for the case of short-range interaction $\tilde{u}(q) = \text{const}$ and linear with logarithmic corrections for unscreened Coulomb interactions. All these properties are well known.

Consider now a junction of several 1D channels. Let $\Phi_\alpha(r)$ be the voltage on the αth link at a distance r from the node. Following the above treatment, it is straightforward to obtain the equations

$$\Phi_\alpha(r) + \frac{v^2}{\omega^2}\left[\partial_r^2\Phi_\alpha + \frac{N}{\pi\hbar v}\sum_\mu \int dr' U_{\alpha\mu}(r,r')\,\partial_{r'}^2\Phi_\mu\right] = 0, \tag{5.25}$$

$$U_{\alpha\mu}(r,r') = U\left(\sqrt{r^2 + r'^2 - 2rr'\cos\beta_{\alpha\mu}}\right), \tag{5.26}$$

where $\beta_{\alpha\mu}$ is the angle between links α and μ. (The external potential term has been dropped.)

To complete the system of equations we specify boundary conditions with an

admittance matrix $\mathbf{Y}$ relating currents to voltages at the junction:

$$j(0) = \mathbf{Y}\Phi(0), \tag{5.27}$$

with $j(0)$ and $\Phi(0)$ six-component vectors specifying current and voltage on each link, respectively. Equivalently, incoming and outgoing currents are related with a current splitting matrix $\mathbf{M}$ [155]:

$$j^+(0) = \mathbf{M}j^-(0), \tag{5.28}$$

where $j_\alpha^+ = [Ne^2\Phi_\alpha/(\pi\hbar) + j_\alpha]/2$ and $j_\alpha^- = [Ne^2\Phi_\alpha/(\pi\hbar) - j_\alpha]/2$ are respectively outgoing and incoming chiral currents of wire α. The relation between $\mathbf{Y}$ and $\mathbf{M}$ is $\mathbf{Y} = \frac{2Ne^2}{h}(\mathbf{M} + \mathbf{1})^{-1}(\mathbf{M} - \mathbf{1})$. In order to ensure current conservation, each row and column of $\mathbf{Y}$ ($\mathbf{M}$) must sum to zero (one). We also define a dimensionless admittance $\bar{\mathbf{Y}} = \frac{h}{Ne^2}\mathbf{Y}$, which we refer to below.

In general, $\mathbf{Y}$ has a complicated dependence on the Luttinger parameter K which characterizes the strength of the interaction:

$$K(q) = [1 + (N\alpha/\pi)\tilde{u}(q)]^{-1/2} = \frac{vq}{\omega_p(q)}. \tag{5.29}$$

Here we will consider the limits of weak and strong interactions, $K \to 0$ and $K \to 1$, respectively. When interactions are weak, the boundary conditions are determined by the the scattering probabilities of single electrons. This may be simply expressed in terms of

$\mathbf{M}$, whose elements are $M_{ij} = |S_{0,ij}|^2$, with $\mathbf{S}_0$ the single-particle scattering matrix:

$$\mathbf{M} = \begin{pmatrix} \mathbf{M}^{(1)} & \mathbf{M}^{(2)} \\ \mathbf{M}^{(2)} & \mathbf{M}^{(1)} \end{pmatrix},$$
$$\mathbf{M}^{(1)} = \begin{pmatrix} 0 & P_d & 0 \\ P_d & 0 & P_d \\ 0 & P_d & 0 \end{pmatrix}, \quad \mathbf{M}^{(2)} = \begin{pmatrix} P_f & 0 & P_d \\ 0 & P_f & 0 \\ P_d & 0 & P_f \end{pmatrix}. \tag{5.30}$$

where P_f and P_d are respectively the probabilities of forward scattering and deflection to neighboring channels. This means that the admittance $\mathbf{Y}$ is purely real and corresponds to resistive coupling between channels. Conversely, in the limit of strong interactions, there is a purely imaginary admittance $\mathbf{Y} = -i\omega\mathbf{C}$, where ω is frequency and $\mathbf{C}$ is a capacitance matrix coupling the different channels [151, 152].

The plasmon scattering matrix $\mathbf{S}$ is obtained by solving Eq. (5.25) subject to the boundary conditions of Eq. (5.27). Since the junction is six-fold rotationally symmetric, we express the result in terms of phase shifts $e^{2i\delta_m}$ in each angular momentum channel $m = 0, \pm 1, \pm 2, 3$. In terms of these phase shifts

$$S_{jk} = \frac{1}{6}\sum_m e^{2i\delta_m} z_{jk}^m, \quad z_{jk} \equiv e^{i\pi(j-k)/3}. \tag{5.31}$$

By inversion symmetry $\delta_m = \delta_{-m}$, so there are four distinct phase shifts that determine $\mathbf{S}$. By current conservation, the phase shift δ_0 is independent of the boundary conditions imposed by $\mathbf{Y}$.

We consider first the simpler case of scattering for short-range interactions, where $d_g \ll \lambda_p$. The solution away from the junction takes the form $\Phi_i(r_i) = e^{-iqr_i} + S_{ii}e^{iqr_i}$, $\Phi_j(r_j) = S_{ji}e^{iqr_j}$ $(j \neq i)$. Substituting this into Eq. (5.27), we find a formula for the

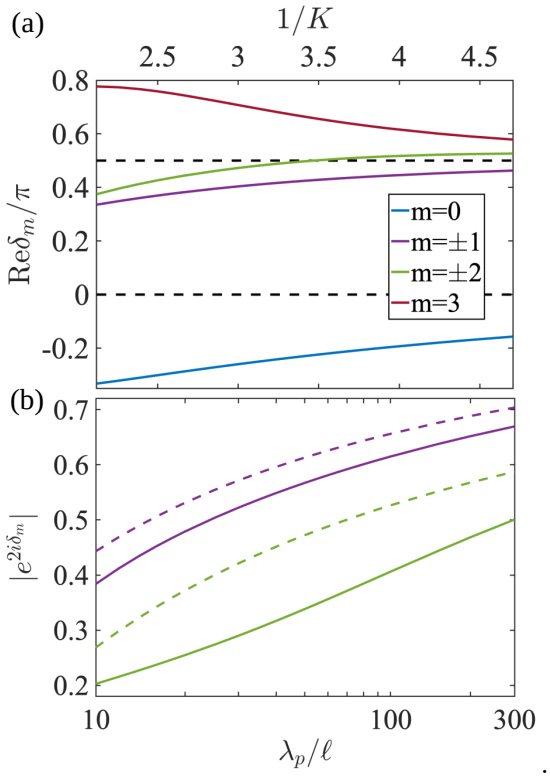

Figure 5.5. Numerical solution for scattering matrix for Coulomb interaction versus plasmon wavelength λ_p. Parameters are $P_f = 0.4$ and $N\alpha = 10$. (a) Real parts of the phase shifts in each angular momentum channel. They asymptotically approach the limiting values shown by the dashed lines. (b) Magnitude of reflection amplitude $|e^{2i\delta_m}|$ for the $m = 1, 2$ channels compared to the prediction of Eq. (5.33) shown by the dashed lines.

scattering matrix:

$$\mathbf{S} = \frac{K\mathbf{1} + \bar{\mathbf{Y}}/2}{K\mathbf{1} - \bar{\mathbf{Y}}/2}, \tag{5.32}$$

or in terms of phase shifts,

$$\begin{aligned} e^{2i\delta_m} &= \frac{K + \bar{Y}_m/2}{K - \bar{Y}_m/2}, \\ \bar{Y}_m &= \sum_j z_{1j}^m \bar{Y}_{1j}. \end{aligned} \tag{5.33}$$

Current conservation requires $\bar{Y}_0 = 0$, hence $\delta_0 = 0$ always. In the absence of interactions, $K = 1$, so $\mathbf{S} = \mathbf{M}$, as expected. For weak interactions, Eq. (5.30) implies $\bar{Y}_3 \to \infty$, and

$$\bar{Y}_1 = \bar{Y}_2^{-1} = -\tfrac{2}{3} P_d^{-1} + 1. \tag{5.34}$$

Therefore, $\delta_3 = \pi/2$ and $\delta_m = \pi/2 + i\mathrm{Im}\delta_m$ for $m = 1, 2$. The imaginary part of the $m = 1, 2$ phase shifts corresponds to dissipation of energy in these channels. For strong interactions, $\bar{Y}_m = -i(\omega L/v)\bar{C}_m$ for $m = 1, 2, 3$, hence there are three independent parameters, $\bar{C}_1$, $\bar{C}_2$, and $\bar{C}_3$, that determine plasmon scattering. For $K \to 0$, we have $\delta_m = \pi/2$ for $m \neq 0$. This implies that $\mathbf{S}$ takes the form

$$S_{ii} = -2/3, \quad S_{ji} = 1/3 \quad (j \neq i), \tag{5.35}$$

which is a universal result independent of $\mathbf{Y}$. It follows from imposing boundary conditions of continuity of the potential Φ across the junction and current conservation:

$$\Phi_j(0) = \Phi_k(0), \quad \sum_j \partial_r \Phi_j(0) = 0. \tag{5.36}$$

This so-called classical limit is approached when either the coupling constant α or the number of modes N become large.

For long-range Coulomb interactions, additional phase shifts are induced. However, as the wavelength increases, the scattering amplitudes tend to those for short-range interactions logarithmically in the small parameter $q\ell$. This behavior is confirmed in Fig. 5.5, where we plot the numerical solution for the δ_m versus the plasmon wavelength λ_p for resistive boundary conditions. In Fig. 5.5(a), we plot the real parts of the phase shifts for each angular momentum channel. At long wavelength $\mathrm{Re}\delta_m$ approaches zero for $m = 0$ and $\pi/2$ for $m \neq 0$ in accordance with Eq. (5.33). Fig. 5.5(b) shows $|e^{2i\delta_m}|$ for the $m = 1, 2$ channels compared to the prediction of Eq. (5.33). Since $|e^{2i\delta_m}| < 1$ for $m = 1, 2$ there is dissipation of energy in these channels. For $m = 0, 3$, we have $|e^{2i\delta_m}| = 1$ due to current conservation, and there is no dissipation.

5.5 Network plasmons

In this section, we analyze plasmons in the mTBG network analogously to the 1D model of Sec. 5.3. For simplicity, we consider a short-range interaction with $U(x) = U_0$ constant, which applies when the interaction is screened by a metallic gate, as discussed in Sec. 5.4. We comment on the modification of our results for long-range Coulomb interactions at the end of this section.

5.5.1 Plasmonic network model

There are three links per unit cell and two propagation directions per link, so in total there are six independent plasmon amplitudes per unit cell. We denote the moiré lattice vectors by $\mathbf{l}_1$, $\mathbf{l}_2$, and $\mathbf{l}_3 = -(\mathbf{l}_1 + \mathbf{l}_2)$ (see Fig. 5.1), and choose the jth link in a unit cell to be along $\mathbf{l}_j$ ($j = 1, 2, 3$). In a given unit cell, let $\phi_{j\pm}$ be the amplitude of the plasmon wave along the jth link, propagating in the forward (+) or backward (−) direction. Traversing the link at frequency ω it accumulates a phase $e^{i\omega L/v_p}$. At a given Bloch momentum $\mathbf{q}$, amplitudes on links directly opposite each other are related by a Bloch phase. The six incoming and outgoing amplitudes at a node may be represented by

six-element vectors $\Phi_{\rm in}(\mathbf{q})$ and $\Phi_{\rm out}(\mathbf{q})$ respectively:

$$\begin{aligned}\Phi_{\rm in}(\mathbf{q}) &= e^{i\omega_{\mathbf{q}}L/v_p}\,\big(\phi_{1-}, e^{-i\mathbf{q}\cdot\mathbf{l}_2}\phi_{2+}, \phi_{3-},\\ &\qquad e^{-i\mathbf{q}\cdot\mathbf{l}_1}\phi_{1+}, \phi_{2-}, e^{-i\mathbf{q}\cdot\mathbf{l}_3}\phi_{3+}\big),\\ \Phi_{\rm out}(\mathbf{q}) &= \big(\phi_{1+}, e^{-i\mathbf{q}\cdot\mathbf{l}_2}\phi_{2-}, \phi_{3+},\\ &\qquad e^{-i\mathbf{q}\cdot\mathbf{l}_1}\phi_{1-}, \phi_{2+}, e^{-i\mathbf{q}\cdot\mathbf{l}_3}\phi_{3-}\big).\end{aligned} \tag{5.37}$$

The incoming and outgoing amplitudes are related by the scattering matrix, $\Phi_{\rm out}(\mathbf{q}) = S\,\Phi_{\rm in}(\mathbf{q})$. Therefore, the plasmon modes are obtained by solving the following eigenproblem:

$$\begin{aligned}T(\mathbf{q})\bar{\Phi}_{\mathbf{q}} &= e^{-i\omega_{\mathbf{q}}L/v_p}\bar{\Phi}_{\mathbf{q}}, \quad T(\mathbf{q}) = W\Lambda_{\mathbf{q}}^{-1}S\Lambda_{\mathbf{q}},\\ \Lambda_{\mathbf{q}} &= \mathrm{diag}\,\big(1, e^{-i\mathbf{q}\cdot\mathbf{l}_2}, 1, e^{-i\mathbf{q}\cdot\mathbf{l}_1}, 1, e^{-i\mathbf{q}\cdot\mathbf{l}_3}\big), \quad W = \begin{pmatrix} 0 & \mathbf{1}_3 \\ \mathbf{1}_3 & 0 \end{pmatrix},\\ \bar{\Phi}_{\mathbf{q}} &= \big(\phi_{1-}, \phi_{2+}, \phi_{3-}, \phi_{1+}, \phi_{2-}, \phi_{3+}\big).\end{aligned} \tag{5.38}$$

The inverse dielectric function is

$$\begin{aligned}\epsilon^{-1}_{\mathrm{PNM},\mathbf{G}\mathbf{G}'}(\mathbf{q},\omega) &= \sum_n \epsilon^{-1}_{\rm 1D}(\omega_{n,\mathbf{q}}/v_p, \omega + i\gamma)\tilde{\Phi}_{n,\mathbf{q},\mathbf{G}}\tilde{\Phi}^*_{n,\mathbf{q},\mathbf{G}'},\\ \tilde{\Phi}_{n,\mathbf{q},\mathbf{G}} &= \sum_{j=1}^{3}\int_0^L dx\, e^{-i(\mathbf{q}+\mathbf{G})\cdot\hat{\mathbf{l}}_j x}\Phi_{j,n,\mathbf{q}}(x).\\ \Phi_{j,n,\mathbf{q}}(x) &= \phi_{j+,n,\mathbf{q}}e^{i\omega_{n,\mathbf{q}}x/v_p} + \phi_{j-,n,\mathbf{q}}e^{i\omega_{n,\mathbf{q}}(L-x)/v_p},\end{aligned} \tag{5.39}$$

with the eigenvector $\bar{\Phi}_{\mathbf{q}}$ normalized such that $\sum_{j=1}^{3}\int_0^a dx|\Phi_{j,n,\mathbf{q}}(x)|^2 = 1$. The spectral function is $S_{\rm PNM}(\mathbf{q},\omega) = -\mathrm{Im}\sum_{\mathbf{G}}\epsilon^{-1}_{\mathrm{PNM},\mathbf{G}\mathbf{G}}(\mathbf{q},\omega)$.

5.5.2 Random phase approximation

The procedure of Sec. 5.3.2 may be straightforwardly generalized to calculate the RPA spectrum of the mTBG network. We begin by calculating the single-particle spectrum

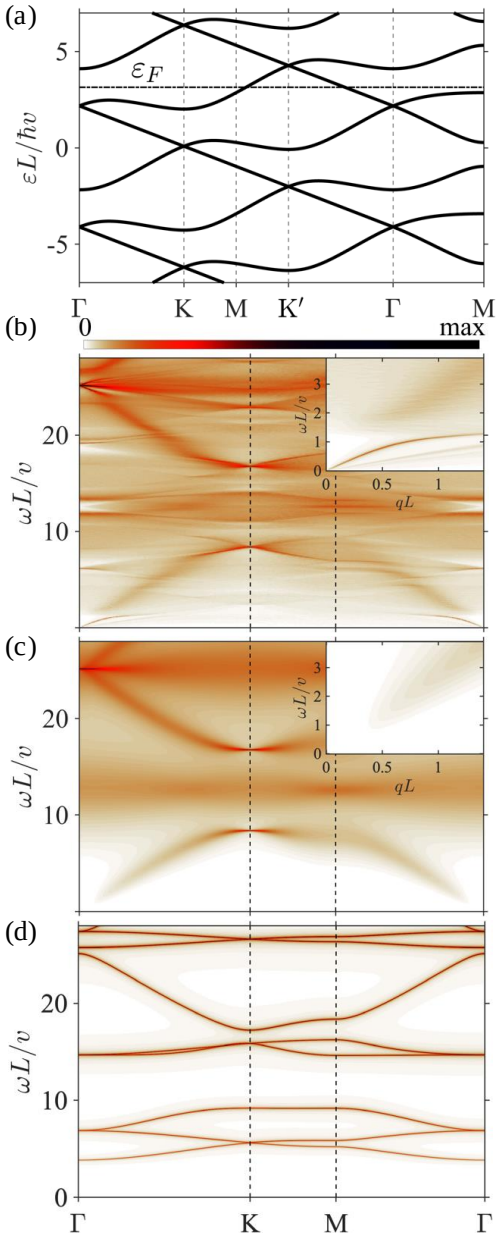

Figure 5.6. (a) The single-particle band structure for $P_f = 0.4$. The dashed-dotted line denotes the Fermi energy used for the RPA calculation below. (b) Corresponding RPA spectrum. The Luttinger parameter is $K = 0.25$. (c) Resistive PNM spectrum for the same parameters. The insets in (b) and (c) show a zoom-in on the low-frequency part of the spectum. (d) Capacitive PNM spectrum with $\bar{C}_1 = -0.125$, $\bar{C}_2 = -0.25$, $\bar{C}_3 = -0.5$.

as described in Appendix D. The RPA polarizability is given by a formula analogous to Eq. (5.11):

$$\begin{aligned} P_{\mathbf{G}\mathbf{G}'}(\mathbf{q},\omega) =& \frac{1}{\hbar}\sum_{\nu=\pm}\sum_{n,m}\int \frac{d^2k}{(2\pi)^2}\rho^{n,m}_{\mathbf{k},\mathbf{q},\mathbf{G}}\left(\rho^{n,m}_{\mathbf{k},\mathbf{q},\mathbf{G}'}\right)^* \\ & \times \nu\frac{n_F(\varepsilon_{n,\mathbf{k}}-\varepsilon_F)-n_F(\varepsilon_{m,\mathbf{k}+\mathbf{q}}-\varepsilon_F)}{\omega-\nu(\varepsilon_{m,\mathbf{k}+\mathbf{q}}-\varepsilon_{n,\mathbf{k}})/\hbar+i\gamma}, \\ \rho^{n,m}_{\mathbf{k},\mathbf{q},\mathbf{G}} =& \sum_{j=1}^{3}\int_0^L dx\, e^{-i(\mathbf{q}+\mathbf{G})\cdot\hat{\mathbf{l}}_j x}\Psi^*_{j,n,\mathbf{k}}(x)\Psi_{j,m,\mathbf{k}+\mathbf{q}}(x), \\ \Psi_{j,n,\mathbf{k}}(x) =& \frac{1}{\sqrt{L}}\psi_{j,n,\mathbf{k}}e^{i\varepsilon_{n,\mathbf{k}}x/\hbar v}, \end{aligned} \tag{5.40}$$

where $\mathbf{G}$ and $\mathbf{G}'$ are moiré reciprocal lattice vectors, $\varepsilon_{n,\mathbf{k}}$ is the single-particle energy of momentum $\mathbf{k}$ in the nth band, $\psi_{j,n,\mathbf{k}}$ is the corresponding wavefunction amplitude on the jth link, the integration is over the moiré Brillouin zone, and the summation over ν accounts for states in both K and K′ valleys. The wavefunction amplitudes are normalized such that $\sum_{j=1}^{3}|\psi_{j,n,\mathbf{k}}|^2 = 1$. The dielectric function is

$$\epsilon_{\mathrm{RPA},\mathbf{G}\mathbf{G}'}(\mathbf{q},\omega) = \delta_{\mathbf{G}\mathbf{G}'} - \tilde{U}(\mathbf{q}+\mathbf{G})P_{\mathbf{G}\mathbf{G}'}(\mathbf{q},\omega), \tag{5.41}$$

with $\tilde{U}(\mathbf{q})$ the 2D Fourier transform of the interaction potential. At long wavelength, the plasmon dispersion is linear in q and determined by Eqs. (5.3) and (5.4). We define the spectral function $S_{\mathrm{RPA}}(\mathbf{q},\omega) = -\mathrm{Im}\sum_{\mathbf{G}}\epsilon^{-1}_{\mathrm{RPA},\mathbf{G}\mathbf{G}}(\mathbf{q},\omega)$.

5.5.3 Results

We plot an example single particle spectrum in Fig. 5.6(a) The corresponding RPA spectral function is plotted in Fig. 5.6(b) for a representative choice of parameters. At low frequency there are three linearly dispersing gapless modes, as predicted by Eq. (5.4). At higher frequencies the plasmon modes lie in the particle hole continuum and have a finite lifetime. However, there are dissipationless modes at high-symmetry points Γ, K, and K′,

which, as in Sec. 5.3, are explained by nesting of the single-particle bands.

We plot PNM spectral functions in Fig. 5.6(c,d) for resistive and capacitive boundary conditions, respectively. The spectrum is quasi-periodic in frequency with six bands per period $2\pi v_p/L$, although we only plot one full period. In the resistive case, the low-frequency spectrum is diffusive, and there are two modes with dispersions

$$\omega_{1,\mathbf{q}} = -i\frac{Lv}{4K^2}(-\bar{Y}_1)q^2, \quad \omega_{2,\mathbf{q}} = -i\frac{Lv}{4}(-\bar{Y}_1)q^2, \tag{5.42}$$

with $\bar{Y}_1$ given by Eq. (5.34). At higher frequencies, there are broadened, linearly dispersing modes, as well as non-dispersive modes when $\omega L/v_p$ is an integer multiple of π. As in the RPA spectrum, the modes become sharp at high-symmetry points Γ, K, and K$'$. This is because there is no dissipation in the $m = 0$ and $m = 3$ scattering channels [Sec. 5.4]. In the capacitive case, the plasmons are dissipationless at all frequencies, and the spectrum has a gap ω_0 determined by the solution of

$$\omega_0 = \frac{K}{2\bar{C}_{\max}} \cot\left(\frac{a}{2v_p}\omega_0\right), \tag{5.43}$$

where $C_{\max} = \max(|\bar{C}_1|, |\bar{C}_2|, |\bar{C}_3|)$.

It is interesting to consider the classical limit of $\mathbf{S}$ given by Eq. (5.35), for which Eq. (5.38) can be solved analytically. The resulting band structure is given by

$$\begin{aligned} &\omega^1_{n,\mathbf{q}} L/v_p = 2n\pi, \quad \omega^2_{n,\mathbf{q}} L/v_p = (2n+1)\pi, \\ &\omega^{\pm}_{n,\mathbf{q}} L/v_p = 2n\pi \pm \arccos\left[\frac{1}{3}\sum_{j=1}^{3}\cos(\mathbf{q}\cdot\mathbf{l}_j)\right], \end{aligned} \tag{5.44}$$

where $n \in \mathbb{Z}$. There is a linearly dispersive gapless mode at the Γ point as well as twofold degenerate flat bands $\omega^1_{n,\mathbf{q}}$ and $\omega^2_{n,\mathbf{q}}$ that correspond to eigenstates localized on closed loops in the network.

For long range interactions, the main difference is in the low-frequency part of the spectrum, where the plasmons will have a $\sqrt{q}$ dispersion. In the coherent regime, the Drude weight is given by the RPA formula Eq. (5.2); in the incoherent regime, it takes the classical value $D_{\max}$ defined in Eq. (5.5). At higher frequencies, the plasmon modes are well-approximated by solving Eq. (5.38) with a wavelength dependent scattering matrix (Fig. 5.5).

5.6 Near-field imaging

Plasmons can be observed in real-space using scattering-type scanning near-field optical microscopy (s-SNOM) [156]. In this technique, an atomic force microscope (AFM) tip is positioned close to the sample and illuminated by an infrared laser. The light scattered by the tip launches surface plasmons, which in turn modify its total radiating dipole moment, and this is measured in the far-field. Note that plasmons can also be launched by a fixed object such as an impurity and detected with the tip. The resulting near-field contrast provides a real-space picture of plasmon interference patterns in the sample. In general, the magnitude of this near-field contrast has a complex dependence on the optical conductivity of the sample and the probe-sample coupling [156, 157]. Here we use a simplified model that gives the near-field signal as a convolution of the inverse dielectric function with appropriate form factors. As shown in Appendix F, the signal for a plasmon launched at position $\mathbf{r}'$ and detected at position $\mathbf{r}$ is proportional to

$$\begin{aligned} G(\mathbf{r},\mathbf{r}';\omega) = \sum_{\mathbf{G},\mathbf{G}'} \int \frac{d^2k}{(2\pi)^2} e^{i(\mathbf{q}+\mathbf{G})\cdot\mathbf{r}} e^{-i(\mathbf{q}+\mathbf{G}')\cdot\mathbf{r}'} \\ \times F_d(\mathbf{q}+\mathbf{G}) \epsilon^{-1}_{\mathbf{G}\mathbf{G}'}(\mathbf{q},\omega) F_l(\mathbf{q}+\mathbf{G}'). \end{aligned} \tag{5.45}$$

Here, $F_d(\mathbf{q}) = qe^{-qz_{\text{tip}}}$, where z_{tip} is the tip-sample distance. For the form factor $F_l(\mathbf{q})$, we take $F_l(\mathbf{q}) = e^{-qz_{\text{tip}}}$ for tip-launched plasmons and $F_l(\mathbf{q}) = 1$ for plasmons launched by an impurity (see Appendix F).

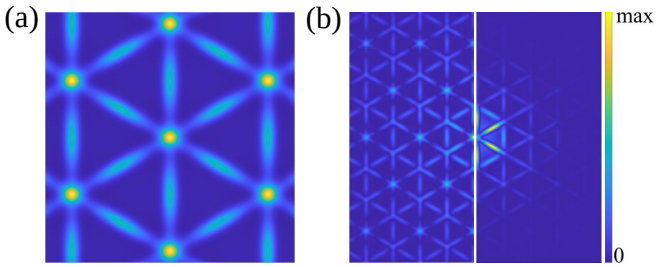

Figure 5.7. (a) Simulated amplitude of near-field signal for frequency $\omega = 19v/a$. (b) Amplitude of near-field signal for a point source at an AA vertex for frequencies $\omega = (4\pi/3)v/L$ (left) and $\omega = 15.5v/L$ (right). Parameters are $K = 0.25$ and $P_f = 0.4$, corresponding to Fig. 5.6(c). The tip-sample distance $z_{\rm tip} = 0.1L$.

For an isolated node, the scattering amplitudes can in principle be determined directly from the near-field signal. Suppose a wave of momentum q is launched at a distance from the node r along the ith link and detected at distance r' along the jth link. It is clear that the resulting signal is proportional to

$$S_{ij} e^{iq(r+r')}. \tag{5.46}$$

The near-field signal for the network is determined, conceptually, by summing over all possible scattering processes. We calculate it numerically from the network dielectric function as discussed above. Simulated near-field images are shown in Fig. 5.7, with $\epsilon^{-1}_{\mathbf{G}\mathbf{G}'}(\mathbf{q}, \omega)$ calculated using the PNM with parameters corresponding to Fig. 5.6(c). In Fig. 5.7(a), the probe acts as both a launcher and detector of the near-field signal. In Fig. 5.7(b), we show the near-field signal from a fixed launcher, e.g., an impurity. The left image is for frequency $\omega = 4\pi/3v/(Ka)$, in resonance with the dissipationless mode at the K point. Therefore, a propagating wave is launched from the tip. The right image is for frequency $\omega = 15.5v/a$, and the response is exponentially localized.

5.7 Discussion and outlook

In this work, we have formulated a theoretical model for plasmons in the network of channel states formed in minimally twisted gapped bilayer graphene. We studied two different regimes depending on the single-particle phase coherence length L_φ. In the phase-coherent regime, $L_\varphi \gg L$, we employed the RPA to calculate the plasmonic spectrum of the network. In the phase-incoherent regime, $L_\varphi \ll L$, plasmon modes are described with a plasmonic network scattering model (PNM), which is similar to scattering models used to describe the single-particle band structure of the mTBG network [141, 142]. However, two key differences of the PNM compared to these single-particle models are that plasmons can scatter in any direction, so plasmon scattering is governed by a full 6×6 scattering matrix, and that this scattering dissipates energy. This also distinguishes our model from a related work on plasmons in the mTBG network, where plasmons were restricted to scatter only in certain directions, as in the single-particle models [148].

In order to experimentally realize domain-wall plasmons, it is necessary that the chemical potential resides in the bandgap, and that the frequency is low enough to avoid Landau damping associated with optical transitions to the bands in AB and BA regions. The former condition may be satisfied by using a top and back gate to independently control the displacement field and Fermi level, and a clean substrate to reduce disorder and unintentional doping. Performing SNOM on top-gated systems may be challenging, but methods based on a transmission line could be a viable alternative to image plasmons [158, 159]. To satisfy the latter condition, $\hbar\omega$ must be smaller than $\Delta_{\mathrm{TBG}}/2$, with Δ_{TBG} the bandgap. The characteristic frequency scale of plasmons is $\omega_0 = 2\pi v/(KL)$. With v equal to the graphene Fermi velocity of 10^8 cm/s, $L = 200$ nm (corresponding to a twist angle of $0.07°$), and $K = 0.5$, we have $\hbar\omega_0 \approx 40$ meV. In contrast, bandgaps up to $\Delta_{\mathrm{TBG}} \approx 200$ meV can be achieved by applying a strong out-of-plane electric field to the sample [124]. Therefore, 1D plasmons with wavelengths $\lambda_p < L$ can be realized.

Potential future directions include studying plasmons in this system under an out-of-plane magnetic field, where Ahronov-Bohm oscillations were observed in electron transport experiments [134, 142], and exploring the crossover between the phase-coherent and incoherent regimes. Considering the effects of strain, which can induce quasi-1D channels in moiré systems [160], would also be intriguing. Additionally, it has been shown that narrow band systems, such as TBG, exhibit instrinsically undamped plasmons above the particle-hole continuum [161], which may have implications for our model.

This chapter, in full, is currently being prepared for submission for publication of the material "Plasmon modes of topological state networks in twisted bilayer graphene" by B. Vermilyea and M.M. Fogler. The dissertation author was the primary investigator and author of the material.

Chapter 6

Conclusion

In this dissertation, I have investigated the many-body physics of excitons and plasmons in low-dimensional systems. In Chapter 2 we studied interactions between polaritons formed by hybridization of excitons in a two-dimensional semiconductor with surface optical phonons or plasmons. These quasiparticles have a high effective mass and can bind into bipolaritons near a Feshbach-like scattering resonance. We analyzed the phase diagram of a many-body condensate of heavy polaritons and bipolaritons and calculated their absorption and luminescence spectra, which can be measured experimentally. Chapter 3 considered another type of polariton that results from the hybrization of magnetoexcitons in graphene with hyperbolic phonon modes in hexagonal boron nitride. We calculated the shift in the magnetoexciton energy due to many-body effects, and found excellent agreement with the experimental data. Additionally, we formulated a quantum theory of LPPs in a graphene/hBN heterostructure and derived an analytical expression for the polaritonic gap. In Chapter 4, we developed a many-body theory of excitonic Bose-polarons formed by spatially direct excitons immersed in a degenerate Bose gas of spatially indirect excitons, and found good agreement with experimental data. Lastly, in Chapter 5, we studied surface plasmons in minimally-twisted gapped bilayer graphene that develops a triangular network of partial dislocations (or AB-BA domain walls) hosting one-dimensional electronic states. We formulated a theoretical model describing the plasmonic spectrum of the network in

different regimes of temperature and electron-electron interaction strength, and discussed optical nano-imaging experiments that can verify our predictions.

Going forward, it would be interesting to extend our work on excitonic Bose-polarons and develop a more sophisticated theory that describes the crossover from Bose to Fermi polarons. To this end, methods known from the Fermi-edge singularity problem may be applicable [162, 163]. Another research problem related to exciton-polarons is motivated by recent experiments that detect correlated electron phases in 2D materials, such as Wigner crystal [164] or fractional quantum Hall [165] phases, using exciton excited states in a TMD monolayer as a sensor. It would be intriguing to develop a theory of how the energy and oscillator strength of the exciton states change due to their interaction with the sample in these experiments. Regarding plasmons, our study of plasmon scattering in twisted bilayer graphene motivates the question of how to describe the physics of a junction of Luttinger liquid wires in different regimes of interaction strength [152]. Finally, another research direction is quantum plasmonics, which enables confinement of light at scales far below that of conventional quantum optics. Previous work has shown that graphene can be a source of entangled plasmons with pair generation rates greatly exceeding those of conventional photonic sources [166]. An open question is how plasmons could be used to extract entanglement from a many-body system [167].

Appendix A

Heavy exciton-polaritons

A.1 Scattering matrix calculation

The scattering matrix satisfies the Bethe-Salpeter equation, which with the notation $k = (\mathbf{k}, i\omega_n)$ takes the form [22]

$$\begin{aligned}\mathcal{T}(k,k';k+q,k'-q) =& W(k,k',q) + \sum_{q'} W(k,k',q')G_x(k+q')G_x(k'-q') \\ & \times \mathcal{T}(k+q',k'-q';k+q;k'-q). \end{aligned} \tag{A.1}$$

Here $W(k,k',q)$ is the interaction vertex and $G_x(k)$ is the exciton Green's function. If $W(k,k',q) = W_0$ is frequency and momentum independent, then $\mathcal{T}$ depends only on the total incoming momentum and energy $(\mathbf{K},\omega)$ and Eq. (A.1) is solved immediately:

$$\mathcal{T}(\mathbf{K},\omega) = \left[W_0^{-1} - \Pi(\mathbf{K},\omega)\right]^{-1}, \tag{A.2}$$

with the two-exciton propagator (at zero temperature)

$$\Pi(\mathbf{K},\omega) = \sum_{\mathbf{q}} \int \frac{d\omega'}{2\pi i} G_x(\mathbf{K}-\mathbf{q},\omega-\omega')G_x(\mathbf{q},\omega'). \tag{A.3}$$

Consider first the case of free excitons, where the Green's function is $G_x^0(,\omega) = (\omega - \omega_{x,\mathbf{k}})^{-1}$, and the propagator is

$$\Pi_0(\mathbf{K},\omega) = \sum_{\mathbf{q}} \int \frac{d\omega'}{2\pi i} G_x^0(\mathbf{K}-\mathbf{q},\omega-\omega') G_x^0(\mathbf{q},\omega') = \sum_{\mathbf{q}} \frac{1}{\omega - \omega_{x,\mathbf{K}-\mathbf{q}} - \omega_{x,\mathbf{q}}}. \tag{A.4}$$

Since the sum diverges logarithmically at large $\mathbf{q}$, we must impose a momentum cutoff Λ, and we have $\Pi_0(\mathbf{K}=0,\omega) = -\frac{m_x}{4\pi}\ln(-E_\Lambda/\omega)$, with $E_\Lambda = \Lambda^2/2m_x$. We eliminate W_0 by requiring that the biexciton binding energy E_{xx} is the pole of the of the zero-momentum scattering matrix, so $W_0^{-1} = -\frac{m_x}{4\pi}\ln(E_\Lambda/E_{xx})$, and the renormalized free exciton scattering matrix takes the form

$$\mathcal{T}_0(\mathbf{K}=0,\omega) = \frac{4\pi/m_x}{\ln\left(-E_{xx}/\omega\right)}, \tag{A.5}$$

which is the universal result for low-energy scattering in 2D [168]. We now consider the case of exciton-polaritons, where the exciton Green's function is

$$G_x(\mathbf{k},\omega) = \sum_{s=\pm} \frac{U_{s,\mathbf{k}}^2}{\omega - \omega_{s,\mathbf{k}}}. \tag{A.6}$$

The polariton energies $\omega_{\pm,\mathbf{k}}$ and Hopfield coefficients $U_{\pm,\mathbf{k}}$ are given respectively in Eqs. (2.2) and (2.5) of the main text. The two-exciton propagator is

$$\Pi(\mathbf{K},\omega) = \sum_{\mathbf{q}} \sum_{s,s'=\pm} \frac{U_{s,\mathbf{K}-\mathbf{q}}^2 U_{s',\mathbf{q}}^2}{\omega - \omega_{s,\mathbf{K}-\mathbf{q}} - \omega_{s',\mathbf{q}}}. \tag{A.7}$$

For photon exciton-polaritons, the cavity mode dispersion takes the form $\omega_{p,\mathbf{k}} =$

$\delta + k^2/2m_p$, with $m_p \ll m_x$. We expand $\Pi(\mathbf{K}=0,\omega)$ in $m_p/m_x \ll 1$ and find

$$\mathcal{T}(\mathbf{K}=0,\omega) = \frac{4\pi}{m_x}\Bigg\{ \ln(-E_{xx}/\omega) + \frac{m_p}{m_x}\frac{\Omega^2}{\omega^2}\Bigg[-1 + \ln[-(m_x/2m_p)\omega/E_{xx}] \\ - \frac{1}{\omega^2+\Omega^2}\big(\omega^2 \ln[(\omega_+ + \omega_- - \omega)/E_{xx}] + \Omega^2\{-\ln[-2\omega/E_{xx}] \\ + \ln[(2\omega_+ - \omega)/E_{xx}] + \ln[(2\omega_- - \omega)/E_{xx})]\}\Bigg] + \ldots \Bigg\}^{-1}. \quad \text{(A.8)}$$

Here $\omega_\pm = \frac{1}{2}\left(\delta \pm \sqrt{\delta^2+\Omega^2}\right)$ are the polariton energies at zero momentum. This shows that $\mathcal{T}(\mathbf{K}=0,\omega)$ has a pole at the biexciton binding energy which is slightly shifted from E_{xx} and acquires a small imaginary part in the two-polariton continuum. In addition, there are bipolariton poles at energies below $\omega_s + \omega_{s'}$, but it is apparent from Eq. (A.8) that the bipolariton binding energy and spectral weight are exponentially small in the large mass ratio m_x/m_p, in agreement with Eq. (2.7) of the main text.

For heavy polaritons we take $\omega_{c,\boldsymbol{k}} = \delta$ constant. Then the integral in Eq. (A.7) may be evaluated analytically at $\mathbf{K}=0$ and we find

$$\mathcal{T}(\mathbf{K}=0,\omega) = -(4\pi/m_x)\left[(2\delta-\omega)^2+\Omega^2\right]\Big\{\Omega^2 \ln[2(\omega_+ + \omega_- - \omega)/E_{xx}] + (2\delta-\omega)^2 \\ \times(-\ln[(2\delta-\omega)/E_{xx}] + \ln[(2\omega_+ - \omega)/E_{xx}] + \ln[(2\omega_- - \omega)/E_{xx}])\Big\}^{-1}. \quad \text{(A.9)}$$

The bipolariton energies $\omega_{ss',\mathbf{K}}$ are poles of $\mathcal{T}(\mathbf{K},\omega)$. The scattering matrix between two polaritons s and s' with incoming momenta $\mathbf{K/2}+\mathbf{k}$ and $\mathbf{K/2}-\mathbf{k}$ and outgoing momenta $\mathbf{K/2}+\mathbf{k}'$ and $\mathbf{K/2}-\mathbf{k}'$ is given by

$$\mathcal{T}_{ss'}(\mathbf{k},\mathbf{k}',\mathbf{K},\omega) = U_{s,\mathbf{K/2+k}} U_{s',\mathbf{K/2-k}} U_{s,\mathbf{K/2+k'}} U_{s',\mathbf{K/2-k'}} \mathcal{T}(\mathbf{K},\omega). \quad \text{(A.10)}$$

The polariton Green's functions are $G_s(\mathbf{k},\omega) = (\omega - \omega_{s,\mathbf{k}})^{-1}$ and we define $\tilde{G}_{ss'}(\mathbf{k},\mathbf{K},\omega) =$

$\int \frac{d\omega'}{2\pi i} G_s(\omega - \omega', \mathbf{K/2} - \mathbf{k}) G_{s'}(\omega', \mathbf{K/2} + \mathbf{k})$, or

$$\tilde{G}_{ss'}(\mathbf{k}, \mathbf{K}, \omega) = \frac{1}{\omega - \omega_{s,\mathbf{K/2-k}} - \omega_{s',\mathbf{K/2+k}}}. \tag{A.11}$$

In the spectral vicinity of the bipolariton resonance, we have [26]

$$\tilde{G}_{ss'}(\mathbf{k}, \mathbf{K}, \omega) \mathcal{T}_{ss'}(\mathbf{k}, \mathbf{k}', \mathbf{K}, \omega) \tilde{G}_{ss'}(\mathbf{k}', \mathbf{K}, \omega) \simeq \frac{\psi_{ss'}(\mathbf{k}, \mathbf{K}) \psi_{ss'}(\mathbf{k}', \mathbf{K})}{\omega - \omega_{ss',\mathbf{K}}}, \tag{A.12}$$

which defines the bipolariton wavefunction $\psi_{ss'}(\mathbf{k}, \mathbf{K})$. In our approximation

$$\psi_{ss'}(\mathbf{k}, \mathbf{K}) = \mathcal{N}_{\mathbf{K}} \frac{U_{s,\mathbf{K/2-k}} U_{s',\mathbf{K/2+k}}}{\omega_{ss',\mathbf{K}} - \omega_{s,\mathbf{K/2-k}} - \omega_{s',\mathbf{K/2+k}}}, \tag{A.13}$$

with $\mathcal{N}_{\mathbf{K}}$ a normalization factor such that $\sum_{\mathbf{k}} |\psi_{ss'}(\mathbf{k}, \mathbf{K})|^2 = 1$. The bipolariton wavefunction is used to compute the optical spectra, see Appendix A.2.

A.2 Calculation of absorption and luminescence spectra

Two processes contribute to the absorption and luminescence spectra: direct coupling of polaritons to photons and coupling of a bipolariton to a photon and polariton [103, 169]. The relevant diagrams for calculating photon self-energy are shown in Fig. A.1. The filled circle denotes the photon-polariton coupling vertex. In terms of the photon-exciton coupling μ_x, it is given by

$$\mu_{1,\mathbf{q}} = U_{-,\mathbf{q}} \mu_x, \tag{A.14}$$

where $U_{-,\mathbf{q}}$ is the Hopfield coefficient. The open circle denotes the photon-polariton-bipolariton coupling vertex, given by

$$\mu_{12,\mathbf{k},\mathbf{q}} = U_{-,\mathbf{k}} U^2_{-,\mathbf{q}+\mathbf{k}} \psi((\mathbf{q}-\mathbf{k})/2, \mathbf{q}+\mathbf{k}) \mu_x, \tag{A.15}$$

with ψ the bipolariton wavefunction defined by Eq. (A.12).

Normal state

In the normal state, only the first two diagrams of Fig. A.1 contribute. The Matsubara Green's functions are

$$G_i(\mathbf{k}, i\omega_n) = \frac{1}{i\omega_n - \tilde{\omega}_{i,\mathbf{k}}}, \tag{A.16}$$

where $i = 1, 2$ for the polariton and bipolariton respectively. Here $\tilde{\omega}_{1,\mathbf{k}}$ and $\tilde{\omega}_{2,\mathbf{k}}$ are the polariton and bipolariton energies shifted by interaction (see Sec. 2.2). The photon self-energy is

$$\Pi(\mathbf{q}, i\omega_n) = |\mu_{1,\mathbf{q}}|^2 G_1(\mathbf{q}, i\omega_n) - \sum_{\mathbf{k}} \sum_{i\omega'_n} |\mu_{12,\mathbf{k},\mathbf{q}}|^2 G_1(\mathbf{k}, i\omega'_n) G_2(\mathbf{q}+\mathbf{k}, i\omega_n + i\omega'_n). \tag{A.17}$$

Evaluating the sum over $i\omega'_n$, we obtain the absorption spectrum:

$$\begin{aligned} A(\mathbf{q}, \omega) =& -2\mathrm{Im}\Pi(\mathbf{q}, \omega - \mu) = |\mu_{1,\mathbf{q}}|^2 2\pi\delta(\omega - \mu - \tilde{\omega}_{1,\mathbf{q}}) \\ &+ \sum_{\mathbf{k}} |\mu_{12,\mathbf{k},\mathbf{q}}|^2 [n_B(\tilde{\omega}_{1,\mathbf{k}}) - n_B(\tilde{\omega}_{2,\mathbf{q}+\mathbf{k}})] 2\pi\delta(\omega - \mu + \tilde{\omega}_{1,\mathbf{k}} - \tilde{\omega}_{2,\mathbf{q}+\mathbf{k}}). \end{aligned} \tag{A.18}$$

with

$$n_B(\omega) = \left(e^{\beta\omega} - 1\right)^{-1} \tag{A.19}$$

the Bose distribution function, β being the inverse temperature. The luminescence spectrum is [103]

$$\begin{aligned} I(\mathbf{q},\omega) =& n_B(\omega-\mu)A(\mathbf{q},\omega) \\ =& |\mu_{1,\mathbf{q}}|^2 n_B(\tilde{\omega}_{1,\mathbf{q}})2\pi\delta(\omega-\mu-\tilde{\omega}_{1,\mathbf{q}}) \\ &+ \sum_{\mathbf{k}} |\mu_{12,\mathbf{k},\mathbf{q}}|^2[1+n_B(\tilde{\omega}_{1,\mathbf{k}})]n_B(\tilde{\omega}_{2,\mathbf{q}+\mathbf{k}})2\pi\delta(\omega-\mu+\tilde{\omega}_{1,\mathbf{k}}-\tilde{\omega}_{2,\mathbf{q}+\mathbf{k}}). \end{aligned} \quad \text{(A.20)}$$

For $\mathbf{q}=0$ and far from the Feshbach resonance, this spectrum consists of a sharp peak at $\omega=\mu+g_{11}n_1+g_{12}n_2$ and a continuum below the energy $\omega=\mu-E_{--}+(g_{11}-g_{12})n_1+(g_{12}-g_{22})n_2$, similar to Eq. (2.15). In principle, this spectrum is qualitatively different from what is shown in Fig. 2.5(b), and so it can be used to identify the condensation transition.

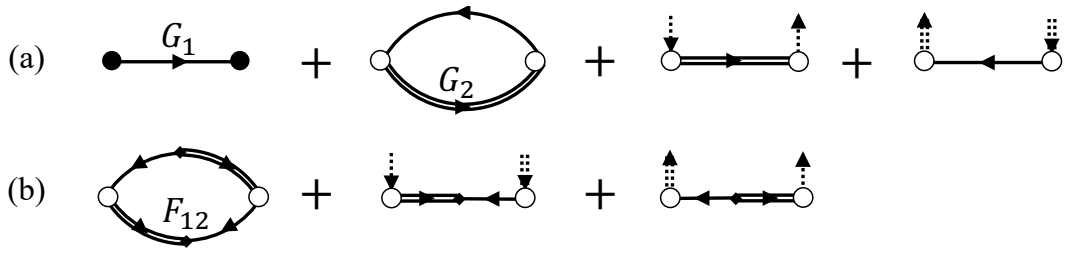

Figure A.1. Diagrams for calculating photon self-energy including (a) normal and (b) anomalous contributions. In the normal state only the first two diagrams in (a) are non-vanishing. Single and double lines denote exciton and biexciton Green's functions, respectively. The filled circle denotes the photon-polariton coupling vertex, and the open circle is the photon-polariton-bipolariton coupling vertex. Dotted lines indicate particles going into or out of the condensate.

Condensed state

In the condensed state, there are two modes: a gapless mode $E_{0,\mathbf{k}}$ and gapped mode $E_{1,\mathbf{k}}$. The Matsubara Green's functions may be written

$$G_i(\mathbf{k}, i\omega_n) = \sum_{\sigma=0,1} \sum_{s=\pm} \frac{s\left(u_{i,\mathbf{k}}^{\sigma,s}\right)^2}{i\omega_n - sE_{\mathbf{k}}^{\sigma}}. \tag{A.21}$$

Here the $u_{i,\mathbf{k}}^{\sigma,s}$ are Bogolubov coefficients that satisfy $\sum_{\sigma,s} s\left(u_{i,\mathbf{k}}^{\sigma,s}\right)^2 = 1$. We also need the anomalous Green's functions

$$F_{ij}(\mathbf{k}, i\omega_n) = -\sum_{\sigma=0,1} \sum_{s=\pm} \frac{s u_{i,\mathbf{k}}^{\sigma,s} u_{j,\mathbf{k}}^{\sigma,-s}}{i\omega_n - sE_{\mathbf{k}}^{\sigma}}. \tag{A.22}$$

Expressions for the energies and Bogolubov coefficients in terms of the parameters in the effective Hamiltonian of Eq. (2.8) are given in Ref. 37. The photon self-energy is

$$\begin{aligned}\Pi(\mathbf{q}, i\omega_n) =& |\mu_{1,\mathbf{q}}|^2 G_1(\mathbf{q}, i\omega_n) - \sum_{\mathbf{k}} \sum_{i\omega_n'} |\mu_{12,\mathbf{k},\mathbf{q}}|^2 G_1(\mathbf{k}, i\omega_n') G_2(\mathbf{q}+\mathbf{k}, i\omega_n + i\omega_n') \\ &- \sum_{\mathbf{k}} \sum_{i\omega_n'} |\mu_{12,\mathbf{k},\mathbf{q}}|^2 F_{12}(\mathbf{k}, i\omega_n') F_{21}^*(\mathbf{q}+\mathbf{k}, i\omega_n + i\omega_n') \\ &+ |\mu_{12,\mathbf{0},\mathbf{q}}|^2 \left[n_1 G_2(\mathbf{q}, i\omega_n) + n_2 G_1(\mathbf{q}, -i\omega_n) - 2\sqrt{n_1 n_2} F_{12}(\mathbf{q}, i\omega_n) \right]. \end{aligned} \tag{A.23}$$

We find for the absorption spectrum

$$
\begin{aligned}
A(\mathbf{q},\omega) =& -2\mathrm{Im}\Pi(\mathbf{q},\omega-\mu) = \sum_{n=1}^{3} A_n(\mathbf{q},\omega),\\
A_1(\mathbf{q},\omega) =& -|\mu_{1,\mathbf{q}}|^2 \sum_{\sigma,s} s\big(u_{1,\mathbf{q}}^{\sigma,-s}\big)^2 2\pi\delta\big(\omega-\mu+sE_{\mathbf{q}}^{\sigma}\big),\\
A_2(\mathbf{q},\omega) =& \sum_{\sigma,\sigma'}\sum_{s,s'}\sum_{\mathbf{k}} |\mu_{12,\mathbf{k},\mathbf{q}}|^2 ss' \Big[\big(u_{1,\mathbf{k}}^{\sigma,s}\big)^2\big(u_{2,\mathbf{q}+\mathbf{k}}^{\sigma',s'}\big)^2 + u_{1,\mathbf{k}}^{\sigma,s}u_{2,\mathbf{k}}^{\sigma,-s}u_{1,\mathbf{q}+\mathbf{k}}^{\sigma',-s'}u_{2,\mathbf{q}+\mathbf{k}}^{\sigma',s'}\Big]\\
&\times\big[n_B\big(sE_{\mathbf{k}}^{\sigma}\big)-n_B\big(s'E_{\mathbf{q}+\mathbf{k}}^{\sigma'}\big)\big]2\pi\delta\big(\omega-\mu+sE_{\mathbf{k}}^{\sigma}-s'E_{\mathbf{q}+\mathbf{k}}^{\sigma'}\big),\\
A_3(\mathbf{q},\omega) =& -|\mu_{12,\mathbf{0},\mathbf{q}}|^2 \sum_{\sigma,s} s\Big[n_1\big(u_{2,\mathbf{q}}^{\sigma,-s}\big)^2 + n_2\big(u_{1,\mathbf{q}}^{\sigma,s}\big)^2 - 2\sqrt{n_1n_2}u_{1,\mathbf{q}}^{\sigma,s}u_{2,\mathbf{q}}^{\sigma,-s}\Big]\\
&\times 2\pi\delta\big(\omega-\mu+sE_{\mathbf{q}}^{\sigma}\big).
\end{aligned}
\tag{A.24}
$$

The luminescence spectrum is

$$
\begin{aligned}
I(\mathbf{q},\omega) =& I_0(\mathbf{q},\omega) + n_B(\omega-\mu)A(\mathbf{q},\omega) = \sum_{n=0}^{3} I_n(\mathbf{q},\omega),\\
I_0(\mathbf{q},\omega) =& \big(|\mu_{1,\mathbf{0}}|^2 n_1 + |\mu_{12,\mathbf{0},\mathbf{0}}|^2 n_1n_2\big)(2\pi)^3\delta(\omega-\mu)\delta(\mathbf{q}),\\
I_1(\mathbf{q},\omega) =& |\mu_{1,\mathbf{q}}|^2 \sum_{\sigma,s} s\big(u_{1,\mathbf{q}}^{\sigma,-s}\big)^2\big[1+n_B\big(sE_{\mathbf{q}}^{\sigma}\big)\big]2\pi\delta\big(\omega-\mu+sE_{\mathbf{q}}^{\sigma}\big),\\
I_2(\mathbf{q},\omega) =& \sum_{\sigma,\sigma'}\sum_{s,s'}\sum_{\mathbf{k}} |\mu_{12,\mathbf{k},\mathbf{q}}|^2 ss' \Big[\big(u_{1,\mathbf{k}}^{\sigma,s}\big)^2\big(u_{2,\mathbf{q}+\mathbf{k}}^{\sigma',-s'}\big)^2 + u_{1,\mathbf{k}}^{\sigma,s}u_{2,\mathbf{k}}^{\sigma,-s}u_{1,\mathbf{q}+\mathbf{k}}^{\sigma',s'}u_{2,\mathbf{q}+\mathbf{k}}^{\sigma',-s'}\Big]\\
&\times\big[1+n_B\big(sE_{\mathbf{k}}^{\sigma}\big)\big]\big[1+n_B\big(s'E_{\mathbf{q}+\mathbf{k}}^{i\sigma}\big)\big]2\pi\delta\big(\omega-\mu+sE_{\mathbf{k}}^{\sigma}+s'E_{\mathbf{q}+\mathbf{k}}^{\sigma'}\big),\\
I_3(\mathbf{q},\omega) =& |\mu_{12,\mathbf{0},\mathbf{q}}|^2 \sum_{\sigma,s} s\Big[n_1\big(u_{2,\mathbf{q}}^{\sigma,-s}\big)^2 + n_2\big(u_{1,\mathbf{q}}^{\sigma,s}\big)^2 - 2\sqrt{n_1n_2}u_{1,\mathbf{q}}^{\sigma,s}u_{2,\mathbf{q}}^{\sigma,-s}\Big]\\
&\times\big[1+n_B\big(sE_{\mathbf{q}}^{\sigma}\big)\big]2\pi\delta\big(\omega-\mu+sE_{\mathbf{q}}^{\sigma}\big).
\end{aligned}
\tag{A.25}
$$

The first term is due to coherent spontaneous emission of photons from the condensate, and is not present in the absorption spectrum. Actually, when $q\to 0$ the weight of the peak at $\omega=\mu$ diverges due to the divergence of the Bogoliubov coefficients. We deal with

this by integrating over a finite range of $\mathbf{q}$, $q < q_c$. Physically, the cutoff q_c represents a typical momentum due to scattering by inhomogeneities, phonons, etc., or the inverse trap size in the case of confined polaritons (Sec. 2.3).

Appendix B

Fermi velocity renormalization and magnetoexciton binding energy

In terms of the ILT energy $E_{-n\to n'}$, the effective Fermi velocity is defined as (assuming $n, n' \geq 0$):

$$v^{\text{eff}}_{F,-n\to n'} \equiv \frac{l_B}{\hbar}\frac{E_{-n\to n'}}{\sqrt{2n}+\sqrt{2n'}}. \tag{B.1}$$

In the main text we explained that the many-body correction $\Delta E_{-n\to n'}$ to the energy $E_{-n\to n'}$ of a $-n \to n'$ ILT (at zero momentum $q = 0$) has two parts: i) the correction due to the electron self-energies ΔE_m of $m = -n, n'$ LLs and ii) the magnetoexciton binding energy $\Delta_{-nn'}$:

$$\Delta E_{-n\to n'} = \Delta E'_n - \Delta E_{-n} - \Delta_{-nn'}. \tag{B.2}$$

We referred to the former as the Fermi velocity renormalization effect and to the latter as the excitonic effect. In this approach, the renormalized Fermi velocity of $-n \to n'$ ILT is given by

$$v_{F,-n\to n'} \equiv v_F + \frac{l_B}{\hbar}\frac{\Delta E'_n - \Delta E_{-n}}{\sqrt{2n}+\sqrt{2n'}}, \tag{B.3}$$

where v_F is the bare Fermi velocity, so that $v^{\text{eff}}_{F,-n\to n'}$ and $v_{F,-n\to n'}$ are related by

$$v^{\text{eff}}_{F,-n\to n'} = v_{F,-n\to n'} - \frac{l_B}{\hbar}\frac{\Delta_{-nn'}}{\sqrt{2n}+\sqrt{2n'}}. \tag{B.4}$$

Following previous work [67], we compute the quantities that enter these equations as follows:

$$\Delta E_{n'} - \Delta E_{-n} = -\int \frac{d^2q}{(2\pi)^2} v(q) I_{-n,n'}(q), \tag{B.5}$$

$$I_{-n,n'}(q) = \sum_m f_m \left(|g_{m,n'}(q)|^2 - |g_{m,-n}(q)|^2 \right),$$

$$\Delta_{-nn'} = \int \frac{d^2q}{(2\pi)^2} v(q) g_{-n,-n}(q) g_{n'n'}(q). \tag{B.6}$$

Here f_m is again the Fermi occupation factor of mth LL [$f_m = \Theta(-m)$ if $m \neq 0$ and $f_0 = 1/2$], and $v(q) = (2\pi e^2)/(\epsilon(q)q)$ is the screened Coulomb interaction. The matrix element $F_{nm}(q)$ is

$$\begin{aligned} F_{nm}(q) &= \frac{2}{\pi x} \left| \mathrm{sgn}(mn) A_{n_<,n_>}(x) + A_{n_<-1,n_>-1}(x) \right|^2 \\ n_< &= \min(|m|,|n|),\ n_> = \max(|m|,|n|),\ x \equiv \frac{q^2 l_B^2}{2} \\ A_{n_1,n_2}(x) &= \left(\frac{1+\delta_{0,n_1}}{2} \frac{1+\delta_{0,n_1}}{2} \frac{n_1!}{n_2!} x^{n_2-n_1} \right)^{1/2} L_{n_1}^{n_2-n_1}(x) e^{-x/2}, \end{aligned} \tag{B.7}$$

where $L_n^\alpha(x)$ is the associated Laguerre polynomial. We neglect dynamical screening effects; however, we include static screening through the momentum-dependent dielectric function

$$\epsilon(q) = \kappa(q) + \kappa_g(q), \tag{B.8a}$$

$$\kappa(q) = \frac{\varepsilon_{\mathrm{hBN}}}{2} \left(\frac{\epsilon_{\mathrm{hBN}} \tanh \xi_{\mathrm{hBN}} q d_1 + \epsilon_0}{\epsilon_0 \tanh \xi_{\mathrm{hBN}} q d_1 + \epsilon_{\mathrm{hBN}}} + \frac{\epsilon_{\mathrm{hBN}} \tanh \xi_{\mathrm{hBN}} q d_2 + \epsilon_{\mathrm{SOS}}}{\epsilon_{\mathrm{SOS}} \tanh \xi_{\mathrm{hBN}} q d_2 + \epsilon_{\mathrm{hBN}}} \right), \tag{B.8b}$$

$$\epsilon_{\mathrm{SOS}} = \epsilon_{\mathrm{SiO2}} \frac{\epsilon_{\mathrm{SiO2}} \tanh q d_3 + \epsilon_{\mathrm{Si}}}{\epsilon_{\mathrm{Si}} \tanh q d_3 + \epsilon_{\mathrm{SiO2}}},$$

$$\kappa_g(q) = 2\pi i q \omega^{-1} \sigma_{xx}(q,\omega). \tag{B.8c}$$

Function $\kappa(q)$ has the meaning of the effective dielectric constant of graphene environment. Parameter $\epsilon_{\rm hBN} = (\epsilon^{\perp}_{\rm hBN}\epsilon^{\parallel}_{\rm hBN})^{1/2} = 4.9$ is the dc (i.e., $\omega = 0$) dielectric constant of hBN defined as the geometric average of its in-plane and out-of-plane dielectric constants, $\xi_{\rm hBN} = (\epsilon^{\perp}_{\rm hBN}/\epsilon^{\parallel}_{\rm hBN})^{1/2}$ is the hBN anisotropy factor, $\epsilon_{\rm SiO2} = 3.9$ is the dc dielectric constant of SiO2, $\epsilon_{\rm Si} = 11.7$ is the dc dielectric constant of Si, and $\epsilon_0 = 1$ is the dielectric constant of vacuum. Parameters $d_1 = 16$ nm and $d_2 = 55$ nm are thicknesses of the top and bottom hBN layers, respectively, and $d_3 = 285$ nm is the SiO2 thickness. Function $\kappa_g(q)$ specified by Eq. (B.8c) accounts for the (static) screening of the Coulomb potential by electrons in graphene and $\sigma_{xx}(q,\omega)$ is the longitudinal conductivity of graphene in the presence of magnetic field. Representative plots of functions $\kappa(q)$, $\kappa_g(q)$, and $\epsilon(q)$ are shown in Fig. B.1(a)-(b).

As one can see from these graphs, $\kappa(q)$ (the middle curve) is equal to $(\epsilon_0 + \epsilon_{\rm Si})/2$ at zero q, then has a small dip to approach $(\epsilon_0 + \epsilon_{\rm SiO2})/2$ within a narrow range of relatively low momenta $d_3^{-1} \leq q \leq d_2^{-1}$, then rises and tends to $\epsilon_{\rm hBN}$ at $q \geq d_1^{-1} = 6.7 \times 10^5\,{\rm cm}^{-1}$. The total dielectric function $\epsilon(q)$ (the top curve) shows the same small dip at low q, goes through a modest maximum, and then approaches the limiting value

$$\epsilon_\infty = \epsilon_{\rm hBN} + \frac{\pi\alpha}{2},\ \alpha = \frac{e^2}{\hbar v_F^{\rm ren}} \approx 2.2, \tag{B.9}$$

at high momenta $q \gg l_B^{-1}$.

The calculation of the binding energies $\Delta_{-nn'}$ in Eq. (B.6) involves numerical evaluation of four integrals of the form

$$\int \frac{d^2q}{(2\pi)^2} v(q) L_n\left(\frac{q^2 l_B^2}{2}\right) L_{n'}\left(\frac{q^2 l_B^2}{2}\right), \tag{B.10}$$

which are well behaved. On the other hand, the integral for the self-energy in Eq. (B.5)

diverges at large momenta $ql_B \gg \sqrt{n}, \sqrt{n'}$ because

$$I_{-n,n'}(q) \simeq -\frac{\sqrt{2n}+\sqrt{2n'}}{4ql_B}, \tag{B.11}$$

as can be deduced from Eqs. (B.7) and (B.5). We regularize this divergence by renormalization, i.e., subtraction of $v_{F,-n\to n'}$ evaluated at some reference field B_0. Let $l_0 \equiv l_B(B_0)$ be the magnetic length at B_0. Since the high momenta enter through the product ql_B, we can rescale the integration variable in Eq. (B.5) by the ratio $R = l_B/l_0 = \sqrt{B_0/B}$ to cancel the divergence. Performing the subtraction, we find

$$v_{F,-n\to n'}(B) = v_{F,-n\to n'}(B_0) - \frac{e^2}{8\hbar\epsilon_\infty}\ln\left(\frac{B}{B_0}\right) + \Delta v_{F,-n\to n'}(B, B_0), \tag{B.12}$$

where

$$\Delta v_{F,-n\to n'}(B, B_0) = -\frac{l_B}{\hbar(\sqrt{2n}+\sqrt{2n'})}\int \frac{d^2q}{(2\pi)^2}[v(q) - Rv(Rq)]I_{-n,n'}(q). \tag{B.13}$$

Note that if the dielectric function is replaced by a constant, e.g., ϵ_∞, then $v(q) = 2\pi e^2/(\epsilon_\infty q)$ and $\Delta v_{F,-n\to n'}(B, B_0)$ vanishes identically. In this case, the conventional logarithmic-in-B rule [67] for the Fermi velocity renormalization is recovered.

In our experiment, all the ILTs were measured at the same photon energy $\hbar\omega$. Therefore, it is convenient to select a particular ILT, e.g., $-2 \to 3$, as a reference, so that $B_0 = B_{-2\to 3}$, where $B_{-2\to 3}$ is the field at which this ILT occurs. Eq. (B.12) entails

$$\begin{aligned} v_{F,-n\to n'} =& v_{F,-2\to 3} - \frac{e^2}{8\hbar\epsilon_\infty}\ln\left(\frac{B}{B_{-2\to 3}}\right) \\ &- \frac{l_B}{\sqrt{2}\hbar}\int \frac{d^2q}{(2\pi)^2}\left[v(q)\frac{I_{-n,n'}(q)}{\sqrt{n}+\sqrt{n'}} - Rv(Rq)\frac{I_{-2,3}(q)}{\sqrt{2}+\sqrt{3}}\right]. \end{aligned} \tag{B.14}$$

Our calculations using this formula show that $v_{F,-n\to n'}$ is almost the same for all the ILTs, as shown in Fig B.1(c). On the other hand, $v^{\text{eff}}_{F,-n\to n'}$, given by Eq. (B.4) , exhibits

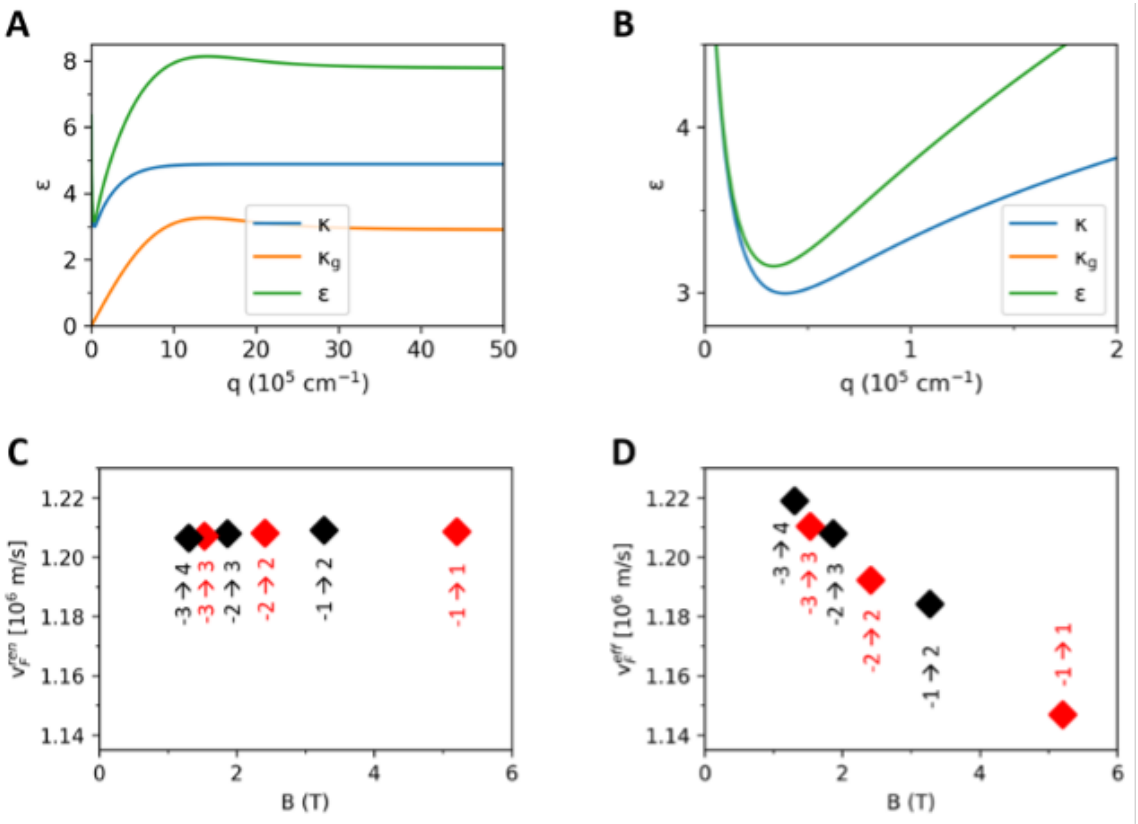

Figure B.1. Calculation of the Fermi velocities and many-body effects. (A and B) Effective dielectric function for electrons in graphene. Functions $\kappa(q)$, $\kappa_g(q)$, and $\epsilon(q)$ defined by Eq. 19 (A to C) for $B = 3.35$ T. (B) shows a magnification of the small dip at low q that is observed for $\kappa_g(q)$ and $\epsilon(q)$. (C) Renormalized Fermi velocities given by Eq. 26. (D) Effective Fermi velocities defined by Eq. 17 that include excitonic corrections.

characteristic dips at $n = n'$ because of relatively larger excitonic corrections $\Delta_{-n,n'}$ at such ILTs, see Fig B.1(d).

To obtain the experimental binding energies $\Delta_{\text{exp},-n,n'}$, we use Eqs. (B.4) and (B.14) but set the effective Fermi velocities equal to their experimentally measured values $v^{\text{eff}}_{F,\text{exp},m\to n}$. Solving for $\Delta_{-n,n'}$, we obtain

$$\begin{aligned}\Delta_{\text{exp},-n,n'} =&\frac{\sqrt{2}\hbar}{l_B}(\sqrt{n}+\sqrt{n'})\Bigg\{v^{\text{eff}}_{F,-2\to 3} - \frac{e^2}{8\hbar\epsilon_\infty}\ln\left(\frac{B}{B_{-2\to 3}}\right)\\ &- \frac{l_B}{\sqrt{2}\hbar}\int\frac{d^2q}{(2\pi)^2}\left[v(q)\frac{I_{-n,n'}(q)}{\sqrt{n}+\sqrt{n'}} - Rv(Rq)\frac{I_{-2,3}(q)}{\sqrt{2}+\sqrt{3}}\right] + \frac{l_B}{\sqrt{2}\hbar}\frac{\Delta_{-2,3}}{\sqrt{2}+\sqrt{3}}\Bigg\}.\end{aligned} \tag{B.15}$$

This gives $\Delta_{\text{exp},-n,n'}$ in terms of $v^{\text{eff}}_{F,\text{exp},-n\to n'}$ and $v^{\text{eff}}_{F,\text{exp},-2\to 3}$, the calculated electron self-energies, and the calculated binding energy $\Delta_{-2,3}$ for the reference ILT.

Appendix C

Quantum theory of Landau-phonon polaritons

We define creation operators $a^\dagger_{l,\mathbf{q}}$ for the hBN hyperbolic phonon mode l with in-plane momentum $\mathbf{q}$, and $b^\dagger_{nm,\mathbf{q}}$ for the $m \to n$ graphene magnetoexciton. There is a Fröhlich coupling between the modes given by the Hamiltonian

$$H_{\text{int}} = \frac{1}{A}\sum_{\mathbf{q}} \hat{\Phi}_{\mathbf{q}}(z)\hat{\rho}_{-\mathbf{q}}, \tag{C.1}$$

Here the operators $\hat{\rho}_{\mathbf{q}}$ and $\hat{\Phi}_{\mathbf{q}}(z)$ correspond to the charge density of the graphene electrons and the electrostatic potential due to hBN phonons, respectively, with z the position of the graphene layer, and A is the area of the system. We may express the charge density operator as [67]

$$\hat{\rho}_{\mathbf{q}} = \sum_{n>m} \rho_{nm,\mathbf{q}}(b_{nm,\mathbf{q}} + b^\dagger_{nm,-\mathbf{q}}), \tag{C.2}$$

where

$$\rho_{nm,\mathbf{q}} = e\left(\frac{2A}{\pi\ell^2}\right)^{1/2}[f_{n_<-1,n_>-1,\mathbf{q}} + \mathrm{sgn}(nm) f_{n_<,n_>,\mathbf{q}}],$$
$$n_< = \min(|n|,|m|), \quad n_> = \max(|n|,|m|),$$
$$f_{n_1,n_2,\mathbf{q}} = \left(\frac{1+\delta_{0,n_1}}{2}\frac{1+\delta_{0,n_2}}{2}\frac{n_1!}{n_2!}\right)^{1/2}\left[\frac{\ell(q_x - iq_y)}{\sqrt{2}}\right]^{n_2-n_1} L_{n_1}^{n_2-n_1}(\tfrac{1}{2}\ell^2 q^2)\exp(-\tfrac{1}{4}\ell^2 q^2), \tag{C.3}$$

with ℓ the magnetic length.

The potential of the $(l,\mathbf{q})$ phonon mode takes the form $\Phi_{l,\mathbf{q}}(z)e^{i\mathbf{q}\cdot\mathbf{x}}$, with $\mathbf{x}$ the in-plane coordinate, in terms of which the potential operator is

$$\hat{\Phi}_{\mathbf{q}}(z) = \frac{A}{2}\sum_l \Phi_{l,\mathbf{q}}(z)(a_{l,\mathbf{q}} + a^\dagger_{l,-\mathbf{q}}). \tag{C.4}$$

We determine $\Phi_{l,\mathbf{q}}(z)$ and the mode frequency $\omega_{l,\mathbf{q}}$ by solving Laplace's equation with appropriate boundary conditions. Let d be the thickness of the hBN slab and let z be the coordinate along the optical axis, with the hBN-substrate interface at $z = 0$. We denote the hBN dielectric functions perpendicular and parallel to the optical axis by $\epsilon_\perp$ and $\epsilon_\parallel$, respectively, the substrate dielectric constant by ϵ_s and the dielectric constant of the medium above hBN by ϵ_a [66]. The z-component of momentum of the hBN hyperbolic phonon mode is

$$k_e^z = iq\frac{\sqrt{\varepsilon_\perp}}{\sqrt{\varepsilon_\parallel}} \equiv \frac{q}{\psi}. \tag{C.5}$$

The reflection coefficients going from the hBN to medium $j = s, a$ may be written as $r_j = e^{2i\phi_j}$, where

$$\phi_j = \arctan\left(\frac{\varepsilon_j}{\varepsilon_\perp \psi}\right). \tag{C.6}$$

In the absence of the graphene the modes are determined by $1 - r_a r_s e^{2ik_e^z d} = 0$, which

implies the quantization condition

$$2k_e^z d + 2\phi_a + 2\phi_s = -2\pi l, \quad l = 0, 1, 2, \ldots \tag{C.7}$$

Solving for q, we find

$$q = -\frac{\psi}{d}(\phi_a + \phi_s + \pi l). \tag{C.8}$$

This expression for $q(\omega)$ may be inverted to find the hyperbolic phonon polariton dispersion $\omega_{l,\mathbf{q}}$. We also have

$$\hat{\Phi}_{l,\mathbf{q}}(z) = \Phi_0 \begin{cases} \cos\phi_s e^{qz}, & z < 0 \\ \cos(k_e^z z + \phi_s), & 0 \le z \le d \\ (-1)^l \cos\phi_a e^{-q(z-d)}, & z > d. \end{cases} \tag{C.9}$$

The normalization factor Φ_0 is chosen such that the total energy of the mode is equal to $\hbar\omega_{l,\mathbf{q}}$:

$$\frac{1}{16\pi}\left\{\int_0^d dz\left[\frac{d}{d\omega}(\omega\epsilon_\perp)|\mathbf{E}_\perp|^2 + \frac{d}{d\omega}(\omega\epsilon_\parallel)|\mathbf{E}_\parallel|^2\right] + \int_{-\infty}^0 dz\,\epsilon_s|\mathbf{E}|^2 + \int_d^\infty dz\,\epsilon_a|\mathbf{E}|^2\right\} = \hbar\omega, \tag{C.10}$$

which implies

$$\Phi_0 = \left(\frac{qA}{32\pi\hbar}\frac{d\varepsilon_\perp}{d\omega}\right)^{-1/2}\left(\frac{1}{[-\varepsilon_\perp]}\left\{\left[1 + (\varepsilon_a/\varepsilon_\perp\psi)^2\right]^{-1} + \left[1 + (\varepsilon_s/\varepsilon_\perp\psi)^2\right]^{-1}\right\} + qd\right)^{-1/2}. \tag{C.11}$$

This expression is evaluated at $\omega_{l,\mathbf{q}}$, which we assume to be in the upper Restrahlen band, hence we neglect the weak frequency dependence of $\epsilon_\parallel$.

We consider the case where one of the phonon modes $(l, \mathbf{q})$ becomes resonant with

an $n \to m$ magnetoexciton. Including N layers of graphene, the Hamiltonian describing the coupled modes is

$$H = \sum_{\mathbf{q}} \Big[\omega_{l,\mathbf{q}} a^\dagger_{l,\mathbf{q}} a_{l,\mathbf{q}} + \omega^x_{nm,\mathbf{q}} \sum_{i=1}^{N} b^\dagger_{i,nm,\mathbf{q}} b_{i,nm,\mathbf{q}} + \sum_{i=1}^{N} \tfrac{1}{2} \Phi_{l,\mathbf{q}}(z_i) \rho_{nm,-\mathbf{q}} (a_{l,\mathbf{q}} + a^\dagger_{l,-\mathbf{q}})(b_{i,nm,-\mathbf{q}} + b^\dagger_{i,nm,\mathbf{q}}) \Big], \tag{C.12}$$

with $\omega^x_{nm,\mathbf{q}}$ the magnetoexciton energy and z_i the position of the ith graphene layer. Keeping only the resonant terms in $H_{\rm int}$, the Hamiltonian reduces to

$$H = \sum_{\mathbf{q}} \left[\omega_{l,\mathbf{q}} a^\dagger_{l,\mathbf{q}} a_{l,\mathbf{q}} + \omega^x_{nm,\mathbf{q}} \sum_{i=1}^{N} b^\dagger_{i,nm,\mathbf{q}} b_{i,nm,\mathbf{q}} + \sum_{i=1}^{N} \tfrac{1}{2} \Phi_{l,\mathbf{q}}(z_i) \rho_{nm,-\mathbf{q}} (a_{l,\mathbf{q}} b^\dagger_{i,nm,\mathbf{q}} + \text{H.c.}) \right]. \tag{C.13}$$

It may be diagonalized by a suitable linear transformation of the operators. We find upper and lower polariton branches with a gap

$$\Delta = \left[\sum_{i=1}^{N} |\Phi_{l,\mathbf{q}}(z_i) \rho_{nm,-\mathbf{q}}|^2 \right]^{1/2}. \tag{C.14}$$

Substituting in the expressions for $\Phi_{l,\mathbf{q}}(z_i)$ and $\rho_{nm,\mathbf{q}}$ found above, we obtain

$$\begin{aligned} &\Delta = \sqrt{\frac{\mathcal{N}\mathcal{E}\mu}{d}}, \quad \mu = 16\pi e^2 F_{nm}/\hbar, \quad \mathcal{E} = \sum_{i=1}^{N} \cos^2(k^z_e z_i + \phi_s), \\ &\mathcal{N} = qd \left(\frac{1}{[-\varepsilon_\perp]} \left\{ \left[1 + (\varepsilon_a/\varepsilon_\perp \psi)^2\right]^{-1} + \left[1 + (\varepsilon_s/\varepsilon_\perp \psi)^2\right]^{-1} \right\} + qd \right)^{-1} \left(\frac{d\varepsilon_\perp}{d\omega} \right)^{-1}, \end{aligned} \tag{C.15}$$

which is evaluated at the frequency ω^x_{nm}, with q the momentum of the phonon mode at this frequency. The matrix element F_{nm} is defined in Eq. (B.7). We assume the N graphene layers are equally spaced. For large N, we may replace the sum by an integral and the

formula becomes

$$\Delta = \sqrt{\frac{\mathcal{N}\bar{\mathcal{E}}\mu}{L}}, \quad \bar{\mathcal{E}} = \tfrac{1}{2}\left\{1 - (2k_e^z d)^{-1}[\sin(2\phi_a) + \sin(2\phi_s)]\right\}, \tag{C.16}$$

with $L = d/N$, which is Eq. (3.3) of the main text.

Appendix D

Single-particle spectrum and Drude weight

In the Efimkin-MacDonald model [141], the scattering matrix takes the form

$$S = \begin{pmatrix} \sqrt{P_f}e^{i\chi} & \sqrt{P_d} & \sqrt{P_d} \\ \sqrt{P_d} & \sqrt{P_f}e^{i\chi} & \sqrt{P_d} \\ \sqrt{P_d} & \sqrt{P_d} & \sqrt{P_f}e^{i\chi} \end{pmatrix}, \tag{D.1}$$

where P_f and P_d are respectively the forward scattering and deflection probabilities and $\chi = \arccos(-\sqrt{P_d}/2\sqrt{P_f})$. The energy spectrum $\varepsilon(\mathbf{k})$ is determined by solving the eigenvalue problem

$$\Lambda_{\mathbf{k}} S \psi_{\mathbf{k}} = e^{-i\varepsilon(\mathbf{k})L/v}\psi_{\mathbf{k}}, \tag{D.2}$$

with $\psi_{\mathbf{k}} = (\psi_{1,\mathbf{k}}, \psi_{2,\mathbf{k}}, \psi_{3,\mathbf{k}})$ the vector of amplitudes on the three links in a unit cell, $\Lambda_{\mathbf{k}} = \mathrm{diag}(e^{-ik_1}, e^{-ik_2}, e^{-ik_3})$ and $k_i = \mathbf{k}\cdot\mathbf{l}_i$ (note $k_3 = -k_1 - k_2$).

The Drude weight is given by

$$D\delta_{\alpha\beta} = \pi e^2 \sum_n \int \frac{d^2k}{(2\pi)^2} \delta[\varepsilon_n(\mathbf{k}) - \varepsilon_F] v_{n,\alpha}(\mathbf{k}) v_{n,\beta}(\mathbf{k}), \tag{D.3}$$

where n is the band index and $\mathbf{v}_n(\mathbf{k}) = \nabla_{\mathbf{k}}\varepsilon_n$. We have neglected the degeneracy factors, which are specified in Eq. (5.2) of the main text. From now on we use units where $L = 1$,

$v = 1$, and $e = 1$. Averaging Eq. (D.3) over one period we obtain

$$\bar{D}\delta_{\alpha\beta} = \frac{1}{2}\sum_n \int \frac{d^2k}{(2\pi)^2} v_{n,\alpha}(\mathbf{k}) v_{n,\beta}(\mathbf{k}), \tag{D.4}$$

or equivalently

$$\bar{D} = \frac{\sqrt{3}}{4}\sum_n \int_0^{2\pi}\int_0^{2\pi} \frac{dk_1 dk_2}{(2\pi)^2}\left(\frac{\partial \varepsilon_n}{\partial k_1}\right)^2. \tag{D.5}$$

In the case of forward scattering, $P_f = 1$, we have $\varepsilon_i = k_i$, so the energy bands are three intersecting planes. The corresponding Drude weight is $D_{\max} = \frac{\sqrt{3}}{2}$.

Now consider the case of weak deflection, $P_d \ll 1$. The off-diagonal terms in S split the degeneracies near the intersections of the planes along the lines $k_i = k_j$. In the vicinity of these lines there is an anticrossing and the resulting energy bands are

$$\varepsilon_{ij,\pm} = \frac{1}{2}\left[k_i + k_j \pm \sqrt{(k_i - k_j)^2 + 4P_d}\right]. \tag{D.6}$$

This leads to a correction to the Drude weight $\Delta\bar{D}_{ij}$ of order $\sqrt{P_d}$. For example,

$$\begin{aligned}
\Delta\bar{D}_{12} &= \frac{\sqrt{3}}{4}\int_0^{2\pi}\int_0^{2\pi}\frac{dk_1 dk_2}{(2\pi)^2}\left[\left(\frac{\partial\varepsilon_{12,+}}{\partial k_1}\right)^2 + \left(\frac{\partial\varepsilon_{12,-}}{\partial k_1}\right)^2 - 1\right] \\
&= -\frac{\sqrt{3}}{2}\int_0^{2\pi}\int_0^{2\pi}\frac{dk_1 dk_2}{(2\pi)^2}\frac{P_d}{(k_1-k_2)^2 + 4P_d} \\
&\simeq -\frac{\sqrt{3}}{2}\int_{-\infty}^{\infty}\frac{dk}{2\pi}\frac{P_d}{k^2 + 4P_d} \\
&= -\frac{\sqrt{3}}{8}\sqrt{P_d}.
\end{aligned} \tag{D.7}$$

Similarly, we find $\Delta\bar{D}_{13} = -\frac{\sqrt{3}}{2}\sqrt{P_d}$ and $\Delta\bar{D}_{23} = -\frac{\sqrt{3}}{8}\sqrt{P_d}$. Therefore, to leading order in $\sqrt{P_d}$,

$$\bar{D} = D_{\max}\left(1 - \frac{3}{2}\sqrt{P_d}\right), \tag{D.8}$$

which is Eq. (5.6) in the main text.

Appendix E

Bosonization description of collective modes

We begin by expressing the long-wavelength electron density fluctuation n_i and the current j_i of mode i in terms of bosonic fields ϕ_i, Π_i such that

$$n_i = -\frac{1}{\pi}\partial_x \phi_i \,, \qquad j_i = ev\Pi_i \,. \tag{E.1}$$

These fields satisfy the canonical commutation relations $[\phi_i(x), \Pi_j(x')] = i\delta_{ij}\delta(x-x')$. The effective Hamiltonian for an isolated 1D wire is $H = H_0 + H_{\rm int}$ where

$$H_0 = \sum_{i=1}^{N} \frac{1}{2\pi} \int dx\ \hbar v \left[\pi^2 \Pi_i^2(x) + (\partial_x \phi_i)^2\right] \tag{E.2}$$

is the kinetic energy and

$$H_{\rm int} = \frac{1}{2\pi^2} \sum_{ij} \int dx dx' \partial_x \phi_i U(x-x') \partial_{x'} \phi_j \tag{E.3}$$

is the interaction energy, with $U(x)$ the effective 1D interaction kernel.

Consider a linear transformation $\varphi_i(x) = \sum_j O_{ij}\phi_j(x)$ where O_{ij} are constants forming an orthogonal matrix. Such a transformation preserves the commutation relations among the fields with the first row $O_{1j} = 1/\sqrt{N}$. The corresponding canonical momenta

are denoted by Π_i. Under this definition, the total density and current in the wire are expressed solely in terms of $i = 1$ field:

$$n = -\frac{\sqrt{N}}{\pi}\,\partial_x\varphi_1\,, \quad j = \sqrt{N}\,ev\Pi_1\,. \tag{E.4}$$

Therefore, φ_1 represents the charged excitation (plasmon) whereas the remaining φ_i's with $i \neq 1$ describe neutral collective modes. The Hamiltonian becomes

$$\begin{aligned} H =& \sum_{i=1}^{N} \frac{1}{2\pi} \int dx\ \hbar v \left[\pi^2 \Pi_i^2(x) + (\partial_x\varphi_i)^2\right] \\ &+ \frac{N}{2\pi^2} \int dx \int dx' \partial_x\varphi_1 U(x-x') \partial_{x'}\varphi_1. \end{aligned} \tag{E.5}$$

The corresponding equations of motion are

$$\begin{aligned} \partial_t\varphi_i &= \pi v \Pi_i, \\ \partial_t\Pi_i &= \frac{1}{\pi} v \partial_x^2\varphi_i + \delta_{i1}\frac{N}{\pi^2\hbar}\partial_x \int dx' U(x-x')\partial_{x'}\varphi_1. \end{aligned} \tag{E.6}$$

With a harmonic time dependence $e^{-i\omega t}$ of the fields, this implies Eqs. (5.19)–(5.21) of the main text.

Appendix F

Modeling of near-field images

Let $\mathbf{r}$ be the position vector in the plane of the sample with the z-axis perpendicular to this plane. The light scattered by the tip or an impurity at position $\mathbf{r}'$ produces an external potential $\Phi_{\text{ext}}(\mathbf{r}-\mathbf{r}')$ on the sample surface. The total electrostatic potential on the surface is then given by $\Phi_{\text{tot}}(\mathbf{r}, z=0) = \int d\mathbf{r}'' \epsilon^{-1}(\mathbf{r}, \mathbf{r}''; \omega)\Phi_{\text{ext}}(\mathbf{r}''-\mathbf{r}')$. Fourier transforming this, we obtain

$$\tilde{\Phi}_{\text{tot},\mathbf{G}}(\mathbf{q}, 0) = \sum_{\mathbf{G}'} \epsilon^{-1}_{\mathbf{G}\mathbf{G}'}(\mathbf{q}, \omega) F_l(\mathbf{q}+\mathbf{G}') e^{-i(\mathbf{q}+\mathbf{G}')\cdot\mathbf{r}'}, \tag{F.1}$$

where F_l is the Fourier transform of Φ_{ext}. In the quasi-static approximation the potential satisfies Laplace's equation above the sample, so at position z it is given by

$$\tilde{\Phi}_{\text{tot},\mathbf{G}}(\mathbf{q}, z) = e^{-|\mathbf{q}+\mathbf{G}|z} \sum_{\mathbf{G}'} \epsilon^{-1}_{\mathbf{G}\mathbf{G}'}(\mathbf{q}, \omega) F_l(\mathbf{q}+\mathbf{G}') e^{-i(\mathbf{q}+\mathbf{G}')\cdot\mathbf{r}'}. \tag{F.2}$$

The measured near-field signal is proportional to the induced dipole moment on the probe, given by the probe polarizability times the total electric field at its position, $-\partial_{z_{\text{tip}}}\Phi_{\text{tot}}(\mathbf{r}, z_{\text{tip}})$, with z_{tip} the tip-sample distance. Fourier transforming $\tilde{\Phi}_{\text{tot}}$ back to real

space and differentiating with respect to z, we find that the signal is proportional to

$$G(\mathbf{r},\mathbf{r}';\omega) = \sum_{\mathbf{G},\mathbf{G}'} \int \frac{d^2k}{(2\pi)^2} e^{i(\mathbf{q}+\mathbf{G})\cdot\mathbf{r}} e^{-i(\mathbf{q}+\mathbf{G}')\cdot\mathbf{r}'} \times F_d(\mathbf{q}+\mathbf{G})\epsilon^{-1}_{\mathbf{G}\mathbf{G}'}(\mathbf{q},\omega)F_l(\mathbf{q}+\mathbf{G}'). \tag{F.3}$$

with $F_d(\mathbf{q}) = qe^{-qz_{\text{tip}}}$. This is Eq. (5.45) of the main text. The form of $F_l(\mathbf{q})$ depends on whether the tip or an impurity launches plasmons. For tip-launched plasmons, we model the tip as a point dipole oriented along the z direction, so it produces a potential of the form $(|\mathbf{r}-\mathbf{r}'|^2 + z_{\text{tip}}^2)^{-3/2}$. The form factor is the Fourier transform of this: $F_l(\mathbf{q}) = e^{-qz_{\text{tip}}}$. On the other hand, for plasmons launched by an impurity we take $F_l(\mathbf{q}) = 1$. In practice, z_{tip} varies in time as the probe oscillates at a finite frequency, and the signal is demodulated at some harmonic of this frequency to suppress the background signal [156]. However, here we ignore this complication and assume z_{tip} to be fixed.

Bibliography

[1] Tsuneya Ando, Alan B. Fowler, and Frank Stern. Electronic properties of two-dimensional systems. *Reviews of Modern Physics*, 54(2):437–672, 1982.

[2] K. S. Novoselov, A. Mishchenko, A. Carvalho, and A. H. Castro Neto. 2D materials and van der Waals heterostructures. *Science*, 353(6298), 2016.

[3] Jeroen W. G. Wilder, Liesbeth C. Venema, Andrew G. Rinzler, Richard E. Smalley, and Cees Dekker. Electronic structure of atomically resolved carbon nanotubes. *Nature*, 391(6662):59–62, 1998.

[4] M. Z. Hasan and C. L. Kane. Colloquium: Topological insulators. *Reviews of Modern Physics*, 82(4):3045–3067, 2010.

[5] Yuan Cao, Valla Fatemi, Ahmet Demir, Shiang Fang, Spencer L. Tomarken, Jason Y. Luo, Javier D. Sanchez-Yamagishi, Kenji Watanabe, Takashi Taniguchi, Efthimios Kaxiras, Ray C. Ashoori, and Pablo Jarillo-Herrero. Correlated insulator behaviour at half-filling in magic-angle graphene superlattices. *Nature*, 556(7699):80–84, 2018.

[6] Yuan Cao, Valla Fatemi, Shiang Fang, Kenji Watanabe, Takashi Taniguchi, Efthimios Kaxiras, and Pablo Jarillo-Herrero. Unconventional superconductivity in magic-angle graphene superlattices. *Nature*, 556(7699):43–50, 2018.

[7] Thierry Giamarchi. *Quantum Physics in One Dimension*. Oxford University Press, 2003.

[8] Sviatoslav Anatolevich Moskalenko and David W. Snoke. *Bose-Einstein condensation of excitons and biexcitons*. Cambridge University Press, Cambridge, 2000. Title from publisher's bibliographic system (viewed on 05 Oct 2015).

[9] M. M. Fogler, L. V. Butov, and K. S. Novoselov. High-temperature superfluidity with indirect excitons in van der Waals heterostructures. *Nature Communications*, 5(1):4555, 2014.

[10] J. J. Hopfield. Theory of the contribution of excitons to the complex dielectric

constant of crystals. *Phys. Rev.*, 112(5):1555–1567, 1958.

[11] Gabriele Giuliani and Giovanni Vignale. *Quantum theory of the electron liquid*. Cambridge University Press, Cambridge, UK, 2005. Includes bibliographical references (pages 742-764) and index.

[12] B. Vermilyea and M. M. Fogler. Feshbach resonance of heavy exciton-polaritons. *Physical Review B*, 109(11):115401, 2024.

[13] Alexey Kavokin. *Microcavities*. Oxford University Press, 2011.

[14] Daniele Sanvitto and Stéphane Kéna-Cohen. The road towards polaritonic devices. *Nat. Mater.*, 15(10):1061–1073, 2016.

[15] Hui Deng, Hartmut Haug, and Yoshihisa Yamamoto. Exciton-polariton Bose-Einstein condensation. *Rev. Mod. Phys.*, 82(2):1489–1537, 2010.

[16] Iacopo Carusotto and Cristiano Ciuti. Quantum fluids of light. *Rev. Mod. Phys.*, 85(1):299–366, 2013.

[17] Michiel Wouters. Resonant polariton-polariton scattering in semiconductor microcavities. *Phys. Rev. B*, 76(4):045319, 2007.

[18] I. Carusotto, T. Volz, and A. Imamoğlu. Feshbach blockade: Single-photon nonlinear optics using resonantly enhanced cavity polariton scattering from biexciton states. *Europhys. Lett.*, 90(3):37001, 2010.

[19] N. Takemura, S. Trebaol, M. Wouters, M. T. Portella-Oberli, and B. Deveaud. Polaritonic Feshbach resonance. *Nat. Phys.*, 10(7):500–504, 2014.

[20] N. Takemura, M. D. Anderson, M. Navadeh-Toupchi, D. Y. Oberli, M. T. Portella-Oberli, and B. Deveaud. Spin anisotropic interactions of lower polaritons in the vicinity of polaritonic Feshbach resonance. *Phys. Rev. B*, 95(20):205303, 2017.

[21] M. Navadeh-Toupchi, N. Takemura, M. D. Anderson, D. Y. Oberli, and M. T. Portella-Oberli. Polaritonic cross Feshbach resonance. *Phys. Rev. Lett.*, 122(4):047402, 2019.

[22] M. A. Bastarrachea-Magnani, A. Camacho-Guardian, M. Wouters, and G. M. Bruun. Strong interactions and biexcitons in a polariton mixture. *Phys. Rev. B.*, 100(19):195301, 2019.

[23] P. Borri, W. Langbein, U. Woggon, J. R. Jensen, and J. M. Hvam. Biexcitons or bipolaritons in a semiconductor microcavity. *Phys. Rev. B*, 62(12):R7763–R7766, 2000.

[24] A. L. Ivanov and H. Haug. Self-consistent theory of the biexciton optical nonlinearity. *Phys. Rev. B*, 48(3):1490–1504, 1993.

[25] A. L. Ivanov and H. Haug. Radiative renormalizations for excitonic molecules. *Phys. Rev. Lett.*, 74(3):438–441, 1995.

[26] A.L. Ivanov, H. Haug, and L.V. Keldysh. Optics of excitonic molecules in semiconductors and semiconductor microstructures. *Phys. Rep.*, 296(5-6):237–336, 1998.

[27] A. L. Ivanov, P. Borri, W. Langbein, and U. Woggon. Radiative corrections to the excitonic molecule state in GaAs microcavities. *Phys. Rev. B*, 69(7):075312, 2004.

[28] D. N. Basov, M. M. Fogler, and F. J. García de Abajo. Polaritons in van der Waals materials. *Science*, 354(6309):aag1992, 2016.

[29] Tony Low, Andrey Chaves, Joshua D. Caldwell, Anshuman Kumar, Nicholas X. Fang, Phaedon Avouris, Tony F. Heinz, Francisco Guinea, Luis Martin-Moreno, and Frank Koppens. Polaritons in layered two-dimensional materials. *Nat. Mater.*, 16(2):182–194, 2017.

[30] Y. Toyozawa and J. Hermanson. Exciton-phonon bound state: A new quasiparticle. *Physical Review Letters*, 21(24):1637–1641, 1968.

[31] John C. Hermanson. Exciton-phonon bound state and the vibronic spectra of solids. *Physical Review B*, 2(12):5043–5051, 1970.

[32] Y B Levinson and E I Rashba. Electron-phonon and exciton-phonon bound states. *Reports on Progress in Physics*, 36(12):1499–1565, 1973.

[33] P. A. D. Gonçalves, L. P. Bertelsen, Sanshui Xiao, and N. Asger Mortensen. Plasmon-exciton polaritons in two-dimensional semiconductor/metal interfaces. *Phys. Rev. B*, 97(4):041402, 2018.

[34] Denis G. Baranov, Martin Wersäll, Jorge Cuadra, Tomasz J. Antosiewicz, and Timur Shegai. Novel nanostructures and materials for strong light–matter interactions. *ACS Photonics*, 5(1):24–42, 2017.

[35] Jiawei Sun, Yang Li, Huatian Hu, Wen Chen, Di Zheng, Shunping Zhang, and Hongxing Xu. Strong plasmon–exciton coupling in transition metal dichalcogenides and plasmonic nanostructures. *Nanoscale*, 13(8):4408–4419, 2021.

[36] Leo Radzihovsky, Jae Park, and Peter B. Weichman. Superfluid transitions in bosonic atom-molecule mixtures near a Feshbach resonance. *Phys. Rev. Lett.*, 92(16):160402, 2004.

[37] Leo Radzihovsky, Peter B. Weichman, and Jae I. Park. Superfluidity and phase transitions in a resonant Bose gas. *Ann. Phys.*, 323(10):2376–2451, 2008.

[38] M. W. J. Romans, R. A. Duine, Subir Sachdev, and H. T. C. Stoof. Quantum phase transition in an atomic Bose gas with a Feshbach resonance. *Phys. Rev. Lett.*, 93(2):020405, 2004.

[39] F. M. Marchetti and Jonathan Keeling. Collective pairing of resonantly coupled microcavity polaritons. *Phys. Rev. Lett.*, 113(21):216405, 2014.

[40] Monique Combescot and Shiue-Yuan Shiau. *Excitons and Cooper Pairs: Two Composite Bosons in Many-Body Physics*. Oxford University Press, 2016.

[41] L. D. Landau and E. M. Lifshitz. *Quantum Mechanics Non-Relativistic Theory*. Elsevier Science and Technology Books, 2013.

[42] Ryo Maezono, Pablo López Ríos, Tetsuo Ogawa, and Richard J. Needs. Excitons and biexcitons in symmetric electron-hole bilayers. *Physical Review Letters*, 110(21):216407, 2013.

[43] A. A. High, J. R. Leonard, A. T. Hammack, M. M. Fogler, L. V. Butov, A. V. Kavokin, K. L. Campman, and A. C. Gossard. Spontaneous coherence in a cold exciton gas. *Nature*, 483(7391):584–588, 2012.

[44] J. R. Leonard, A. A. High, A. T. Hammack, M. M. Fogler, L. V. Butov, K. L. Campman, and A. C. Gossard. Pancharatnam–Berry phase in condensate of indirect excitons. *Nature Communications*, 9(1), 2018.

[45] J. R. Leonard, Lunhui Hu, A. A. High, A. T. Hammack, Congjun Wu, L. V. Butov, K. L. Campman, and A. C. Gossard. Moiré pattern of interference dislocations in condensate of indirect excitons. *Nature Communications*, 12(1), 2021.

[46] Cheol-Hwan Park and Steven G. Louie. Tunable excitons in biased bilayer graphene. *Nano Lett.*, 10(2):426–431, 2010.

[47] Long Ju, Lei Wang, Ting Cao, Takashi Taniguchi, Kenji Watanabe, Steven G. Louie, Farhan Rana, Jiwoong Park, James Hone, Feng Wang, and Paul L. McEuen. Tunable excitons in bilayer graphene. *Science*, 358(6365):907–910, 2017.

[48] Joshua D. Caldwell, Andrey V. Kretinin, Yiguo Chen, Vincenzo Giannini, Michael M. Fogler, Yan Francescato, Chase T. Ellis, Joseph G. Tischler, Colin R. Woods, Alexander J. Giles, Minghui Hong, Kenji Watanabe, Takashi Taniguchi, Stefan A. Maier, and Kostya S. Novoselov. Sub-diffractional volume-confined polaritons in the natural hyperbolic material hexagonal boron nitride. *Nat. Commun.*, 5(1):5221,

2014.

[49] Alexander J. Giles, Siyuan Dai, Igor Vurgaftman, Timothy Hoffman, Song Liu, Lucas Lindsay, Chase T. Ellis, Nathanael Assefa, Ioannis Chatzakis, Thomas L. Reinecke, Joseph G. Tischler, Michael M. Fogler, J. H. Edgar, D. N. Basov, and Joshua D. Caldwell. Ultralow-loss polaritons in isotopically pure boron nitride. *Nat. Mater.*, 17(2):134–139, 2017.

[50] Jian Qin, Yu-Hui Chen, Zhepeng Zhang, Yanfeng Zhang, Richard J. Blaikie, Boyang Ding, and Min Qiu. Revealing strong plasmon-exciton coupling between nanogap resonators and two-dimensional semiconductors at ambient conditions. *Phys. Rev. Lett.*, 124(6):063902, 2020.

[51] Yumeng You, Xiao-Xiao Zhang, Timothy C. Berkelbach, Mark S. Hybertsen, David R. Reichman, and Tony F. Heinz. Observation of biexcitons in monolayer WSe2. *Nat. Phys.*, 11(6):477–481, 2015.

[52] Heiko Groß, Joachim M. Hamm, Tommaso Tufarelli, Ortwin Hess, and Bert Hecht. Near-field strong coupling of single quantum dots. *Science Advances*, 4(3), 2018.

[53] Kyoung-Duck Park, Molly A. May, Haixu Leng, Jiarong Wang, Jaron A. Kropp, Theodosia Gougousi, Matthew Pelton, and Markus B. Raschke. Tip-enhanced strong coupling spectroscopy, imaging, and control of a single quantum emitter. *Sci. Adv.*, 5(7):eaav5931, 2019.

[54] S. Alyatkin, H. Sigurdsson, A. Askitopoulos, J. D. Töpfer, and P. G. Lagoudakis. Quantum fluids of light in all-optical scatterer lattices. *Nature Communications*, 12(1), 2021.

[55] Hisaki Oka and Hajime Ishihara. Highly efficient generation of entangled photons by controlling cavity bipolariton states. *Phys. Rev. Lett.*, 100(17):170505, 2008.

[56] Scott E. Pollack, Daniel Dries, and Randall G. Hulet. Universality in three- and four-body bound states of ultracold atoms. *Science*, 326(5960):1683–1685, 2009.

[57] P. Makotyn, C. E. Klauss, D. L. Goldberger, E. A. Cornell, and D. S. Jin. Universal dynamics of a degenerate unitary Bose gas. *Nature Physics*, 10(2):116–119, 2014.

[58] Jason H. V. Nguyen, De Luo, and Randall G. Hulet. Formation of matter-wave soliton trains by modulational instability. *Science*, 356(6336):422–426, 2017.

[59] C. R. Cabrera, L. Tanzi, J. Sanz, B. Naylor, P. Thomas, P. Cheiney, and L. Tarruell. Quantum liquid droplets in a mixture of Bose-Einstein condensates. *Science*, 359(6373):301–304, 2018.

[60] Lukas Wehmeier, Suheng Xu, Rafael A. Mayer, Brian Vermilyea, Makoto Tsuneto, Michael Dapolito, Rui Pu, Zengyi Du, Xinzhong Chen, Wenjun Zheng, Ran Jing, Zijian Zhou, Kenji Watanabe, Takashi Taniguchi, Adrian Gozar, Qiang Li, Alexey B. Kuzmenko, G. Lawrence Carr, Xu Du, Michael M. Fogler, D. N. Basov, and Mengkun Liu. Landau-phonon polaritons in Dirac heterostructures. *Science Advances*, 10(37), 2024.

[61] D. N. Basov, Ana Asenjo-Garcia, P. James Schuck, Xiaoyang Zhu, and Angel Rubio. Polariton panorama. *Nanophotonics*, 10(1):549–577, 2020.

[62] C. Faugeras, S. Berciaud, P. Leszczynski, Y. Henni, K. Nogajewski, M. Orlita, T. Taniguchi, K. Watanabe, C. Forsythe, P. Kim, R. Jalil, A.K. Geim, D.M. Basko, and M. Potemski. Landau level spectroscopy of electron-electron interactions in graphene. *Physical Review Letters*, 114(12):126804, 2015.

[63] Ievgeniia O. Nedoliuk, Sheng Hu, Andre K. Geim, and Alexey B. Kuzmenko. Colossal infrared and terahertz magneto-optical activity in a two-dimensional Dirac material. *Nature Nanotechnology*, 14(8):756–761, 2019.

[64] R. Roldán, J.-N. Fuchs, and M. O. Goerbig. Collective modes of doped graphene and a standard two-dimensional electron gas in a strong magnetic field: Linear magnetoplasmons versus magnetoexcitons. *Physical Review B*, 80(8):085408, 2009.

[65] Michael Dapolito, Makoto Tsuneto, Wenjun Zheng, Lukas Wehmeier, Suheng Xu, Xinzhong Chen, Jiacheng Sun, Zengyi Du, Yinming Shao, Ran Jing, Shuai Zhang, Adrien Bercher, Yinan Dong, Dorri Halbertal, Vibhu Ravindran, Zijian Zhou, Mila Petrovic, Adrian Gozar, G. L. Carr, Qiang Li, Alexey B. Kuzmenko, Michael M. Fogler, D. N. Basov, Xu Du, and Mengkun Liu. Infrared nano-imaging of Dirac magnetoexcitons in graphene. *Nature Nanotechnology*, 18(12):1409–1415, 2023.

[66] S. Dai, Z. Fei, Q. Ma, A. S. Rodin, M. Wagner, A. S. McLeod, M. K. Liu, W. Gannett, W. Regan, K. Watanabe, T. Taniguchi, M. Thiemens, G. Dominguez, A. H. Castro Neto, A. Zettl, F. Keilmann, P. Jarillo-Herrero, M. M. Fogler, and D. N. Basov. Tunable phonon polaritons in atomically thin van der Waals crystals of boron nitride. *Science*, 343(6175):1125–1129, 2014.

[67] K. Shizuya. Many-body corrections to cyclotron resonance in monolayer and bilayer graphene. *Physical Review B*, 81(7):075407, 2010.

[68] D. C. Elias, R. V. Gorbachev, A. S. Mayorov, S. V. Morozov, A. A. Zhukov, P. Blake, L. A. Ponomarenko, I. V. Grigorieva, K. S. Novoselov, F. Guinea, and A. K. Geim. Dirac cones reshaped by interaction effects in suspended graphene. *Nature Physics*, 7(9):701–704, 2011.

[69] S. Das Sarma. Theory of two-dimensional magnetopolarons. *Physical Review Letters*, 52(10):859–862, 1984.

[70] J. Zhu, S. M. Badalyan, and F. M. Peeters. Electron-phonon bound states in graphene in a perpendicular magnetic field. *Physical Review Letters*, 109(25):256602, 2012.

[71] D. C. Tsui, Th. Englert, A. Y. Cho, and A. C. Gossard. Observation of magnetophonon resonances in a two-dimensional electronic system. *Physical Review Letters*, 44(5):341–344, 1980.

[72] L. V. Butov, V. I. Grinev, V. D. Kulakovskii, and T. G. Andersson. Direct observation of magnetoplasmon-phonon coupled modes in the magnetophotoluminescence spectra of the two-dimensional electron gas in $In_xGa_{1-x}as$/gaas quantum wells. *Physical Review B*, 46(20):13627–13630, 1992.

[73] R.J. Nicholas. The magnetophonon effect. *Progress in Quantum Electronics*, 10(1):1–75, 1985.

[74] Clement Faugeras, Milan Orlita, and Marek Potemski. Raman scattering of graphene-based systems in high magnetic fields. *Journal of Raman Spectroscopy*, 49(1):146–156, 2017.

[75] Yoshinori Tokura and Naoto Nagaosa. Nonreciprocal responses from non-centrosymmetric quantum materials. *Nature Communications*, 9(1), 2018.

[76] Todd Van Mechelen, Wenbo Sun, and Zubin Jacob. Optical n-invariant of graphene's topological viscous Hall fluid. *Nature Communications*, 12(1), 2021.

[77] Arpit Arora, Mark S. Rudner, and Justin C. W. Song. Quantum plasmonic nonreciprocity in parity-violating magnets. *Nano Letters*, 22(23):9351–9357, 2022.

[78] Felice Appugliese, Josefine Enkner, Gian Lorenzo Paravicini-Bagliani, Mattias Beck, Christian Reichl, Werner Wegscheider, Giacomo Scalari, Cristiano Ciuti, and Jérôme Faist. Breakdown of topological protection by cavity vacuum fields in the integer quantum Hall effect. *Science*, 375(6584):1030–1034, 2022.

[79] Prasahnt Sivarajah, Andreas Steinbacher, Blake Dastrup, Jian Lu, Maolin Xiang, Wei Ren, Stanislav Kamba, Shixun Cao, and Keith A. Nelson. THz-frequency magnon-phonon-polaritons in the collective strong-coupling regime. *Journal of Applied Physics*, 125(21), 2019.

[80] Vasil Rokaj, Markus Penz, Michael A. Sentef, Michael Ruggenthaler, and Angel Rubio. Polaritonic hofstadter butterfly and cavity control of the quantized Hall

conductance. *Physical Review B*, 105(20):205424, 2022.

[81] Lucas Winter and Oded Zilberberg. Fractional quantum Hall edge polaritons, 2023.

[82] M. M. Fogler, A. A. Koulakov, and B. I. Shklovskii. Ground state of a two-dimensional electron liquid in a weak magnetic field. *Physical Review B*, 54(3):1853–1871, 1996.

[83] Erik A. Szwed, Brian Vermilyea, Darius J. Choksy, Zhiwen Zhou, Michael M. Fogler, Leonid V. Butov, Dmitry K. Efimkin, Kirk W. Baldwin, and Loren Pfeiffer. Excitonic Bose polarons in electron–hole bilayers. *Nano Letters*, 24(42):13219–13223, 2024.

[84] Yu. E. Lozovik and V. I. Yudson. A new mechanism for superconductivity: pairing between spatially separated electrons and holes. *Sov. Phys. JETP*, 44:389, 1976.

[85] L. V. Keldysh and A. N. Kozlov. Collective properties of excitons in semiconductors. *Sov. Phys. JETP*, 27:521–528, 1968.

[86] L. V. Keldysh and Yu. V. Kopaev. Possible instability of the semimetallic state toward Coulomb interaction. *Sov. Phys. Solid State*, 6:2219, 1965.

[87] C. Comte and P. Noziéres. Exciton Bose condensation: the ground state of an electron-hole gas - i. mean field description of a simplified model. *J. Phys. France*, 43(7):1069–1081, 1982.

[88] D. J. Choksy, E. A. Szwed, L. V. Butov, K. W. Baldwin, and L. N. Pfeiffer. Fermi edge singularity in neutral electron-hole system. *Nature Physics*, 19(9):1275–1279, 2023.

[89] D. J. Choksy, Chao Xu, M. M. Fogler, L. V. Butov, J. Norman, and A. C. Gossard. Attractive and repulsive dipolar interaction in bilayers of indirect excitons. *Phys. Rev. B*, 103:045126, 2021.

[90] Daijiro Yoshioka and Allan H. MacDonald. Double quantum well electron-hole systems in strong magnetic fields. *J. Phys. Soc. Jpn.*, 59(12):4211–4214, 1990.

[91] Chao Xu and Michael M. Fogler. Ground and excited states of coupled exciton liquids in electron-hole quadrilayers. *Phys. Rev. B*, 104:195430, 2021.

[92] S. Schmitt-Rink, D. S. Chemla, and D. A. B. Miller. Linear and nonlinear optical properties of semiconductor quantum wells. *Adv. Phys.*, 38(2):89–188, 1989.

[93] G. Bastard and J. Brum. Electronic states in semiconductor heterostructures. *IEEE J. Quantum Electron.*, 22(9):1625–1644, 1986.

[94] Fedor T. Vasko and Alex V. Kuznetsov. *Electronic States and Optical Transitions in Semiconductor Heterostructures*. Graduate Texts in Contemporary Physics. Springer, New York, 1998.

[95] K. Sivalertporn, L. Mouchliadis, A. L. Ivanov, R. Philp, and E. A. Muljarov. Direct and indirect excitons in semiconductor coupled quantum wells in an applied electric field. *Phys. Rev. B*, 85:045207, 2012.

[96] Calvin Yi-Ping Chao and Shun Lien Chuang. Analytical and numerical solutions for a two-dimensional exciton in momentum space. *Phys. Rev. B*, 43(8):6530, 1991.

[97] K. Varga and Y. Suzuki. Precise solution of few-body problems with the stochastic variational method on a correlated Gaussian basis. *Phys. Rev. C*, 52:2885–2905, 1995.

[98] A. D. Meyertholen and M. M. Fogler. Biexcitons in two-dimensional systems with spatially separated electrons and holes. *Phys. Rev. B*, 78:235307, 2008.

[99] M. Schick. Two-dimensional system of hard-core bosons. *Physical Review A*, 3(3):1067–1073, 1971.

[100] V. N. Popov. On the theory of the superfluidity of two- and one-dimensional Bose systems. *Theoretical and Mathematical Physics*, 11(3):565–573, 1972.

[101] G. E. Astrakharchik, J. Boronat, J. Casulleras, I. L. Kurbakov, and Yu. E. Lozovik. Weakly interacting two-dimensional system of dipoles: Limitations of the mean-field theory. *Physical Review A*, 75(6):063630, 2007.

[102] G. E. Astrakharchik, J. Boronat, J. Casulleras, I. L. Kurbakov, and Yu. E. Lozovik. Equation of state of a weakly interacting two-dimensional Bose gas studied at zero temperature by means of quantum Monte Carlo methods. *Physical Review A*, 79(5):051602, 2009.

[103] H. Haug and S. Schmitt-Rink. Electron theory of the optical properties of laser-excited semiconductors. *Progress in Quantum Electronics*, 9(1):3–100, 1984.

[104] Christoph Schindler and Roland Zimmermann. Analysis of the exciton-exciton interaction in semiconductor quantum wells. *Phys. Rev. B*, 78:045313, 2008.

[105] L. A. Peña Ardila, G. E. Astrakharchik, and S. Giorgini. Strong coupling Bose polarons in a two-dimensional gas. *Physical Review Research*, 2(2):023405, 2020.

[106] G. Guijarro, G. E. Astrakharchik, J. Boronat, B. Bazak, and D. S. Petrov. Few-body bound states of two-dimensional bosons. *Physical Review A*, 101(4):041602, 2020.

[107] W. Casteels, J. Tempere, and J. T. Devreese. Polaronic properties of an impurity in a Bose-Einstein condensate in reduced dimensions. *Physical Review A*, 86(4):043614, 2012.

[108] Volodymyr Pastukhov. Polaron in dilute 2D Bose gas at low temperatures. *Journal of Physics B: Atomic, Molecular and Optical Physics*, 51(15):155203, 2018.

[109] Jesper Levinsen, Francesca Maria Marchetti, Jonathan Keeling, and Meera M. Parish. Spectroscopic signatures of quantum many-body correlations in polariton microcavities. *Physical Review Letters*, 123(26):266401, 2019.

[110] Ivan Amelio, N. D. Drummond, Eugene Demler, Richard Schmidt, and Atac Imamoglu. Polaron spectroscopy of a bilayer excitonic insulator. *Phys. Rev. B*, 107:155303, 2023.

[111] Yasufumi Nakano, Meera M. Parish, and Jesper Levinsen. Variational approach to the two-dimensional Bose polaron. *Physical Review A*, 109(1):013325, 2024.

[112] E. Akaturk and B. Tanatar. Two-dimensional Bose polaron using diffusion Monte Carlo method. *International Journal of Modern Physics B*, 33(21):1950238, 2019.

[113] Felipe Isaule, Ivan Morera, Pietro Massignan, and Bruno Juliá-Díaz. Renormalization-group study of Bose polarons. *Physical Review A*, 104(2):023317, 2021.

[114] Luis Fernando Cárdenas-Castillo and Arturo Camacho-Guardian. Strongly interacting bose polarons in two-dimensional atomic gases and quantum fluids of polaritons. *Atoms*, 11(1):3, 2022.

[115] O Hryhorchak, G Panochko, and V Pastukhov. Mean-field study of repulsive 2D and 3D Bose polarons. *Journal of Physics B: Atomic, Molecular and Optical Physics*, 53(20):205302, 2020.

[116] Galyna Panochko and Volodymyr Pastukhov. Static impurities in a weakly interacting Bose gas. *Atoms*, 10(1):19, 2022.

[117] Tao Shi, E. A. Demler, and et al. Dynamics of Bose polarons in ultracold atoms and dissipative Bose-Einstein condensates of excitons. unpublished, 2024.

[118] Steffen Patrick Rath and Richard Schmidt. Field-theoretical study of the Bose polaron. *Phys. Rev. A*, 88:053632, November 2013.

[119] Yulia E. Shchadilova, Richard Schmidt, Fabian Grusdt, and Eugene Demler. Quantum dynamics of ultracold Bose polarons. *Physical Review Letters*, 117(11):113002, 2016.

[120] Rasmus Søgaard Christensen, Jesper Levinsen, and Georg M. Bruun. Quasiparticle properties of a mobile impurity in a Bose-Einstein condensate. *Physical Review Letters*, 115(16):160401, 2015.

[121] Nguyen N. T. Nam and Mikito Koshino. Lattice relaxation and energy band modulation in twisted bilayer graphene. *Physical Review B*, 96(7):075311, 2017.

[122] Fernando Gargiulo and Oleg V Yazyev. Structural and electronic transformation in low-angle twisted bilayer graphene. *2D Materials*, 5(1):015019, 2017.

[123] Hyobin Yoo, Rebecca Engelke, Stephen Carr, Shiang Fang, Kuan Zhang, Paul Cazeaux, Suk Hyun Sung, Robert Hovden, Adam W. Tsen, Takashi Taniguchi, Kenji Watanabe, Gyu-Chul Yi, Miyoung Kim, Mitchell Luskin, Ellad B. Tadmor, Efthimios Kaxiras, and Philip Kim. Atomic and electronic reconstruction at the van der Waals interface in twisted bilayer graphene. *Nature Materials*, 18(5):448–453, 2019.

[124] Yuanbo Zhang, Tsung-Ta Tang, Caglar Girit, Zhao Hao, Michael C. Martin, Alex Zettl, Michael F. Crommie, Y. Ron Shen, and Feng Wang. Direct observation of a widely tunable bandgap in bilayer graphene. *Nature*, 459(7248):820–823, 2009.

[125] Ivar Martin, Ya. M. Blanter, and A. F. Morpurgo. Topological confinement in bilayer graphene. *Physical Review Letters*, 100(3):036804, 2008.

[126] Fan Zhang, Allan H. MacDonald, and Eugene J. Mele. Valley Chern numbers and boundary modes in gapped bilayer graphene. *Proceedings of the National Academy of Sciences*, 110(26):10546–10551, 2013.

[127] Abolhassan Vaezi, Yufeng Liang, Darryl H. Ngai, Li Yang, and Eun-Ah Kim. Topological edge states at a tilt boundary in gated multilayer graphene. *Physical Review X*, 3(2):021018, 2013.

[128] Long Ju, Zhiwen Shi, Nityan Nair, Yinchuan Lv, Chenhao Jin, Jairo Velasco, Claudia Ojeda-Aristizabal, Hans A. Bechtel, Michael C. Martin, Alex Zettl, James Analytis, and Feng Wang. Topological valley transport at bilayer graphene domain walls. *Nature*, 520(7549):650–655, 2015.

[129] Long-Jing Yin, Hua Jiang, Jia-Bin Qiao, and Lin He. Direct imaging of topological edge states at a bilayer graphene domain wall. *Nature Communications*, 7(1), 2016.

[130] Eddwi H. Hasdeo and Justin C. W. Song. Long-lived domain wall plasmons in gapped bilayer graphene. *Nano Letters*, 17(12):7252–7257, 2017.

[131] Pablo San-Jose and Elsa Prada. Helical networks in twisted bilayer graphene under

interlayer bias. *Physical Review B*, 88(12):121408, 2013.

[132] Shengqiang Huang, Kyounghwan Kim, Dmitry K. Efimkin, Timothy Lovorn, Takashi Taniguchi, Kenji Watanabe, Allan H. MacDonald, Emanuel Tutuc, and Brian J. LeRoy. Topologically protected helical states in minimally twisted bilayer graphene. *Physical Review Letters*, 121(3):037702, 2018.

[133] Niels R Walet and Francisco Guinea. The emergence of one-dimensional channels in marginal-angle twisted bilayer graphene. *2D Materials*, 7(1):015023, 2019.

[134] S. G. Xu, A. I. Berdyugin, P. Kumaravadivel, F. Guinea, R. Krishna Kumar, D. A. Bandurin, S. V. Morozov, W. Kuang, B. Tsim, S. Liu, J. H. Edgar, I. V. Grigorieva, V. I. Fal'ko, M. Kim, and A. K. Geim. Giant oscillations in a triangular network of one-dimensional states in marginally twisted graphene. *Nature Communications*, 10(1), 2019.

[135] Maximilian Fleischmann, Reena Gupta, Florian Wullschläger, Simon Theil, Dominik Weckbecker, Velimir Meded, Sangeeta Sharma, Bernd Meyer, and Samuel Shallcross. Perfect and controllable nesting in minimally twisted bilayer graphene. *Nano Letters*, 20(2):971–978, 2019.

[136] Bonnie Tsim, Nguyen N. T. Nam, and Mikito Koshino. Perfect one-dimensional chiral states in biased twisted bilayer graphene. *Physical Review B*, 101(12):125409, 2020.

[137] Tao Hou, Yafei Ren, Yujie Quan, Jeil Jung, Wei Ren, and Zhenhua Qiao. Metallic network of topological domain walls. *Physical Review B*, 101(20):201403, 2020.

[138] Lili Jiang, Zhiwen Shi, Bo Zeng, Sheng Wang, Ji-Hun Kang, Trinity Joshi, Chenhao Jin, Long Ju, Jonghwan Kim, Tairu Lyu, Yuen-Ron Shen, Michael Crommie, Hong-Jun Gao, and Feng Wang. Soliton-dependent plasmon reflection at bilayer graphene domain walls. *Nature Materials*, 15(8):840–844, 2016.

[139] Bor-Yuan Jiang, Guang-Xin Ni, Zachariah Addison, Jing K. Shi, Xiaomeng Liu, Shu Yang Frank Zhao, Philip Kim, Eugene J. Mele, Dimitri N. Basov, and Michael M. Fogler. Plasmon reflections by topological electronic boundaries in bilayer graphene. *Nano Letters*, 17(11):7080–7085, 2017.

[140] S. S. Sunku, G. X. Ni, B. Y. Jiang, H. Yoo, A. Sternbach, A. S. McLeod, T. Stauber, L. Xiong, T. Taniguchi, K. Watanabe, P. Kim, M. M. Fogler, and D. N. Basov. Photonic crystals for nano-light in moiré graphene superlattices. *Science*, 362(6419):1153–1156, 2018.

[141] Dmitry K. Efimkin and Allan H. MacDonald. Helical network model for twisted

bilayer graphene. *Physical Review B*, 98(3):035404, 2018.

[142] C. De Beule, F. Dominguez, and P. Recher. Aharonov-Bohm oscillations in minimally twisted bilayer graphene. *Physical Review Letters*, 125(9):096402, 2020.

[143] Yang-Zhi Chou, Fengcheng Wu, and Sankar Das Sarma. Hofstadter butterfly and Floquet topological insulators in minimally twisted bilayer graphene. *Physical Review Research*, 2(3):033271, 2020.

[144] Xiao-Chuan Wu, Chao-Ming Jian, and Cenke Xu. Coupled-wire description of the correlated physics in twisted bilayer graphene. *Physical Review B*, 99(16):161405, 2019.

[145] Jongjun M. Lee, Masaki Oshikawa, and Gil Young Cho. Non-Fermi liquids in conducting two-dimensional networks. *Physical Review Letters*, 126(18):186601, 2021.

[146] Yang-Zhi Chou, Fengcheng Wu, and Jay D. Sau. Charge density wave and finite-temperature transport in minimally twisted bilayer graphene. *Physical Review B*, 104(4):045146, July 2021.

[147] Supriyo Datta. *Electronic Transport in Mesoscopic Systems*. Cambridge University Press, 1995.

[148] Luis Brey, T. Stauber, T. Slipchenko, and L. Martín-Moreno. Plasmonic Dirac cone in twisted bilayer graphene. *Physical Review Letters*, 125(25):256804, 2020.

[149] J T Chalker and P D Coddington. Percolation, quantum tunnelling and the integer Hall effect. *Journal of Physics C: Solid State Physics*, 21(14):2665–2679, 1988.

[150] Alex Kamenev and Walter Kohn. Landauer conductance without two chemical potentials. *Physical Review B*, 63(15):155304, 2001.

[151] F Guinea, G. Gómez Santos, M Sassetti, and M Ueda. Asymptotic tunnelling conductance in Luttinger liquids. *Europhysics Letters (EPL)*, 30(9):561–566, 1995.

[152] Manuel Houzet, Tsuyoshi Yamamoto, and Leonid I. Glazman. Microwave spectroscopy of the Schmid transition. *Physical Review B*, 109(15):155431, 2024.

[153] F. Parage, M. M. Doria, and O. Buisson. Plasma modes in periodic two-dimensional superconducting-wire networks. *Physical Review B*, 58(14):R8921–R8924, 1998.

[154] Jorik van de Groep, Pierpaolo Spinelli, and Albert Polman. Transparent conducting silver nanowire networks. *Nano Letters*, 12(6):3138–3144, 2012.

[155] Amit Agarwal, Sourin Das, and Diptiman Sen. Power dissipation for systems with junctions of multiple quantum wires. *Physical Review B*, 81(3):035324, 2010.

[156] Xinzhong Chen, Debo Hu, Ryan Mescall, Guanjun You, D. N. Basov, Qing Dai, and Mengkun Liu. Modern scattering-type scanning near-field optical microscopy for advanced material research. *Advanced Materials*, 31(24), 2019.

[157] B.-Y. Jiang, L. M. Zhang, A. H. Castro Neto, D. N. Basov, and M. M. Fogler. Generalized spectral method for near-field optical microscopy. *Journal of Applied Physics*, 119(5), 2016.

[158] Patrick Gallagher, Chan-Shan Yang, Tairu Lyu, Fanglin Tian, Rai Kou, Hai Zhang, Kenji Watanabe, Takashi Taniguchi, and Feng Wang. Quantum-critical conductivity of the Dirac fluid in graphene. *Science*, 364(6436):158–162, 2019.

[159] J. W. McIver, B. Schulte, F.-U. Stein, T. Matsuyama, G. Jotzu, G. Meier, and A. Cavalleri. Light-induced anomalous Hall effect in graphene. *Nature Physics*, 16(1):38–41, 2020.

[160] Andreas Sinner, Pierre A. Pantaleón, and Francisco Guinea. Strain-induced quasi-1D channels in twisted moiré lattices. *Physical Review Letters*, 131(16):166402, 2023.

[161] Cyprian Lewandowski and Leonid Levitov. Intrinsically undamped plasmon modes in narrow electron bands. *Proceedings of the National Academy of Sciences*, 116(42):20869–20874, 2019.

[162] Pawel Hawrylak. Optical properties of a two-dimensional electron gas: Evolution of spectra from excitons to Fermi-edge singularities. *Phys. Rev. B*, 44:3821–3828, 1991.

[163] Jia Wang, Xia-Ji Liu, and Hui Hu. Exact quasiparticle properties of a heavy polaron in bcs fermi superfluids. *Physical Review Letters*, 128(17):175301, April 2022.

[164] Yang Xu, Song Liu, Daniel A. Rhodes, Kenji Watanabe, Takashi Taniguchi, James Hone, Veit Elser, Kin Fai Mak, and Jie Shan. Correlated insulating states at fractional fillings of moiré superlattices. *Nature*, 587(7833):214–218, 2020.

[165] Alexander Popert, Yuya Shimazaki, Martin Kroner, Kenji Watanabe, Takashi Taniguchi, Ataç Imamoğlu, and Tomasz Smoleński. Optical sensing of fractional quantum Hall effect in graphene. *Nano Letters*, 22(18):7363–7369, 2022.

[166] Zhiyuan Sun, D. N. Basov, and M. M. Fogler. Graphene as a source of entangled plasmons. *Physical Review Research*, 4(2):023208, 2022.

[167] G De Chiara, C Brukner, R Fazio, G M Palma, and V Vedral. A scheme for

entanglement extraction from a solid. *New Journal of Physics*, 8(6):95–95, 2006.

[168] D. Bollé and F. Gesztesy. Low-energy parametrization of scattering observables in n-dimensional quantum systems. *Phys. Rev. Lett.*, 52(17):1469–1472, 1984.

[169] E. Hanamura and H. Haug. Condensation effects of excitons. *Physics Reports*, 33(4):209–284, October 1977.